Cell Reports
Physical Science

Article

Ionic hydrogel sensors for low-latency high-accuracy 3D reconstruction of soft robotic endoscope

Graphical abstract

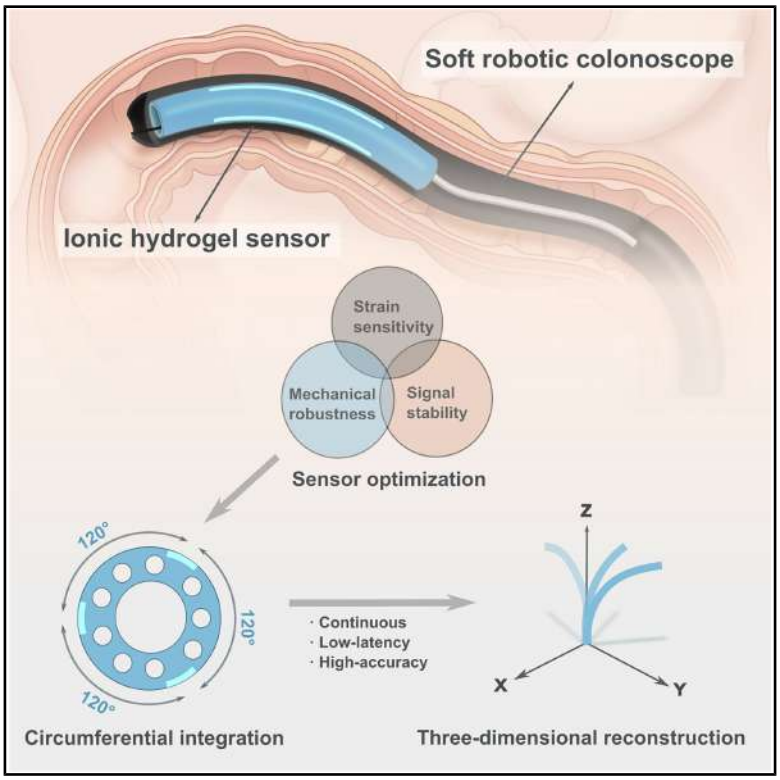

Highlights

- Ionic hydrogel strain sensors enable compliant shape sensing for soft endoscopy
- Joint optimization identifies ideal composition, integration, and sensing conditions
- Three embedded sensors continuously reconstruct 3D endoscope-tip motion
- Delay-compensation strategy nearly halves reconstruction error to 5.9% of arc length

Authors

Shuhang Chen, Jialei Shi, Libaihe Tian, Ferdinando Rodriguez y Baena, Jang Ah Kim, Daniele Dini

Correspondence

shuhang.chen22@imperial.ac.uk (S.C.), j.a.kim@imperial.ac.uk (J.A.K.), d.dini@imperial.ac.uk (D.D.)

In brief

Soft robotic endoscopes require low-cost embedded shape sensing that does not compromise compliance. Chen et al. optimize ionic hydrogel strain sensors and integrate three sensors around a soft endoscope tip, enabling low-latency 3D shape reconstruction. A simple delay-compensation method reduces reconstruction error to 5.9% of actuator length.

Chen et al., 2026, Cell Reports Physical Science 7, 103625
November 18, 2026 © 2026 The Authors. Published by Elsevier Inc.
https://doi.org/10.1016/j.xcrp.2026.103625

CellPress

Cell Reports
Physical Science

CellPress
OPEN ACCESS

Article

Ionic hydrogel sensors for low-latency high-accuracy 3D reconstruction of soft robotic endoscope

Shuhang Chen,[1,*] Jialei Shi,[1,2] Libaihe Tian,[3] Ferdinando Rodriguez y Baena,[1,2] Jang Ah Kim,[1,2,*] and Daniele Dini[1,4,*]
[1]Department of Mechanical Engineering, Imperial College London, South Kensington Campus, London SW7 2AZ, UK
[2]The Hamlyn Centre for Robotic Surgery, Imperial College London, London, UK
[3]Department of Metabolism, Digestion and Reproduction, Imperial College London, London, UK
[4]Lead contact
*Correspondence: shuhang.chen22@imperial.ac.uk (S.C.), j.a.kim@imperial.ac.uk (J.A.K.), d.dini@imperial.ac.uk (D.D.)
https://doi.org/10.1016/j.xcrp.2026.103625

SUMMARY

Continuous shape sensing remains a major barrier to deploying soft robotic endoscopes, because existing solutions often compromise structural compliance, require expensive instrumentation, or provide only limited embedded feedback. Here, we report an integrated soft sensing system based on an array of ionic hydrogel strain sensors, enabling low-latency, high-accuracy three-dimensional shape reconstruction of a soft endoscope tip. Optimization across NaCl concentration, applied voltage, and strain rate identifies ideal composition and operating conditions jointly balancing gauge factor, strain-rate independence, and mechanical robustness. Three optimized sensors are then integrated around the circumference of a soft pneumatic actuator, addressing adhesion, dehydration, and signal stability under actuation. Continuous three-dimensional shape reconstruction is achieved using a Frenet-Serret-based model, and a simple delay-compensation strategy reduces the relative tip-position error from 10.08% to 5.92% of the actuator arc length. This offers a low-cost, compliant, disposable-compatible route to proprioceptive sensing for minimally invasive intervention.

INTRODUCTION

Colorectal cancer (CRC) is a major global health burden, ranking as the third most commonly diagnosed malignancy and the second leading cause of cancer-related death worldwide, with nearly 2 million new cases and approximately 1 million deaths estimated in 2020.[1,2] Over the past three decades, the global burden of CRC has risen substantially, with a particularly marked increase among adults younger than 50 years, driven by rising obesity rates, sedentary lifestyles, and cigarette and alcohol use.[3–5] Colonoscopy remains the gold standard for the detection and removal of precancerous colorectal lesions, but its use is limited by procedure-related pain and discomfort, the risk of complications such as perforation and bleeding, and the requirement for skilled surgeons.[4,6,7] Therefore, there is an increasing need for more accessible, more comfortable for patients, and more automated robotic platforms for CRC surgery.

To address this need, next-generation endoscopes are increasingly adopting soft robot-based designs, which offer inherent compliance enabling continuous deformation along their length rather than at discrete joints, gentle force application to surrounding tissue, and enhanced dexterity in confined anatomical environments.[8,9] Soft everting robotic endoscopes[10,11] and inchworm-like devices[12,13] can achieve minimal pushing and substantially lower (by up to 80%) contact forces and mesentery extension compared to conventional rigid scopes. However, owing to the intrinsic complexity and non-linearity in soft robotic systems, accurate real-time shape reconstruction, which is essential for soft robotics closed-loop control, autonomous navigation, and seamless human-robot interaction, remains a challenge.[14,15]

Over the last decade, a wide range of distributed sensing solutions have been explored for curvature estimation and three-dimensional (3D) shape reconstruction in soft robotic systems. Among these, Fiber Bragg Grating (FBG) sensors are the most mature and extensively studied technology for soft endoscopic shape sensing.[16–18] Integrated within flexible substrates, FBGs can achieve sub-millimeter reconstruction accuracy and enable real-time shape feedback when combined with model-based or data-driven approaches.[18] However, their limited strain tolerance, mechanical fragility, and reliance on costly optical instrumentation restrict their applicability in highly compliant, large-deformation, and disposable soft robotic platforms.[14,15,19] Electromagnetic (EM) tracking systems provide an alternative approach by estimating position and orientation from voltages induced in embedded sensing coils.[20] These systems offer fast response and good robustness without requiring line-of-sight, making them attractive for navigation in confined anatomical

This is an open access article under the CC BY license (http://creativecommons.org/licenses/by/4.0/).

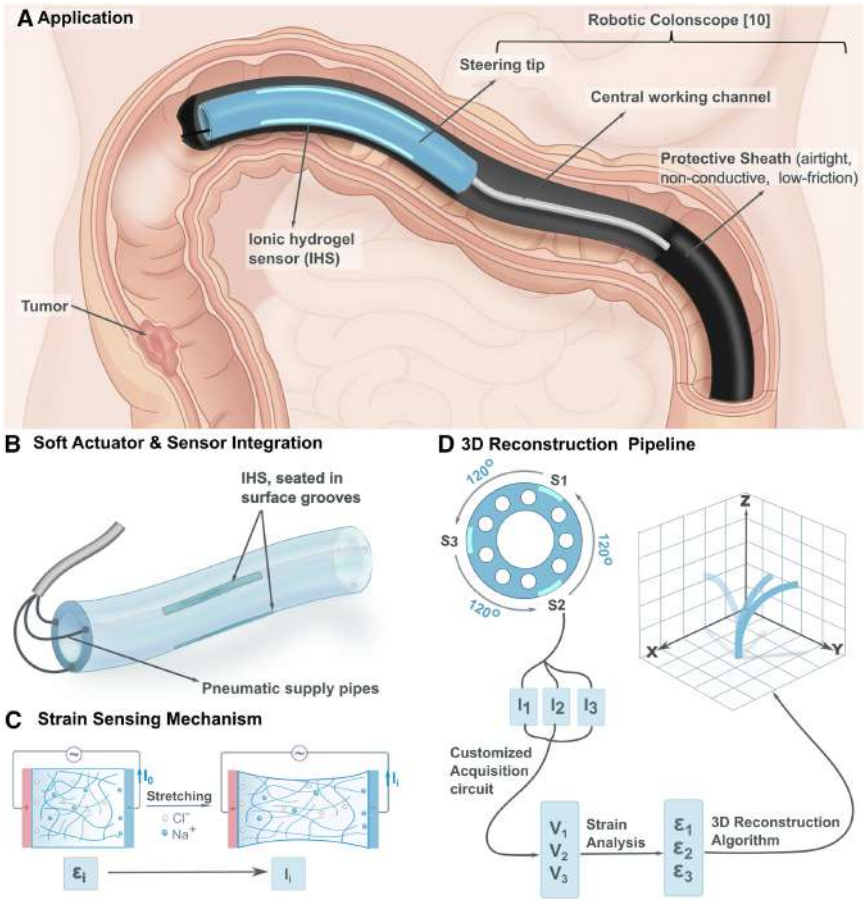

Figure 1. Ionic hydrogel sensors applied as strain sensors for real-time surface strain sensing and three-dimensional shape reconstruction for a soft self-growing colonoscope robot

(A) Conceptual illustration of a soft self-growing colonoscope robot navigating the lower gastrointestinal tract for early cancerous tissue detection and minimally invasive inspection.

(B) Conceptual illustration of soft pneumatic actuator with surface-integrated IHS along its surface.

(C) Strain sensing mechanism of IHS, in which geometrical deformation under an applied voltage induces ionic redistribution, resulting in changes in the output current.

(D) 3D shape reconstruction workflow. Circumferential arrangement of three strain sensors at 120° intervals (S1–S3) enables multi-directional bending detection. The output currents (I_1–I_3) are measured and converted to voltage signals (V_1–V_3) via a customized acquisition circuit. Through strain analysis, the corresponding strains (ε_1–ε_3) are extracted and subsequently processed to estimate the real-time 3D shape of the soft actuator using a reconstruction algorithm.

environments. Nevertheless, EM tracking provides pose information only at discrete sensor locations rather than continuous body-level shape, requires bulky external field generators, and is susceptible to EM interference in clinical settings, limiting scalability and integration simplicity.[14,15,20] Vision-based techniques, including ultrasound imaging,[21] X-ray projection,[22] and fluoroscopy,[23] have also been employed for shape estimation in continuum and soft robots. While these methods can deliver high spatial accuracy, they depend on complex and often bulky imaging infrastructures, suffer from limited temporal resolution or signal-to-noise ratio, and are therefore ill-suited for real-time, embedded shape sensing in soft robotic endoscopes.[14,15]

The limitations of these established approaches have motivated increasing interest in soft material-based strain sensors capable of large deformation and mechanical conformity. Polymer-based piezoresistive and capacitive sensors have been integrated onto soft manipulators for curvature and position estimation, achieving reconstruction errors on the order of 4%–10% of actuator length depending on sensor density and modeling strategy.[24–26] While these approaches preserve compliance, their performance often depends strongly on sensor number, placement, and calibration robustness. In parallel, ionic conductive hydrogels, where electrical signals are carried by mobile ions within a polymer network, have emerged as promising candidates for soft strain sensing due to their ultra-high stretchability, intrinsic softness, biocompatibility, and material tunability.[27,28] They have been widely demonstrated in wearable motion sensing and soft actuator monitoring, with sensing models ranging from linear approximations to geometry-based nonlinear descriptions,[24,29–33] etc. However, most prior studies remain focused on material development and single-sensor demonstrations, with limited consideration of operating conditions, integration challenges, or system-level performance. Despite their material advantages, the deployment of ionic hydrogel strain sensors in functional soft robotic systems—particularly for continuous, real-time three-dimensional shape reconstruction—remains largely unexplored.

Building upon the soft steering robotic endoscope structure previously reported in Shi et al.,[10] this work directly addresses these unmet needs by introducing an end-to-end optimization and integration framework that advances ionic hydrogel strain sensors from materials research to functional proprioception. As conceptually illustrated in Figure 1, polyvinyl alcohol-reinforced polyacrylamide hydrogels doped with sodium chloride (PAAm/PVA-NaCl) are engineered as surface-mounted ionic hydrogel sensors (IHSs). The IHS operates as a piezoresistive strain sensor. When the hydrogel is stretched, changes in its geometry and ionic conduction pathway alter the electrical resistance measured under a constant applied voltage (Figure 1C). The sensor is designed as a compliant surface-mounted strip so that it can deform together with the soft actuator wall. For device integration, multiple IHS strips are arranged circumferentially around the actuator to capture direction-dependent surface strain during pneumatic steering, while the central gauge region remains free to stretch with the actuator and the sensor ends are

CellPress
OPEN ACCESS

fixed through adhesive-electrode interfaces (Figure 1D). This configuration enables direct measurement of local surface strain during multiaxial bending while preserving the intrinsic compliance and continuous deformability that underpin the navigation strategy of our previously reported soft everting endoscope steering tip.[10]

Deployment on a disposable soft endoscopic steering tip requires the surface sensing element to combine high strain sensitivity with signal stability and repeatability under continuous pneumatic actuation, while also meeting practical clinical translation constraints on cost, fabrication simplicity, and millimeter-scale circumferential integration with a limited number of sensing channels. These requirements are inherently coupled, as sensing performance, mechanical compliance, and device manufacturability must be balanced simultaneously rather than optimized independently. This motivates the joint multi-parameter design framework developed in this work.

Guided by these application-specific requirements, we systematically map the coupled parameter space defined by ionic concentration, applied voltage, and strain rate and identify an operating regime that simultaneously maximizes piezoresistive sensitivity, minimizes strain-rate dependence, and maintains mechanical robustness under large deformation. This materials-informed optimization directly enables stable sensor integration on the soft endoscope body, while addressing practical deployment challenges, including adhesion reliability, dehydration-induced drift, and signal stability under actuation. Beyond sensor integration, this work also demonstrates continuous three-dimensional shape reconstruction using a minimal array of three IHSs and a mechanics-based Frenet-Serret formulation, aligned with the geometry and operating principles of the soft endoscope in Shi et al.[10] Dynamic characterization reveals a frequency-dependent delay in the integrated actuator-sensor response—an effect that is rarely quantified in hydrogel-based sensing systems. By explicitly characterizing and compensating for this delay through a lightweight algorithmic approach, we significantly reduce reconstruction error without introducing additional hardware complexity.

Specifically, this work makes three application-driven advances: (1) it establishes a quantitative, multi-parameter optimization framework for ionic hydrogel strain sensors beyond material-level metrics; (2) it demonstrates robust system-level integration and stabilization of these sensors on a soft robotic endoscope steering tip based on our prior platform[10]; and (3) it enables continuous three-dimensional shape reconstruction with fixed-offset delay correction using a minimal sensor architecture.

RESULTS AND DISCUSSION

Material characterization

Design parameter selection for systematic optimization

The IHSs were fabricated via UV polymerization, as detailed in the methods and Figure S1 (supplemental information). As illustrated in Figure 2A, the electrical performance of the IHS was characterized using a customized linear displacement system coupled with a potentiostat (AUTOLAB), with further details provided in the methods section. The IHSs were secured using a pair of film grips with integrated aluminum electrodes, ensuring both mechanical stability and reliable electrical contact under large strain deformation. Uniaxial tensile loading at a constant strain rate was applied using a programmable motorized stage controlled via a custom MATLAB interface. A constant voltage was maintained during deformation, and the corresponding current response was recorded in real time.

To find the optimum operational condition, IHS samples with varying NaCl concentrations (0, 0.1, 0.3, 0.5, 1.0, 1.5, 2.0, and 3.5 wt %) were stretched to failure across a range of strain rates (0.1, 0.5, 1, 5 mm s^{-1}) and tested under different applied voltages (0.5, 1, 1.2, 1.5, 2, 3, 4, 5 V). NaCl concentration is chosen as the primary design variable for sensor optimization, as introducing salt is expected to enhance ionic conductivity, but excessive ion concentration can disrupt gel crosslinking formation, such as hydrogen bonds, thus degrading sensor mechanical toughness.[34] This introduces a trade-off between electrical and mechanical performance. Eight concentrations spanning (0–3.5 wt %) are therefore evaluated to identify the composition that optimally balances these two competing requirements (Table S1, Supplemental Information). For each formulation, the operating voltage was investigated over 0.5–5 V. While conventional hydrogel sensors typically operate below 1 V to avoid electrochemical side reactions and ensure long-term stability,[35–37] the present application targets a single-use tip-disposable robotic endoscope,[10] for which only short-term operational stability is required. A preliminary linear sweep voltammetry (LSV) measurement (Figure S2, Supplemental Information) revealed an inflection point for groups with salt concentration above 1.5 wt %, suggesting that the piezoresistive response of the IHSs was strongly influenced by the applied voltage as well. The applied voltage was therefore treated as another key operating parameter, and the testing range was extended to 5 V to systematically identify the condition that yields the most stable and sensitive piezoresistive response for single-use operation. Finally, four strain rates (0.1–5 mm s^{-1}) were applied to investigate the rate dependence of the piezoresistive response of the IHSs. As the strain rate of the embedded sensors can be directly governed by the pneumatic pressurization speed of the soft actuator, this characterization range was selected to encompass quasi-static deformation regimes relevant to soft stretchable material characterization,[38] ensuring direct relevance to the intended operating conditions. Establishing whether strain rate is a significant independent variable is important to determine the appropriate calibration model for practical deployment.

Definition of characteristic parameters for the response

A representative transient current response $I(t)$ (0.3 wt % salt, 5 V, 0.5 mm s^{-1}) is presented in Figure 2B, illustrating two distinct phases during the uniaxial stretching process. Phase 1 corresponds to an approximately 30 s equilibration period prior to mechanical loading, during which the current signal is allowed to stabilize before deformation commences. The subsequent phase 2 represents the piezoresistive response of IHS upon uniaxial strain deformation. The resistance-time $R(t)$ response is derived as $R(t) = V/I(t)$, where V is the applied constant voltage, and is shown in Figure 2C. Several characteristic parameters

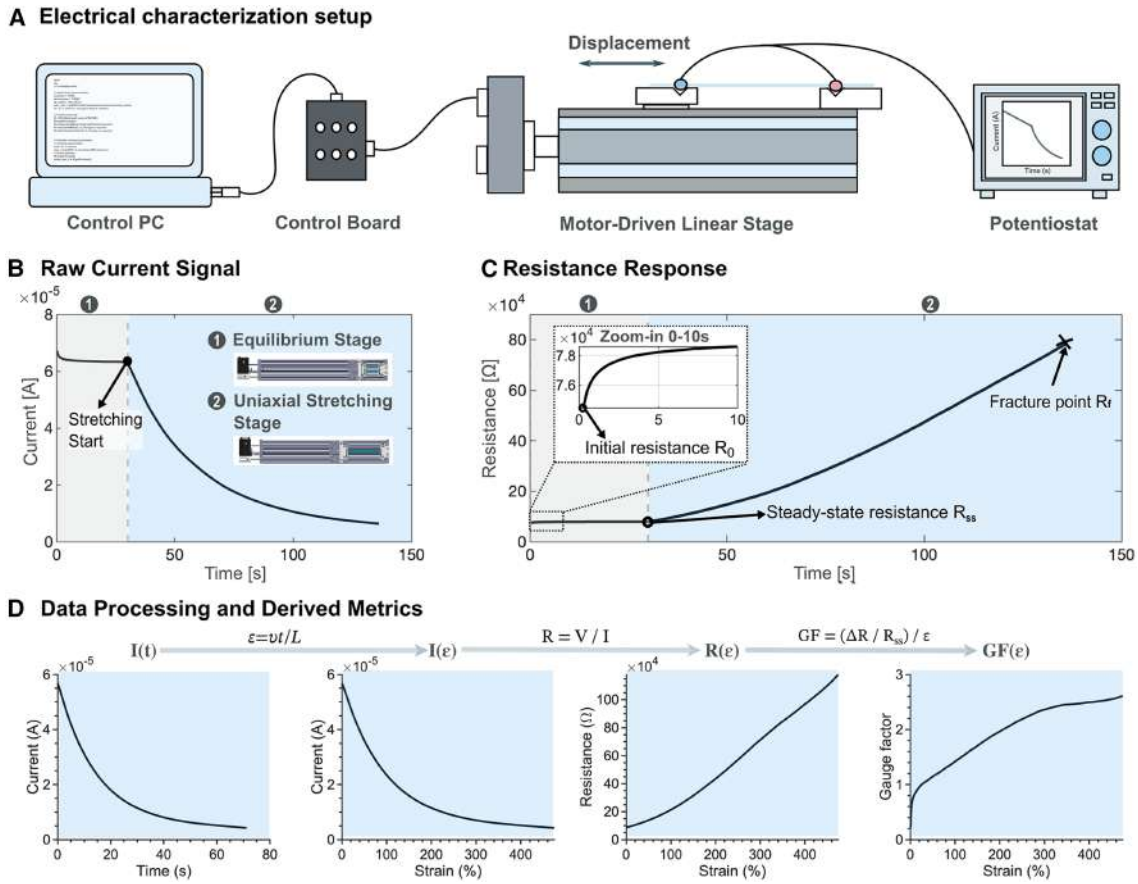

Figure 2. Electrical characterization and signal analysis of the ionic hydrogel sensors

(A) Experimental setup for electrical characterization of IHS under controlled uniaxial stretching.

(B) Representative example of a two-phase raw current signal under a constant applied voltage during the uniaxial tensile loading.

(C) Representative example of raw resistance response as a function of time, including an initial equilibration stage (phase 1) and the subsequent strain-response regimes (phase 2).

(D) Data processing workflow for the strain-response regimes. The measured current signal $I(t)$ is first mapped to $I(\varepsilon)$ using the strain profile from the tensile test as the reference and is then converted to resistance $R(\varepsilon)$ using Ohm's law. The gauge factor is subsequently calculated as a function of strain for comparison across regimes.

are defined from this response to quantify the piezoresistive response of the IHSs:

- Initial resistance (R_0): the first recorded resistance value captured upon signal initiation, before interfacial equilibration.
- Steady state resistance (R_{ss}): the resistance value at the test start point, representing the stabilized baseline following the equilibration stage but prior to mechanical loading.
- Equilibration stage (phase 1): the pre-deformation period during which the current stabilizes toward R_{ss}.
- Uniaxial stretching stage (phase 2): the deformation period over which resistance evolves in response to applied strain, beginning at R_{ss} and ending at fracture R_f. for all subsequent data processing, R_{ss} is taken as the reference baseline with t = 0 defined at the onset of mechanical loading.
- Fracture point: the point of specimen failure, characterized by the fracture resistance R_f, fracture strain ε_f, representing the maximum tensile capability of the IHS.

Mathematical description of the sensing response

The characterization of IHSs follows a systematic data processing workflow (Figure 2D). All subsequent analysis pertains exclusively to phase 2, with the equilibration period (phase 1) excluded from strain conversion. The raw current signal $I(t)$ is first mapped to the strain domain current response $I(\varepsilon)$ via $\varepsilon = vt/L$, where v is the strain rate and L the gauge length, and then converted to resistance using Ohm's law. The gauge factor (GF), defined as the ratio of the fractional resistance change to the applied strain,[30] is expressed as:

$$GF\ \varepsilon\ = \frac{\Delta R\ R_{ss}}{\varepsilon} \qquad \text{(Equation 1)}$$

where $\Delta R = R(\varepsilon)\text{-}R_{ss}$, the ΔR is the resistance change relative to the steady-state baseline.

To assess strain-rate dependence, the coefficient of variation (CV) of resistances across all tested strain rates was computed at each strain level:

$$\mathrm{CV}\ \varepsilon = \frac{\sigma_{R\ \varepsilon}}{\overline{R}\ \varepsilon} \times 100\% \qquad \text{(Equation 2)}$$

where $\overline{R}\ \varepsilon$ and $\sigma_{R(\varepsilon)}$ are the mean and standard deviation of resistance across all tested strain rates at strain ε, respectively. In this work, a CV threshold of 10% is adopted as a practical and relatively conservative repeatability criterion for assessing the strain-rate dependence.[39] A strain-rate-dependent response (CV $\geq$ 10%) causes the $R(\varepsilon)$ calibration to shift with actuation speed, requiring operation at a fixed driving frequency for reliable strain signal analysis. Conversely, a strain-rate-independent response (CV <10%) ensures that a single calibration curve remains valid across varying actuation frequencies, enabling more flexible system operation.[40,41] That is, if the condition of CV < 10% is satisfied, measurements obtained at different strain rates can be treated as equivalent repeats and pooled for the evaluation of the $R(\varepsilon)$ relationship.

Piezoresistive response under varying strain rate and voltage

To illustrate the strain rate effect in detail, the 5 V case is presented as an example. Its transient current response $I(t)$ across four loading strain rates is shown in Figure 3A, and the individual strain-dependent current responses $I(\varepsilon)$ are plotted in Figure 3B. The strong overlap among the four $I(\varepsilon)$ curves indicates that strain rate has a negligible effect on the current response. As the applied voltage was fixed within these tests, the corresponding resistance response shows the same negligible strain-rate dependence, which is further quantified by the CV(ε) value in Figure 3C. As fracture strains varied across samples, the mean CV is only computed when there are at least three valid data points at each strain level, while those where the number of valid samples falls below three are excluded from the summary statistics. Within the range ε < 500%, the mean CV is around 5.2%, confirming that the piezoresistive response is governed primarily by strain rather than strain rate throughout the stretching process. Consequently, the four tests under different strain rates are therefore treated as repeats for all subsequent analysis.

The effect of applied voltage on the resistance response of IHSs is examined next. Figure 3D presents the current $I(\varepsilon)$ (left), resistance $R(\varepsilon)$ (middle), and gauge factor GF(ε) (right) as a function of strain across all eight applied voltages for IHS doped with 0.3 wt % NaCl. Generally, the current decreases with increasing strain across all voltages, with higher applied voltages yielding larger current magnitudes. The starting resistance R_{ss} as a function of voltage is summarized in Figure S7 (Supplemental Information). The resistance increases gradually over the entire strain range across all test voltages. Higher applied voltages yield slightly lower baseline resistance R_{ss}, though the absolute change in resistance ΔR at a given strain remains comparable across voltage levels. The GF (ε) extracted from the resistance strain curves exhibits a non-linear response across all voltages, with a rapid initial rise below 50% strains, followed by a more moderate increase at higher strains.

At 0.5 V, the GF rose sharply to around 0.5 at the beginning and transitioned into a slow quasi-linear regime, approaching 1 at 500% strain. Under 5 V, the GF continued to rise more significantly across the entire tested strain range, reaching approximately 2.5 at ε = 500%, which is around five times the piezoresistive sensitivity observed at 0.5 V under this salt concentration. This voltage dependence of GF can be largely attributed to the difference in R_{ss}. According to Equation 1, for comparable ΔR, higher applied voltage lowers R_{ss} and therefore increases GF. Overall, increasing the applied voltage led to a systematic increase in GF across the strain range, reflecting enhanced strain sensitivity of the IHSs at higher electrical loading.

The summary of strain rate effect across different applied voltages is summarized in Figure 3E, where the mean and maximum CV of resistance across strain rates as a function of applied voltage are presented. The mean CV remains below 10% across all tested voltages, confirming that strain-rate dependence is minimal regardless of the applied voltage. The treatment of different strain rates as repeats is therefore valid across the test voltage range. The fracture strain across applied voltages is summarized in Figure 3F. Under this salt concentration, the mean fracture strain does not show strong voltage dependence.

Multi-parameter optimization and selection of optimal IHS condition

While voltage-dependent tuning offers initial control over piezoresistive sensitivity, practical deployment of ionic hydrogel strain sensors requires a holistic optimization that simultaneously accounts for electrical performance and mechanical durability. In particular, NaCl concentration independently governs ionic conductivity, sensitivity, and network integrity, introducing substantial trade-offs that cannot be resolved by single-parameter optimization. To identify operating conditions suitable for reliable system-level integration, a multi-parameter screening framework is therefore established, combining sensitivity, signal stability, and mechanical robustness as concurrent design criteria.

Figure 4A summarizes the evolution of GF with strain for three representative salt concentrations: salt-free (0 wt %), low salt (0.3 wt %), and high salt (3.5 wt %) hydrogels. In the absence of salt, GF increases monotonically with strain and shows negligible dependence on applied voltage, reflecting the absence of ionic charge carriers. Introducing a low level of NaCl (0.3 wt %) produces a nonlinear GF(ε) response with pronounced voltage dependence: at ε = 500%, GF increases from approximately 1 under 0.5 V to nearly 3 under 5 V, consistent with the voltage-dependent behavior discussed in the preceding subsection. By contrast, hydrogels with high salt concentration (3.5 wt %) exhibit substantially suppressed sensitivity at low voltages, with GF remaining near 0.4 across the entire strain range at 0.5 V, and recovering only under higher applied voltages. The observed inverse relationship between NaCl concentration and GF is consistent with previous reports on NaCl-containing ionic hydrogel strain sensors, in which lower salt content produces looser polymer networks that undergo larger strain-induced geometrical deformation, resulting in greater resistance change.[42] The full parameter-dependent GF trends are further detailed in Figures S8 and S9 (Supplemental Information).

To enable quantitative comparison, GF at ε = 80% is selected as the primary sensitivity metric (Figure 4B). Although the IHSs embedded on the soft actuator typically experience strains below 60%, ε = 80% is chosen to provide a conservative upper

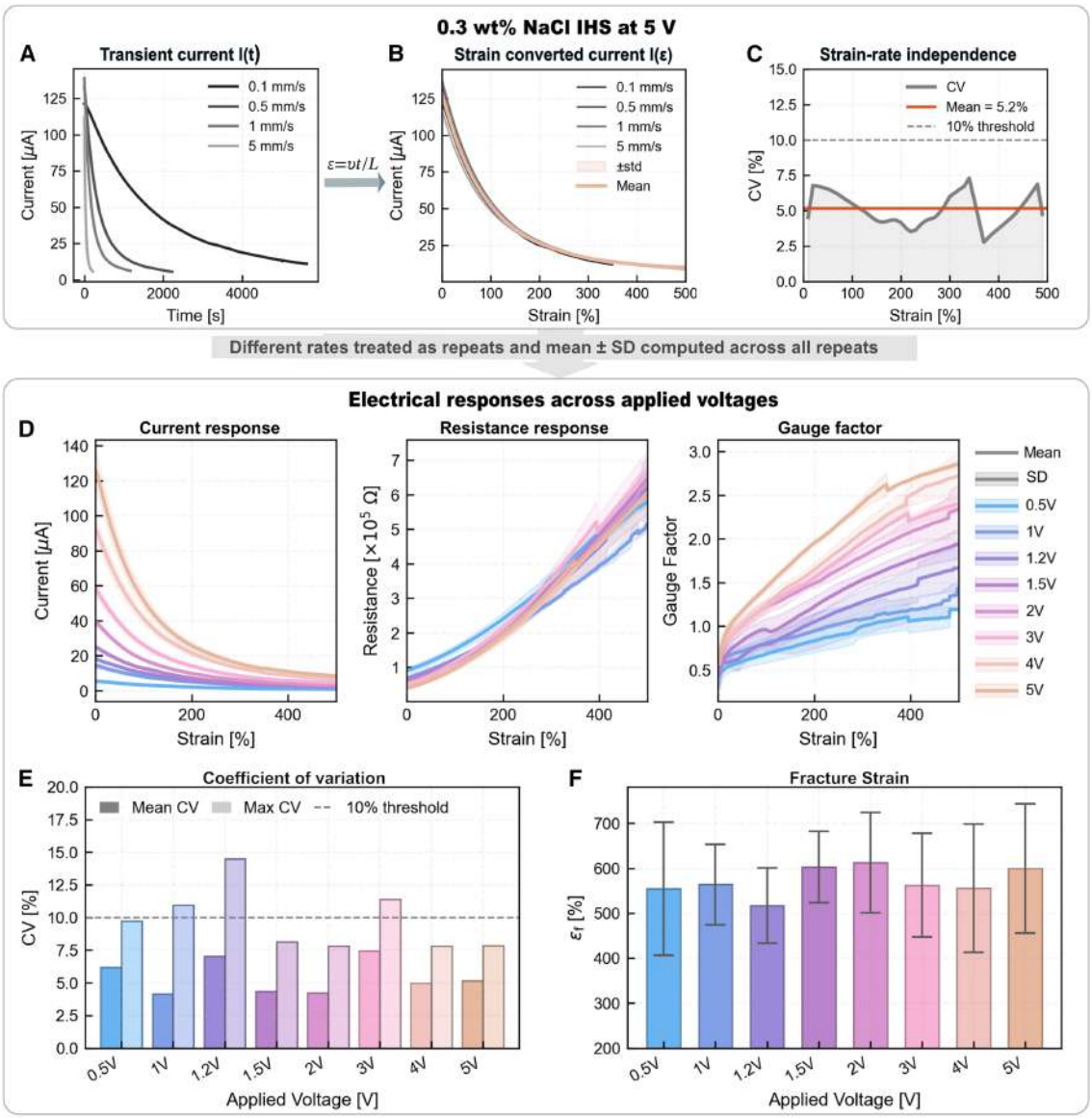

Figure 3. Electromechanical characterization of 0.3 wt % NaCl IHSs under uniaxial tension across voltages (0.5–5 V) and strain rates (0.1–5 mms^{-1})

(A–C) Effect of strain rate on the piezoresistive response, shown for the representative case of 0.3 wt % NaCl at 5 V. (A) Transient current responses $I(t)$ recorded across different strain rates. (B) Strain-dependent current $I(\varepsilon)$ derived via $\varepsilon = vt/L$, showing individual traces for all four strain rates together with the mean ± SD. (C) Coefficient of variation (CV) of resistance across strain rates as a function of strain, with a mean CV of 5.2% (n = 4).

(D) Representative electrical responses of IHSs (0.3 wt % NaCl). Current-strain $I(\varepsilon)$ (left), resistance-strain $R(\varepsilon)$ (middle), and GF-strain GF(ε) (right) across the test voltages.

(E) Mean and max CV of resistance as a function of applied voltages, with the 10% reference threshold indicated.

(F) Fracture strain ε_f as a function of applied voltage.

In all images, data are presented as mean ± SD (n = 4 strain rates); solid lines and shaded regions represent the mean and SD, respectively.

bound for extreme deformation scenarios. Across all tested conditions, GF spans from below 0.3 (high salt, low voltage) to approximately 1.4 (low salt, high voltage), highlighting the necessity of multi-parameter optimization rather than single-factor tuning.

Signal stability is evaluated using the mean coefficient of variation (CV) of resistance across all tested strain rates (Figure 4C). Over the full parameter space, the mean CV is 6.5%, with 84% of conditions satisfying the CV <10% threshold. To further quantify these independent contributions, column and row means were extracted to assess the separate effects of voltage and salt concentration (Figure S10, Supplemental Information). Higher applied voltages consistently reduce strain-rate dependence, while moderate salt concentrations further stabilize conductive

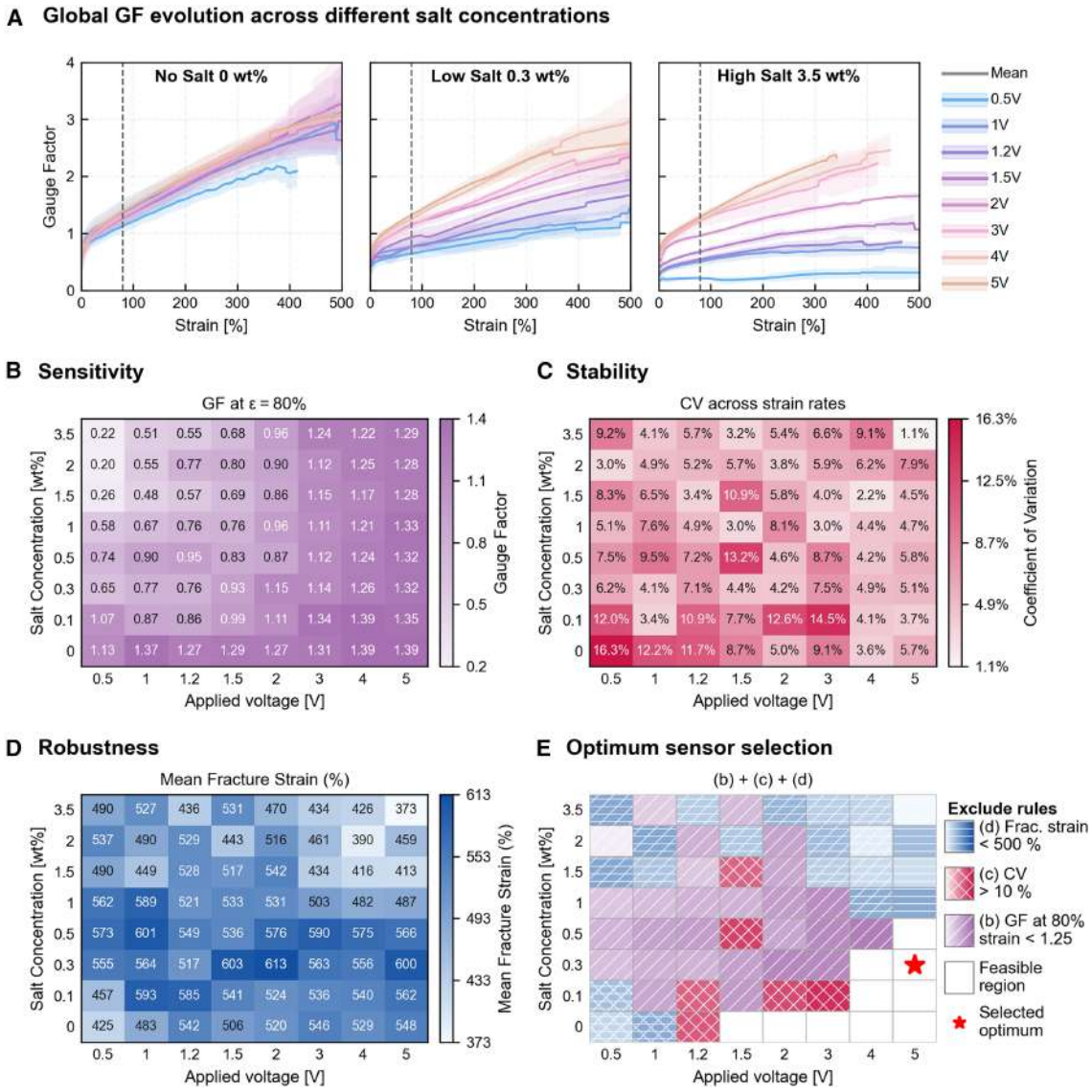

Figure 4. Multi-parameter maps for identifying the optimal IHS condition

(A) Full range GF evolution under different salt concentrations and applied voltages. The three representative salt concentrations (0, 0.3, and 3.5 wt %) illustrate the overall electromechanical response across the full strain range. In all plots, data are presented as mean ± SD (n = 4 strain rates); solid lines and shaded regions represent the mean and SD, respectively.

(B) GF at 80% strain, selected as a conservative upper-bound deformation level for comparing the sensitivity of candidate formulations.

(C) Mean coefficient of variation (CV), used to evaluate signal stability, where lower values indicate weaker strain rate dependence.

(D) Mean fracture strain, used as a robustness criterion, where higher values indicate better mechanical tolerance before failure.

(E) Final optimum IHS selection map, obtained by combining the exclusion criteria from sensitivity, stability, and robustness. Parameters with GF at 80% strain below the predefined threshold (1.25), mean CV at or above the stability threshold (10%), or mean fracture strain below the robustness threshold (500%) are excluded. The remaining feasible region is shown in white, and the selected optimum is marked by the red star. Overlapping shaded cells indicate exclusion by multiple criteria.

pathways. This stabilizing role of mobile ions in reducing rate-dependent variability is consistent with prior observations in ionic conductive hydrogels[41] and ionogel-based strain sensors.[40] In contrast, salt-free and very low-salt hydrogels operated at low voltages approach the instability threshold, making them less suitable for reliable calibration under variable actuation speeds.

Mechanical robustness is assessed through the mean fracture strain (Figure 4D). Increasing NaCl concentration leads to a systematic reduction in extensibility, reflecting progressive network stiffening and brittleness induced by high ionic strength. The fracture behavior of IHS exhibits a coupled dependence on both ionic content and applied voltage, reflecting a balance between network stabilization and electrically induced degradation

mechanisms. With increasing salt concentration, a general reduction in fracture strain is observed, although the salt-free sample does not exhibit the highest extensibility. This suggests that low ionic content may help homogenize stress transfer within the network and enhance energy dissipation through reversible ionic interactions, whereas the absence of mobile ions results in a more heterogeneous and mechanically less resilient network.[43] At higher concentrations, this beneficial effect is outweighed, likely because excessive ionic strength progressively screens and weakens the original physical interactions and crosslinking within the network, thereby rendering the hydrogel more brittle.[34] This trend is consistent with previous reports showing increased elastic modulus and reduced fracture strain in ion-rich hydrogel networks.[44] Although higher applied voltages enhance piezoresistive sensitivity, they further reduce fracture strain at elevated salt concentrations, likely due to concurrent mechanisms including accelerated water loss under an applied electric field,[45] electrically induced electrochemical reactions, and Joule heating-driven disruption of hydrogen-bonded junctions and triple-helix domains within the polymer network.[46]

These competing effects are consolidated in Figure 4E, where optimum IHS candidates are identified through simultaneous threshold criteria based on sensitivity, signal stability, and mechanical robustness (Figures 4B–4D). In particular, formulations with a GF below 1.25 at $\varepsilon = 80\%$, a mean CV at or above 10%, or a mean fracture strain below 500% are excluded. This screening significantly narrows the feasible design space to a small subset of low-salt, high-voltage conditions. Salt-free and 0.1 wt % NaCl formulations are further excluded on practical grounds, as their high steady-state resistance yields operating currents close to the noise floor (Figure S7, Supplemental Information), thereby imposing stringent requirements on readout circuit design and noise suppression. Among the remaining candidates, 0.3 wt % NaCl at 4–5 V and 0.5 wt % NaCl at 5 V hydrogels operated exhibit comparable signal stability and strain-rate independence. The final selection is therefore governed by sensitivity-durability trade-offs. Operation at 5 V consistently maximizes GF across the strain range (Figure 4A), while the 0.3 wt % formulation at the selected 5 V preserves a higher mean fracture strain than 0.5 wt % (Figure 4D), offering greater tolerance to large deformation and repeated loading. Accordingly, 0.3 wt % NaCl at 5 V is identified as the optimal operating condition, providing the best balance between piezoresistive sensitivity, signal stability, mechanical robustness, and electrical compatibility.

To enable quantitative mapping between electrical output and strain, the resistance-strain relationship $R(\varepsilon)$ was further characterized by fitting a parabolic and a cubic model to all experimental data. Both models achieved good fit across all test conditions ($R^2 > 0.99$) while the cubic model yielded a marginally higher and more consistent R^2 (0.9995 ± 0.0007) compared with the parabolic model (0.9988 ± 0.0017). Additionally, the leading cubic coefficient was found to be negligibly small, indicating that the additional model complexity of the cubic term only contributes marginally to the fit. The parabolic model was therefore selected as the calibration function for subsequent analyses, with fitted coefficients and detailed model comparison provided in Figures S14–S16 and discussed in Note S2 (Supplemental Information).

On this basis, the optimized IHS formulation (0.3 wt % NaCl, 5 V) is carried forward to the following subsection, where its integration onto a soft robotic endoscope is addressed in detail, including adhesion optimization, dehydration management, and in-system signal stability under actuation. Its performance is then validated through dynamic characterization and continuous 3D shape reconstruction experiments, directly linking the material-level design space established here to system-level proprioceptive performance.

Application in 3D shape reconstruction

System integration and optimization

Building on the optimized IHS formulation, this section addresses the practical integration challenges, including dehydration-induced signal degradation and interfacial adhesion, with the full methodology and experimental platform illustrated in Figure 5. To achieve reliable system-level integration, the signal acquisition workflow was first designed (Figure 5A). In brief, a pressure controller delivered programmed pneumatic inputs $P_{set,i}$ to the three actuator chambers, with the corresponding feedback pressures $P_{fb,i}$ measured internally and logged alongside $P_{set,i}$ to the processing computer. The three IHS signals (S_1, S_2, and S_3) were simultaneously collected and conditioned through a signal acquisition circuit (Figure S18, Supplemental Information) and digitized via an Arduino, to produce voltage outputs V_i (i = 1, 2, 3). In parallel, the ground-truth tip position information (M_x, M_y, M_z) was independently recorded via an EM tracker and streamed directly to the processing computer. The acquired voltage signals were subsequently pre-processed to extract the surface strains ε_i (Note S3), which were then used as inputs to the real-time 3D reconstruction algorithm for estimating the curvature κ. The position error e was used as the final output metric.

The soft pneumatic bending actuator was fabricated via silicone molding following our previously reported protocol in Shi et al.[10] with modifications to incorporate circumferential surface grooves for improved sensor adhesion (Figure S17, Supplemental Information). To enable multi-axis deformation sensing, three IHSs were mounted circumferentially on the actuator surface at equal 120° intervals, each at a radial distance of r = 8.5 mm from the neutral axis (Figure 5B). Under the constant-curvature assumption adopted in the shape reconstruction algorithm (Note S6), this symmetric three-sensor arrangement enables reconstruction of the two bending-curvature components of a single constant-curvature segment, while axial elongation is partially accounted for through common-mode strain (Equation S15). Torsion and spatially non-uniform curvature are not resolved by the present axial sensor layout. The designed angular positions were θ_i = 90°, 210°, 330°, with as-built positions measured after fabrication and recorded in Table S5 (Supplemental Information).

To ensure robustness of the device integration, the interfacial adhesion strength between the hydrogel sensor and the silicone surface was quantified via 90-degree peeling tests, adapted from the methodology reported in Shi et al.[47] A mixed composite adhesive comprising silicone adhesive and Ethyl cyanoacrylate (ECA) was prepared, with the ECA weight fraction (from 0 to 100 wt %) systematically varied to investigate its effect on

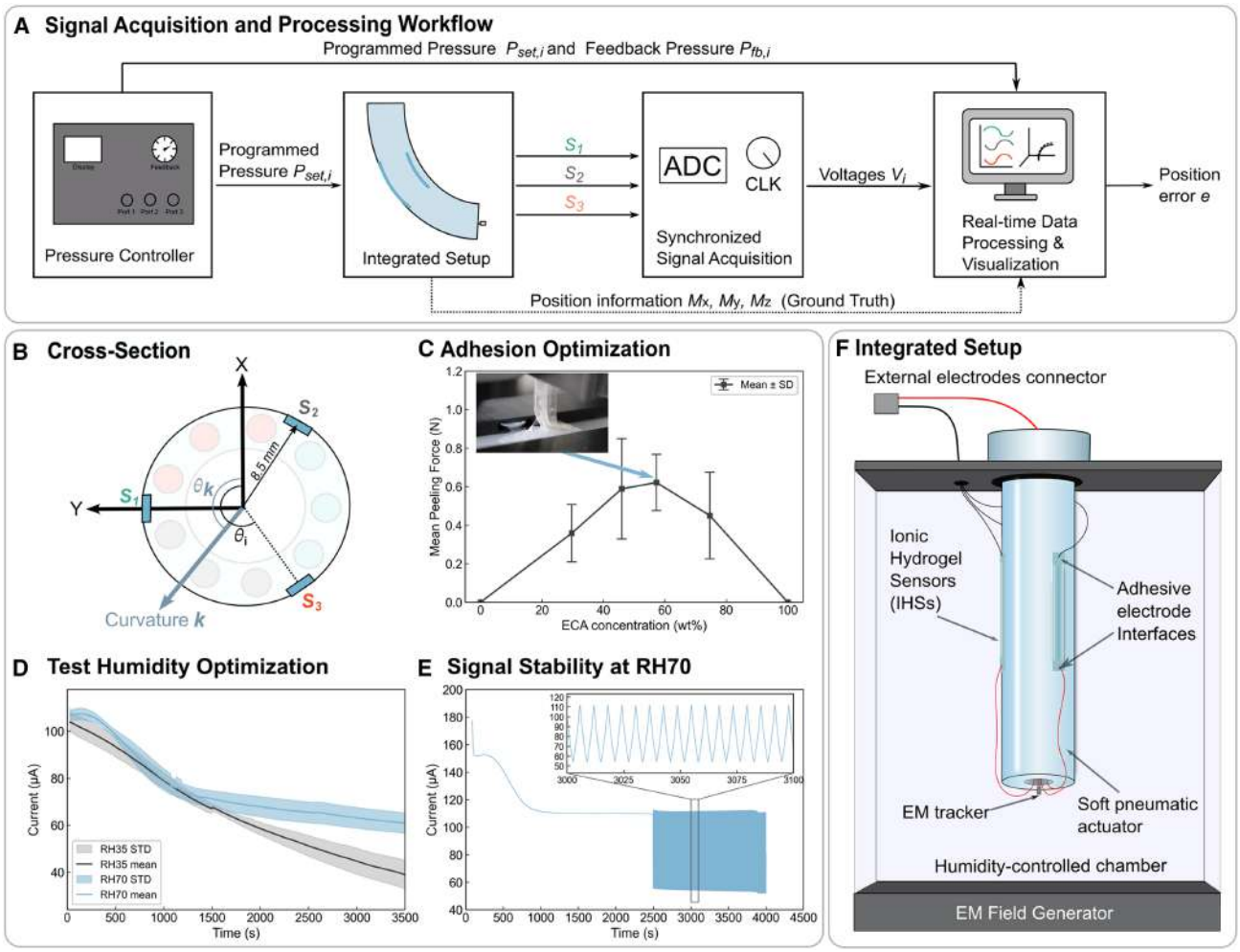

Figure 5. Integrated experimental platform and test methodology

(A) Hardware setup for signal acquisition and real-time 3D reconstruction, with programmed pressure input $P_{set,\ i}$, synchronized IHS voltage outputs V_i, EM-tracked ground truth (M_x, M_y, M_z), and position error e as output.

(B) Cross-sectional schematic showing three strain sensors arranged circumferentially at 120° intervals for bending-direction and curvature reconstruction.

(C) Quantitative analysis of adhesion strength as a function of ECA concentration (mean ± SD), with the optimum formulation identified at 60 wt % ECA. The inset shows a photograph of the adhesive interface during the peeling test.

(D) IHS (0.3 wt % NaCl, 5 V) electrical response at controlled humidity levels (35% RH and 70% RH), showing the effect of local environmental humidity on sensing performance. Solid lines and shaded region show the mean ± SD.

(E) Current-time trace of an IHS (0.3 wt % NaCl, 5 V, 70% RH) over the full test duration, with the blue-shaded region indicating the stabilized window selected for cyclic loading. Inset: expanded view confirming periodic current variation with minimal drift.

(F) Schematic of the experimental platform setup. IHSs are attached to the surface of a soft pneumatic actuator via adhesive electrode interfaces and connected to external electrode connector. The actuator is placed inside a humidity-controlled chamber, and an electromagnetic (EM) tracking system is used for ground-truth position measurement.

peeling force (Figure 5C). Below 60 wt % ECA fractions, the average peeling force increased with increasing ECA concentration. However, the mean peeling force decreased with increasing ECA percentage above 60%. The observed composition-dependent adhesion behavior may be attributed to the dual-network structure formed between the hydrogel and silicone substrate. Upon contact with the hydrogel, residual water and polar functional groups (–OH and $–CONH_2$) initiate rapid polymerization of ECA, forming a rigid poly(ethyl cyanoacrylate) (PECA) phase at the hydrogel interface. Any local penetration is expected to be confined to the superficial interfacial region, forming a thin PECA/hydrogel interpenetrating zone rather than bulk diffusion into the hydrogel. Meanwhile, the silicone-ECA component cures into a compliant siloxane-based network compatible with the PDMS substrate. Within the interfacial region, the PECA phase and the curing silicone network form a physically interpenetrated structure that bridges the hydrogel and elastomer surfaces. At an insufficient ECA fraction, limited PECA formation reduces interfacial anchoring density, resulting in weak adhesion (Figure S19d(i), Supplemental Information).

Conversely, excessive PECA content introduces brittleness, which may compromise mechanical robustness and long-term signal stability (Figure S19d(iv), Supplemental Information). An intermediate composition of 60 wt % ECA thus yielded the maximum peel strength, representing the optimal balance between interfacial anchoring and mechanical compliance (Figure 5C, inset; Figure S19d(ii), Supplemental Information). The 60 wt % ECA formulation was therefore selected for all subsequent actuator integration experiments.

To identify suitable operating conditions for endoscopic deployment, the electrical stability of IHSs (0.3 wt %, 5 V) was evaluated under two relative humidity (RH) levels, 35% RH and 70% RH, representing ambient laboratory conditions and a locally humidified condition relevant to moisture-rich endoscopic environments, respectively (Figure 5D). Under ambient conditions (35% RH), the output current decreased by approximately 60% over 1 h. In contrast, under controlled humidification at 70% RH, the sensor output underwent an initial humidity-equilibration transient for approximately 1200 s before entering a stable operating window, with a baseline drift of only) 0.56% over the subsequent 20 min (Figure S20b(ii), Supplemental Information), confirming that sustained humidity control is essential for reliable signal stability. To further evaluate sensor-level dynamic stability, cyclic loading to 80% strain was initiated only after the chamber had reached the target humidity and the sensor output had stabilized, allowing drift to be quantified within the stable operating window rather than during the initial equilibration transient (Figure 5E). During 200 cycles, the unstrained baseline current drifted by only) 0.16%, while the relative current response remained at 50.3 ± 0.6% (Figure S20b(iii), Supplemental Information). These results demonstrate that the IHS remained electrically stable under repeated loading over a time frame relevant to the typical 0.5–1 h duration of an endoscopic procedure.[48] To further assess device-level stability, the soft steering tip with integrated IHS was cyclically actuated between 0 and 2.5 bar at 0.1 Hz under humidity-controlled conditions. The test was also performed continuously for 1 h, corresponding to 358 strain-unstrain cycles. The baseline drifted by) 1.09%, while representative early, middle, and late cycle waveforms showed highly consistent signal amplitudes and shapes, demonstrating good sensing system stability over durations relevant to the intended endoscopic procedure (Figure S21b, Supplemental Information). Although electrolytic reactions may occur at the electrode-hydrogel interface under 5 V, long-term electrode degradation is not a concern given the single-use disposable design, and the fully integrated setup will be encapsulated within a non-conductive and airtight protective sheath to isolate the IHSs from direct contact with tissue and luminal fluid for final deployment. Accordingly, 70% RH was selected for all subsequent experiments.

Finally, the soft pneumatic actuator with embedded IHSs, humidity control, and EM tracker were integrated as illustrated in Figure 5F, with the complete experimental platform photographed in Figure S21 (Supplemental Information). Each sensor was seated within a surface groove on the outer wall of the actuator and bonded only at the two ends using the optimized adhesive formulation, leaving the central gauge section adhesive-free so that any local ECA-induced interfacial modification remained confined to the anchoring regions rather than the strain-sensing region. Reliable electrical contact between the sensors and the readout circuit was achieved through wire soldering to the electrode interfaces. The fully assembled system was enclosed within a humidity-controlled chamber maintained at 70% RH to ensure signal stability throughout testing. To enable quantitative validation on shape reconstruction, an EM tracker was embedded at the distal tip of the actuator, providing real-time ground-truth position data referenced to the EM field generator below the setup.

Operational performance of embedded sensors

To comprehensively evaluate the in-system performance, the embedded IHSs were tested under realistic pneumatic loading conditions, covering both frequency-dependent and amplitude-dependent excitations (Figure 6). The dynamic electromechanical response of the IHS was first evaluated under sinusoidal pneumatic excitation across four frequencies (0.05, 0.10, 0.25, and 0.50 Hz) at a pressure amplitude of 1.5 ± 1 bar, with the programmed pressure inputs and sensor voltage readings presented in Figure 6A. These four frequencies were selected to cover the representative dynamic operating window of soft pneumatic actuators, which generally operate below 1 Hz due to the compressibility of the air and the viscoelastic behavior of the silicone body,[49,50] while remaining within the range where stable inflation-deflation behavior can be reliably achieved. Across all test frequencies, the sensor signal consistently trailed the applied pneumatic pressure profile, indicating a measurable phase lag between mechanical input and electrical output. The phase lag was quantified over nine cycles using a cycle-resolved peak detection method (Figure S22a; Note S4, Supplemental Information). The mean phase lag increased with excitation frequency, from 15.9°±10.2° at 0.05 Hz to 48.9°±9.5° at 0.50 Hz, with intermediate values of 29.0°±11.8° and 35.7°±13.4° at 0.10 and 0.25 Hz, respectively (Figure 6B; Figure S22b; Table S2, Supplemental Information). The progressive increase in the mean phase lag with excitation frequency indicates a frequency-dependent delay in the integrated actuator-sensor response. This delay may arise from coupled system-level factors, including compliance in pneumatic actuation, relaxation of the silicone actuator body, deformation of the hydrogel sensor, interfacial adhesion, and signal acquisition. Correspondingly, the time delay τ decreased from 940 ms at 0.05 Hz to 278 ms at 0.50 Hz, with intermediate values of 857 and 420 ms at 0.10 and 0.25 Hz, respectively (Figure S22c, Supplemental Information). The corresponding voltage amplitudes (ΔV), defined as the half peak-to-peak amplitude per cycle, are summarized in Figure 6C (left axis, column graph). Importantly, ΔV remained relatively stable at 0.05 and 0.10 Hz (0.255 ± 0.006 V and 0.251 ± 0.009 V, respectively), but decreased with further increasing the excitation frequency, from 0.178 ± 0.009 V at 0.25 Hz to 0.122 ± 0.007 V at 0.50 Hz. This reduction in ΔV at higher frequency was corroborated by EM tracker measurements, which independently tracked actuator tip displacement and confirmed a progressive reduction in the valley-to-peak 3D Euclidean displacement from 47.4 mm at 0.05 Hz to 19.7 mm at 0.50 Hz (Figure 6C, right axis, scatterplot; Table S2, Supplemental Information). The close agreement between ΔV and the EM-tracked 3D tip displacement across all tested frequencies

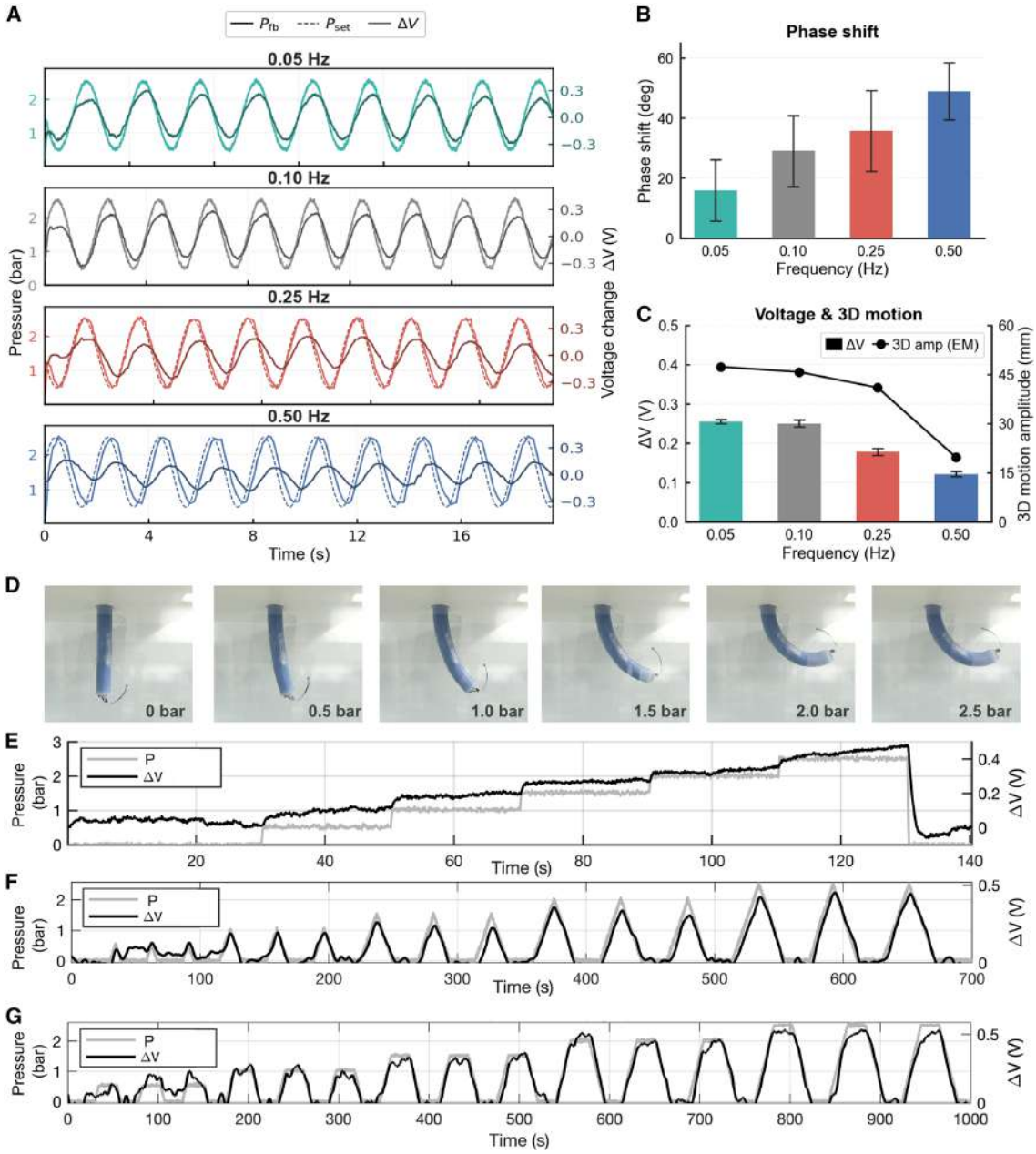

Figure 6. Signal responses of integrated sensor on soft robotic endoscope under variation of pneumatic actuation

(A) Time-domain responses of the strain sensor voltage to sinusoidal pneumatic pressure inputs at different actuation frequencies (0.05, 0.10, 0.25, and 0.5 Hz).

(B) Summary of the phase shift between pressure and voltage responses as a function of actuation frequency. Bars show the mean and error bars indicate SD across the nine actuation cycles (n = 9).

(C) Voltage amplitude ΔV and EM-tracked 3D tip displacement amplitude as a function of actuation frequency. ΔV values represent the mean ± SD over nine actuation cycles (n = 9), and the 3D displacement amplitudes (line) were obtained from independent EM tracker measurements at each frequency.

(D) Sequential snapshots of the soft pneumatic actuator at applied pressures of 0, 0.5, 1.0, 1.5, 2.0, and 2.5 bar, illustrating the progressive bending deformation with increasing pressure input.

(E) Time-domain sensor responses under stepwise pressure inputs.

(F) Time-domain sensor response under triangular cyclic pressure inputs, demonstrating dynamic strain tracking during continuous loading and unloading.

(G) Time-domain sensor response under trapezoidal cyclic pressure inputs, incorporating a sustained hold phase to assess signal stability under quasi-static deformation.

confirmed that the IHS output faithfully tracked mechanical deformation of the actuator rather than responding directly to the programmed applied pressure.

The reliability of the embedded IHS sensing was further evaluated under three different loading profiles of single-chamber pressurization across 0–2.5 bar (Figure 6D), which were designed with increasing dynamic complexity: stepwise pressurization evaluated quasi-static hold behavior (Figure 6E), triangular waveforms introduced continuous dynamic cyclic actuation (Figure 6F), and trapezoidal waveforms combined dynamic actuation with sustained hold phases to assess both tracking ability and signal stability under prolonged deformation simultaneously (Figure 6G).

For stepwise pressurization, pressure was increased across five discrete levels (0.5, 1.0, 1.5, 2.0, and 2.5 bar) and held for 20 s at each step (Figure 6E). The sensor voltage output ΔV increased from 0.106 ± 0.009 V at 0.5 bar to 0.458 ± 0.012 V at 2.5 bar, closely following the applied pressure profile at each step, and the signal stabilized rapidly upon reaching each plateau. The baseline noise, quantified over the initial 0–30 s interval under zero pressure, had a standard deviation of 0.0147 V and a valley-to-peak amplitude of 0.0655 V (Figure S23b, Supplemental Information). The reading remained steady throughout the hold phase, with hold-phase standard deviations below 0.012 V, corresponding to about 2.5%–8.0% of the mean ΔV at each pressure level (Figure S23d; Table S3, Supplemental Information). The local signal-to-noise ratio (SNR), defined as the ratio of the mean voltage amplitude to its standard deviation within each hold window, increased from 12.4 at 0.5 bar to a plateau of 38 at pressures above 1.5 bar (Figure S23e, Supplemental Information), indicating that measurement reliability improves with actuation level and that the sensor operates well above the noise level within the effective operating range from 1 to 2.5 bar.

During cyclic loading, each of the five pressure levels (0.5, 1.0, 1.5, 2.0, and 2.5 bar) was repeated three times per waveform type. Triangular waveform (0 bar → P → 0 bar) was first applied to assess continuous strain tracking under repeated actuation cycles (Figure 6F). At 0.5 bar, the strain-induced electrical response showed insufficient resolution, with a noticeable cycle-to-cycle coefficient of variation (CV) of 62.8% (Figure S24c; Table S4, Supplemental Information). This is likely due to the small response amplitude at low actuation levels, where the signal becomes more susceptible to noise and to the intrinsic time-dependent response of the IHS. In practice, this low-pressure regime corresponds to minimal actuator deformation and is less relevant to the intended sensing task, which primarily targets larger bending states in the 1.0–2.5 bar range. At pressures greater than 1 bar, on the other hand, the sensor output reproducibly followed actuator deformation, resulting in a mean CV of 4.0% (Table S4, Supplemental Information). Trapezoidal waveforms (0 bar → P → hold 30 s → 0 bar) were then used to evaluate signal stability under combined dynamic actuation and sustained deformation (Figure 6G). Over pressures from 1.0 to 2.5 bar, the plateau ΔV was highly reproducible across cycles, with a mean CV below 8.3%. The hold-phase signal also remained stable, exhibiting consistently low within-cycle variation across all tested plateaus (Table S4, Supplemental Information).

Collectively, these results confirm that the sensor reading remained highly reproducible and strongly correlated with the pressure input for the soft actuator system across all waveform types with pressure levels between 1.0 and 2.5 bar.

Optimized 3D reconstruction

Finally, IHSs embedded in the soft actuator were calibrated locally and demonstrated for real-time 3D shape reconstruction (Figure 7). Owing to intrinsic device-to-device variability and adhesion-induced differences at the electrode interfaces, each sensing channel was first calibrated independently prior to every experiment. To achieve this, identical pneumatic inputs were applied to all three chambers, producing a uniform axial extension of the actuator and subjecting the attached IHSs to uniaxial tensile deformation (Figure 7A). The pressure profile (P_{set}) was programmed to monotonically ramp from 0 to 2.5 bar and back to 0 bar (Figure 7B). The resulting increase in output voltage and the strain (Δs) profiles upon the increasing pressure input were measured throughout the process (Figure 7C). The output voltages were subsequently converted to resistance, and a parabolic model was individually fitted to the $R(\varepsilon)$ data of each sensing channel (Figure 7D; Note S5, Supplemental Information). The fitted model was further applied up to 60% strain, extending beyond the directly calibrated range of 37.9% to predict sensor response across the full operational range of the IHS response during soft robotic steering. Given the validated accuracy of the parabolic model across the entire stretching-to-fracture strain range, its application up to 60% strain remains well within the established model range. Notably, all three channels achieved high goodness-of-fit ($R^2 > 0.97$), confirming robust mapping across channels despite sensor-to-sensor variations in sensitivity. The resulting sensor-specific calibration coefficients a_i, b_i, and c_i are summarized in Table S5 (Supplemental Information) and were subsequently used to convert raw voltage signals $V_i(t)$ into quantitative strain estimates $\varepsilon_i(t)$ for downstream curvature reconstruction.

Subsequently, reconstruction performance was validated by driving the actuator along a continuous circular trajectory in 3D space (Figure 7E), providing a controlled benchtop proof-of-concept for 3D steering reconstruction, similar to approaches adopted in works.[18,51,52] The voltage outputs of all three sensing channels were converted to strain signals using the individually calibrated curves. The resulting strain measurements and the applied pressure profiles are presented in Figure 7F, confirming that each channel reliably captured the cyclic deformation of the actuator. The strain signals from the three channels were subsequently used as inputs to the shape reconstruction algorithm, as described in Note S6. For the demonstration, the actuation frequency was approximately 0.033 Hz, and all three chambers were driven with the same period and fixed phase offsets. Because this low-frequency trajectory was close to the 0.05 Hz condition characterized in the dynamic characterization experiments, the corresponding delay ($\tau \approx 940$ ms) was adopted as a simplified fixed compensation term for this specific reconstruction experiment. As shown in Figure 7G, the reconstructed tip trajectory closely matched the EM-measured ground truth, with an initial 3D tip position error of 10.08% ± 5.51% of the actuator arc length (Figure 7H). Following application of a 0.94 s delay compensation, the error was reduced to 5.92% ± 3.82%,

CellPress
OPEN ACCESS

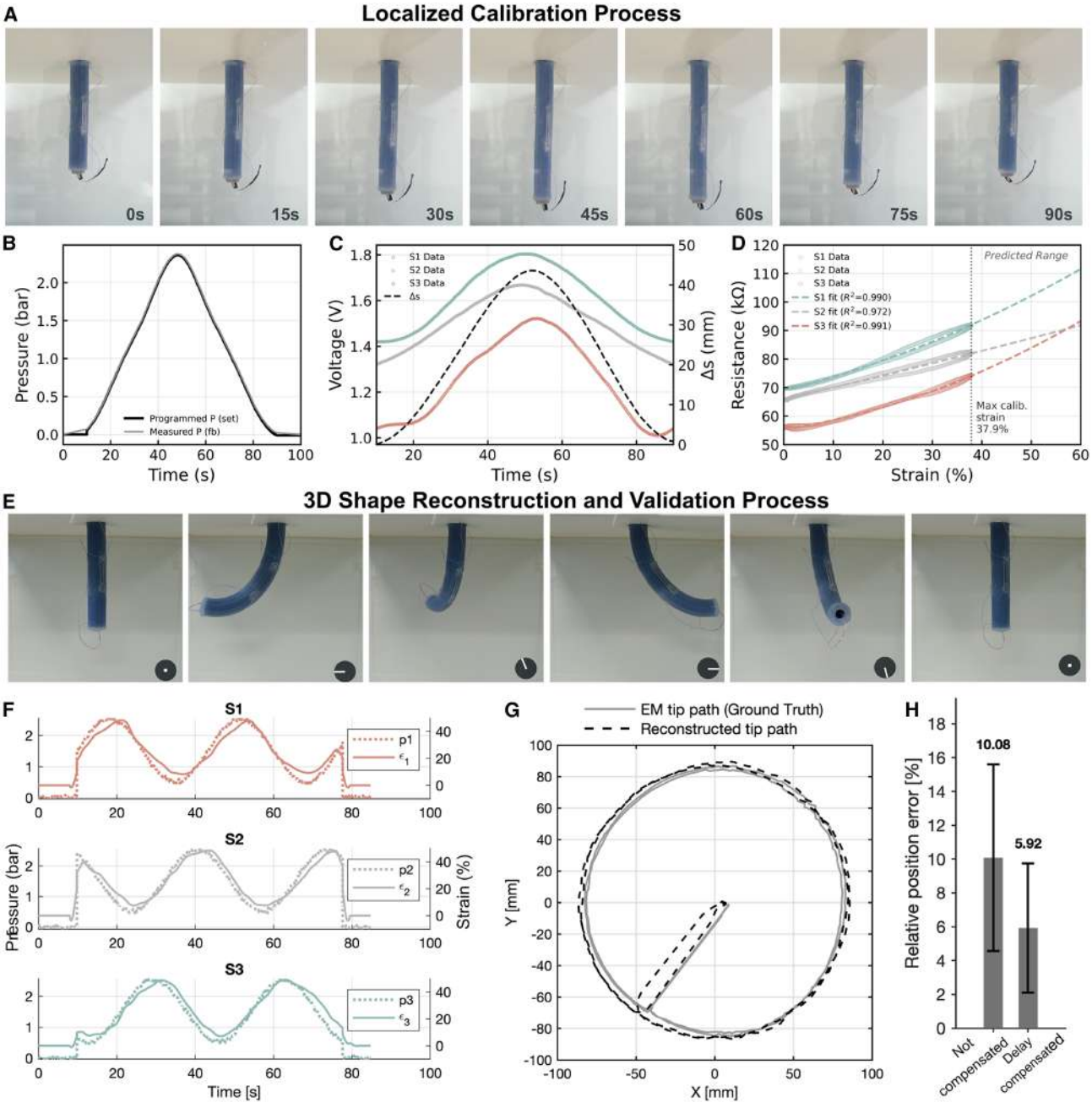

Figure 7. Application of localized calibration and shape reconstruction as well as validation process on a pneumatic soft actuator

(A) Representative sequence images showing the deformation of the soft actuator under programmed pressure input for localized sensor calibration.

(B) Programmed pressure input for localized sensor calibration.

(C) Voltage signals (V_i) were measured on the three sensors, and the corresponding surface strain was calculated based on the EM tracker signal. The voltages and strains were plotted against time, demonstrating a consistent trend alongside bending.

(D) Individual calibration curve. Dots show the synchronized resistance versus strain. Dashed lines show the quadratic fit calibration equation. The maximum achievable strain for this calibration process is 37.9%.

(E) Representative sequence images showing the 3D circle deformation process of the soft actuator under programmed pressure inputs.

(F) Time-synchronized actuation pressure and sensor signals, as well as the estimated surface strains, were plotted.

(G) Static reconstructed actuator tip trajectory and the ground truth electromagnetic (EM) tracking.

(H) Reconstructed tip position error estimation. Bars show the mean and error bar indicate SD, expressed as a percentage of the actuator length (%).

Table 1. Performance comparison of representative sensing strategies for soft robotic shape reconstruction and configuration sensing

Reference	Sensor	Method	Dim.	#Ch.	*E* (MPa)	Max strain (%)	Error (%)
Rigid optical sensing							
Moore et al.[53]	multicore FBG	Frenet-Serret	3D	3×*n*	–	–	7.2
Low-dimensional soft sensing							
Cheng et al.[24]	stick-on hydrogel strain sensor	single-sensor bending-angle estimation via resistance calibration	2D	1	∼0.05	>400	–
Yuen et al.[54]	graphite-silicone capacitive strain sensor	calibration-based finger angle reconstruction	2D	1	∼0.1–1*	∼375	–
Full 3D soft reconstruction							
So et al.[25]	resistive MWCNT-based silicone sensor	Frenet-Serret-based shape reconstruction	3D	3	–	30	∼11.5
–	–	–	–	9	–	–	∼4.45
Liu et al.[26]	CNT-IDE silicone capacitive strain sensor	model-based reconstruction	3D	12	–	∼200	<4
This work	ionic hydrogel	Frenet-Serret	**3D**	**3**	∼0.15	>500	**5.92**

Error is reported as a percentage of the arc length (tip position error unless stated otherwise). Entries are drawn from published reports rather than measurements on a common platform. Where possible, the comparison is method-matched: Moore and Rogge,[53] So et al.,[25] and this work use the Frenet-Serret formulation, and So et al.[25] use a three-channel configuration. Differences in actuator geometry, loading conditions, and sensor implementation mean that the reported errors should be interpreted as indicative rather than as a controlled benchmark. FBG, fiber Bragg grating; MWCNT, multi-walled carbon nanotube; CNT, carbon nanotube; IDE, interdigitated electrode; –, not reported or not directly comparable; #Ch., number of sensing channels; Dim., reconstruction dimensionality. *Estimated from the typical modulus range of silicone elastomers used in the sensor; not directly reported in the cited work.

corresponding to an absolute tip position error of 7.37 ± 4.76 mm (Table S6, Supplemental Information). This demonstrated that, for the fixed low-frequency trajectory used here, phase lag can be partially compensated through a lightweight fixed-offset correction without additional hardware modifications. The full shape reconstruction parameters and quantitative 3D tip reconstruction results, with and without time-delay compensation, are detailed in Tables S5 and S6 (Supplemental Information), respectively. Video S1 qualitatively compares the physical actuator motion with the real-time reconstructed constant-curvature backbone, while EM tracking quantitatively validates the distal-tip position.

Representative literature reports are summarized in Table 1 to contextualize the reconstruction performance. Because these studies use different actuator geometries, loading conditions, and sensing implementations, the comparison is indicative rather than a controlled side-by-side benchmark. The proposed system achieves a reconstruction error of 5.92%, comparable to the 7.2% reported for rigid multicore FBG sensors using a similar implementation of the Frenet-Serret method.[53] However, the stiffness and the limited strain compliance of the FBG-based systems restrict their mechanical compatibility with highly deformable soft robotic structures. Many advanced soft strain sensors have also been reported, such as stick-on hydrogel strain sensors[24] and elastomer-based capacitive sensors,[54] yet most demonstrated applications remain limited to 2D configuration sensing tasks such as bending detection or joint-angle estimation. In contrast, this work demonstrates full three-dimensional shape reconstruction, achieving 5.92% tip error with only 3 channels, outperforming the three-channel MWCNT-based silicone strain sensor work,[25] which reported ∼11.5% error under the same Frenet-Serret framework, and approaching its nine-channel result of ∼4.5%. The 12-channel CNT-IDE capacitive system[26] attains <4% via a model-based approach, yet requires four times more sensing channels. The competitive reconstruction accuracy with a minimal sensing channel count, low material cost, mechanical compliance, and fabrication simplicity of ionic hydrogel strain sensors collectively highlight their potential as disposable proprioceptive elements for soft robotic endoscopy.

Despite these advantages, the system-level evaluation identifies three sets of limitations, none of which arise primarily from the intrinsic electromechanical performance of the sensor itself. First, at the integration level, local humidity control was essential for long-term signal stability, and reliable adhesion to the actuator surface is required to maintain strain transfer and sensor durability. However, the present results are based on benchtop measurements performed in open space under ambient temperature (∼25°C) and controlled humidity (∼70% RH), rather than the confined, fluid-exposed intraluminal environment of the actual endoscopic operation. The sensors were tested unencapsulated. Although a non-conductive, airtight protective sheath is proposed to isolate the IHSs from luminal fluid and tissue contact in the final device (Figure 1A), the potential effect on sensor response of this encapsulation strategy has not yet been experimentally validated. In addition, the effect of physiological temperature (∼37°C) on sensor baseline and sensitivity, and whether it would require local recalibration, was not characterized. Second, at the model level, three co-located axial strain measurements under a constant-curvature assumption can resolve the two bending-curvature components and estimate

axial elongation through the common-mode strain term, but they cannot resolve twist or spatially non-uniform curvature. This limitation could be mitigated in future designs by incorporating sensing information beyond co-located axial strain, such as helical or off-axis sensor,[55] shear-sensitive sensors, or sensors distributed along the actuator length.[56] In parallel, the reconstruction model could be extended from a single-segment constant-curvature formulation to variable-curvature or Cosserat-rod-based models that explicitly include torsion and spatially non-uniform curvature.[57] To assess the potential effect of torsion on reconstruction, a supplementary numerical torsion-sensitivity analysis was performed under a representative loading condition (Note S7, Figure S25; Table S7, Supplemental Information). Third, at the validation level, local compression, friction, and geometric confinement from surrounding tissue were also not reproduced, and validation in phantoms, *ex vivo* tissues, and *in vivo* environments remain outstanding.

Three directions remain for future work. From a hardware perspective, current reliable sensing was achieved over 1.0–2.5 bar, while lower pressures produced resistance changes close to the acquisition noise, limiting signal resolution. This may be improved through enhanced shielding, lower-noise readout electronics, and optimized electrode connections. From a software perspective, the frequency-dependent delay observed during dynamic actuation indicates that a single fixed delay may become insufficient under variable-frequency actuation, where it would introduce frequency-dependent phase error. Future work will therefore implement adaptive delay compensation, either by updating the delay from the estimated actuation frequency and measured phase lag or by using learning-based signal processing trained on synchronized pressure, sensor, and ground-truth motion data. From an application-validation perspective, the present study provides benchtop validation under controlled pneumatic actuation. During practical endoscopic navigation, interaction with the bowel wall may introduce local compression, friction-induced strain, asymmetric loading, and contact-induced torsion that are not explicitly resolved by the current constant-curvature reconstruction framework. Future work will therefore focus on improving robustness to contact-induced effects and integrating IHS-based shape sensing with closed-loop pressure control for soft steering-tip reconstruction and navigation guidance. Before practical disposable endoscopic use, the system will need to be validated in fluid-exposure, anatomically realistic phantoms, and contact-rich environments, followed by *ex vivo* and *in vivo* testing. Appropriate insulation and encapsulation of the IHSs will also be required to assess real-time proprioceptive performance and clinical feasibility.

To conclude, this work presents a systematic, end-to-end optimization framework for ionic hydrogel strain sensors intended for soft robotic endoscope shape reconstruction, spanning material formulation, electrical operating conditions, and system-level integration. Systematic material characterization revealed that NaCl concentration and applied voltage exert coupled effects on sensor performance: increasing salt concentration enhanced ionic conductivity but generally reduced mechanical toughness, while higher voltage amplified sensitivity but accelerated mechanical failure. These trade-offs were resolved through the joint application of three quantitative criteria: sensitivity (GF $\geq$ 1.25 at ε = 80%), strain rate independence (CV < 10%), and mechanical robustness (fracture strain $\geq$500%). Across the full parameter space tested, the low-salt and high-voltage combination (0.3 wt % NaCl, 5 V) is thereby identified as the optimal operating condition, offering the best compromise among piezoresistive sensitivity, relatively high material toughness, and minimal rate dependence. Beyond material characterization, this work also demonstrated their viability as functional sensing elements capable of delivering quantitative, low-latency strain deformation feedback on the targeted operating soft robotic endoscope platform. A three-channel IHS array was integrated onto the soft pneumatic actuator surface at 120° intervals, enabling 3D bending detection under controlled pneumatic actuation. Dynamic characterization under sinusoidal excitation (0.05–0.5 Hz) revealed a frequency-dependent time delay (max $\sim$0.9 s) between pressure input and signal output. A lightweight time-delay compensation algorithm was then developed and validated, reducing the phase-induced shape reconstruction error from 10.08% to 5.92% relative to the actuator arc length, corresponding to an absolute tip position error of 7.4 ± 4.8 mm, outperforming state-of-the-art soft hydrogel strain sensor-based approaches.

In this work, we have therefore made three primary contributions toward ionic hydrogel-based shape sensing for soft robotic endoscopy. First, we have performed a systematic optimization of sensor operating conditions, identifying an effective balance between sensitivity, strain-rate independence, and mechanical robustness across NaCl concentration, applied voltage, and loading rate. Second, we have demonstrated the practical integration of the optimized sensors into a soft pneumatic endoscope actuator, addressing key challenges in adhesion, dehydration management, and signal stability. Third, we have shown continuous low-latency shape reconstruction from three embedded sensors and quantified a clear reduction in reconstruction error through delay compensation. Collectively, these results establish a practical, promising pathway for using IHSs as a low-cost, mechanically compliant, and disposable sensing technology for future soft robotic endoscopic systems.

METHODS

Materials

Acrylamide (AAm), *N*,*N* -methylenebis(acrylamide) (MBA) (99%), sodium chloride (NaCl, BioXtra, $\geq$99.5%), 2-hydroxy-4'-(2-hydroxyethoxy)-2-methylpropiophenone (Irgacure 2959, 98%), polyvinyl alcohol (PVA, MW 85,000–124,000, 99+%, hydrolyzed) were purchased from Sigma-Aldrich (Merck KGaA, UK).

Preparation of PAAm/PVA-NaCl hydrogel mixtures

Building on the material compositions and synthesis methods proposed in the literature,[58] this study introduces modifications, including varied NaCl content and a UV polymerization fabrication approach. To improve tensile toughness and sensor durability, PVA chains were incorporated into the PAAm network via hydrogen bonding and physical entanglement, forming a semi-interpenetrating network (semi-IPN) structure. A 2.5 wt % PVA solution was first prepared by dissolving PVA powder in

deionized (DI) water at 95°C with continuous stirring for 2 h until complete dissolution, then cooled to room temperature prior to use. The gel precursor solution was subsequently prepared by combining the PVA solution with AAm, MBA, and Irgacure 2959 (photoinitiator [PI]) at fixed concentrations of 33, 0.05, and 0.05 wt %, respectively, based on total gel weight (Table S1, Supplemental Information). To investigate the effect of NaCl concentration on ionic strain sensor performance, eight hydrogel formulations were prepared with NaCl concentrations of 0, 0.1, 0.3, 0.5, 1.0, 1.5, 2.0, and 3.5 wt %. DI water was added to each formulation to balance the total mixture weight. The components were thoroughly mixed until a clear, homogeneous gel precursor solution was obtained.

Fabrication of IHS

Hydrogel samples were cast in transparent polydimethylsiloxane (PDMS) molds with strip dimensions of 35 mm × 5 mm × 1.5 mm (Figure S1, Supplemental Information). The gel precursor solution was carefully transferred into the mold cavities using a pipette. Clear acetate sheets were placed over the molds to prevent evaporation and preserve sample geometry during polymerization. The molds were then exposed to UV light using a UV transilluminator (UVP, Upland, CA, USA; 25 W) at maximum intensity for 10 min to ensure complete crosslinking. Following UV exposure, the cured hydrogel strips, together with the clear acetate sheets, were removed from the PDMS molds and stored in sealed bags for 24 h to allow complete polymerization within the gel matrix prior to testing. All formulations were characterized and deployed in their as-cured state, without post-fabrication equilibration in aqueous media. The composition variable therefore refers to the as-fabricated network formulation rather than the equilibrium-swollen state.

Electrical performance characterization setup

The electrical performance of the IHS was characterized using a high-precision linear displacement system with AUTOLAB potentiostat (Figure 2A). The IHSs were secured using specialized film grips with integrated high-purity aluminum electrodes, ensuring both mechanical stability and reliable ohmic contact under high-strain deformation. Uniaxial stretching was actuated by a ROBOTIS MX-106 motor, driven by a U2D2 Power Hub board and modulated via a custom MATLAB script to maintain precise strain rates. During the deformation process, the IHSs were subjected to a constant bias voltage, while the resulting current responses were captured by the instrument simultaneously.

To systematically investigate the effects of NaCl concentration, strain rate, and applied voltage on the piezoresistive response, IHS samples were stretched to failure across four strain rates (0.1–5 mm s^{-1}) under eight applied voltages (0.5–5 V). The corresponding current response $I(\varepsilon)$, resistance response $R(\varepsilon)$, initial resistance R_0, and steady-state resistance R_{ss} across the full parameter space are summarized in Figures S3–S7 (Supplemental Information), respectively. The gauge factor response GF (ε), grouped by NaCl concentration in Figure S8 and regrouped by applied voltage in Figure S9, decouples the voltage and concentration dependence. The strain-rate dependence of fracture strain is provided in Figure S11 (Supplemental Information).

To cross-validate the electrical characterization results and assess reproducibility across measurement platforms, IHS samples were additionally characterized using another precision electrical measurement instrument Keithley 4200-SCS parameter analyzer. Both instruments followed identical measurement protocols, and the resulting $I(\varepsilon)$ responses across the two platforms are compared in Figure S4 and discussed in Note S1 (Supplemental Information).

Mechanical test setup

The mechanical performance of IHS samples was characterized using an Instron 5433 universal testing machine. For tensile testing, two representative IHS formulations, salt-free (0 wt % NaCl) and high-salt (3.5 wt % NaCl), were mounted in film grips and subjected to uniaxial tensile loading at four strain rates (0.1, 0.5, 1, and 5 mm s^{-1}). The engineering stress-strain curves were extracted (Figure S12, Supplemental Information). Cyclic mechanical loading was further performed to evaluate hysteresis behavior and long-term fatigue performance, applying variable-amplitude cycling at 10%, 20%, 50%, 100%, and 200% strain and constant-amplitude cycling at 80% strain over multiple cycles, with load-extension curves and load-time traces recorded (Figure S13, Supplemental Information).

Humidity control test setup

A sealed glass tank was used as the humidity-controlled test chamber. The internal RH was maintained at the target level by a programmed humidifier, with the duty cycle adjusted to achieve either 35% RH (ambient laboratory conditions) or 70% RH (locally humidified conditions). RH was continuously monitored throughout each experiment using a ThermoPro hygrometer. The linear stage and motor unit were housed in a sealed protective box and positioned within the chamber to enable uniaxial stretching under controlled humidity conditions (Figure S20, Supplemental Information).

EM tracking for ground truth validation

An Aurora EM tracking system was employed to independently measure the actuator tip trajectory as ground truth. The EM data were temporally synchronized with the sensor signals and spatially aligned in MATLAB. The reconstructed tip trajectory was then directly compared with the EM measurements, enabling quantitative assessment of the strain-based 3D reconstruction accuracy. In addition to the quantitative distal-tip comparison, the time-varying reconstructed backbone was displayed synchronously with the physical actuator motion in Video S1 to provide qualitative visual validation of the whole-shape evolution.

RESOURCE AVAILABILITY

Lead contact

Requests for further information and resources should be directed to and will be fulfilled by the lead contact, Daniele Dini (d.dini@imperial.ac.uk).

Materials availability

This study did not generate new unique reagents. All chemicals are commercially available and listed in the methods.

Data and code availability

- All experimental data reported in this paper have been deposited at Helix (Imperial College London) and are publicly available (Helix: https://doi.org/10.82186/y9gt6-dgs21).
- All original code has been deposited at Helix (Imperial College London) and is publicly available (Helix: https://doi.org/10.82186/y9gt6-dgs21).
- Any additional information required to reanalyze the data reported in this paper is available from the lead contact upon request.

ACKNOWLEDGMENTS

The authors would like to acknowledge the support received from the Engineering and Physical Sciences Research Council (EPSRC), United Kingdom, via the Grant EP/X033546/1. S.C. acknowledges the Department of Mechanical Engineering at Imperial for supporting her PhD scholarship. D.D. also acknowledges the support of the Royal Academy of Engineering (RAEng) for the Shell/RAEng Research Chair in Complex Engineering Interfaces.

AUTHOR CONTRIBUTIONS

Conceptualization, S.C., J.A.K., and D.D.; methodology, S.C., J.S., L.T., J.A.K., and D.D.; software, S.C.; validation, S.C. and J.S.; formal analysis, S.C., J.A.K., and D.D.; investigation, S.C.; resources, F.R.y.B., J.A.K., and D.D.; data curation, S.C.; writing – original draft, S.C.; writing – review and editing, J.S., L.T., F.R.y.B., J.A.K., and D.D.; visualization, S.C.; supervision, J.A.K. and D.D.; project administration, F.R.y.B. and D.D.; funding acquisition, F.R.y.B. and D.D.

DECLARATION OF INTERESTS

The authors declare no competing interests.

DECLARATION OF GENERATIVE AI AND AI-ASSISTED TECHNOLOGIES IN THE MANUSCRIPT PREPARATION PROCESS

During the preparation of this work, the authors used Claude (Anthropic) in order to check grammar, improve readability, and assist with analysis code. After using this tool, the authors reviewed and edited the content as needed and take full responsibility for the content of the published article.

SUPPLEMENTAL INFORMATION

Supplemental information can be found online at https://doi.org/10.1016/j.xcrp.2026.103625.

Received: June 24, 2026
Revised: September 9, 2026
Accepted: October 9, 2026
Published: October 29, 2026

REFERENCES

1. Xi, Y., and Xu, P. (2021). Global colorectal cancer burden in 2020 and projections to 2040. Transl. Oncol. *14*, 101174. https://doi.org/10.1016/j.tranon.2021.101174.
2. Keum, N., and Giovannucci, E. (2019). Global burden of colorectal cancer: emerging trends, risk factors and prevention strategies. Nat. Rev. Gastroenterol. Hepatol. *16*, 713–732. https://doi.org/10.1038/s41575-019-0189-8.
3. Wang, Y., Huang, X., Cheryala, M., Aloysius, M., Zheng, B., Yang, K., Chen, B., Fang, Q., Chowdary, S.B., Abougergi, M.S., and Chen, S. (2023). Global increase of colorectal cancer in young adults over the last 30 years: an analysis of the global burden of disease study 2019. J. Gastroenterol. Hepatol. *38*, 1552–1558. https://doi.org/10.1111/jgh.16220.
4. Kim, H., Melio, A., Simianu, V., and Mankaney, G. (2025). Challenges and opportunities for colorectal cancer prevention in young patients. Cancers *17*, 2043. https://doi.org/10.3390/cancers17122043.
5. Rawla, P., Sunkara, T., and Barsouk, A. (2019). Epidemiology of colorectal cancer: incidence, mortality, survival, and risk factors. Prz. Gastroenterol. *14*, 89–103. https://doi.org/10.5114/pg.2018.81072.
6. Sherid, M., Samo, S., and Sulaiman, S. (2013). Complications of colonoscopy. In Colonoscopy and Colorectal Cancer Screening – Future Directions (IntechOpen).
7. Reumkens, A., Rondagh, E.J.A., Bakker, C.M., Winkens, B., Masclee, A.A.M., and Sanduleanu, S. (2016). Post-colonoscopy complications: A systematic review, time trends, and meta-analysis of population-based studies. Am. J. Gastroenterol. *111*, 1092–1101. https://doi.org/10.1038/ajg.2016.234.
8. Alian, A., Zari, E., Wang, Z., Franco, E., Avery, J.P., Runciman, M., Lo, B., Rodriguez y Baena, F., and Mylonas, G. (2023). Current engineering developments for robotic systems in flexible endoscopy. Tech. Innov. Gastrointest. Endosc. *25*, 67–81. https://doi.org/10.1016/j.tige.2022.11.006.
9. Khanicheh, A., and Shergill, A.K. (2019). Endoscope design for the future. Tech. Gastrointest. Endosc. *21*, 167–173. https://doi.org/10.1016/j.tgie.2019.05.003.
10. Shi, J., Borvorntanajanya, K., Chen, K., Franco, E., and Baena, F.R.y. (2025). Design, control, and evaluation of a novel soft everting robot for colonoscopy. IEEE Trans. Robot. *41*, 4843–4859. https://doi.org/10.1109/tro.2025.3595696.
11. Kim, N.G., Park, S., Seo, D., Lee, S., Yoon, H., Kim, J., and Ryu, J.-H. (2026). A soft growing robotic endoscope for painless and strain-free insertion. Soft Robot. *13*, 5–18. https://doi.org/10.1177/21695172251369693.
12. Manfredi, L., Capoccia, E., Ciuti, G., and Cuschieri, A. (2019). A soft pneumatic inchworm double balloon (spid) for colonoscopy. Sci. Rep. *9*, 11109. https://doi.org/10.1038/s41598-019-47320-3.
13. Del Bono, V., McCandless, M., Gerald, A., Capaldi, E., Pang, J., Muter, C., Baldiswieler, M., Aihara, H., and Russo, S. (2025). A soft robotic add-on for colonoscopy: increasing safety and comfort through force monitoring. npj Robot *3*, 15. https://doi.org/10.1038/s44182-025-00028-1.
14. Shi, C., Luo, X., Qi, P., Li, T., Song, S., Najdovski, Z., Fukuda, T., and Ren, H. (2017). Shape sensing techniques for continuum robots in minimally invasive surgery: A survey. IEEE Trans. Biomed. Eng. *64*, 1665–1678. https://doi.org/10.1109/TBME.2016.2622361.
15. Sahu, S.K., Sozer, C., Rosa, B., Tamadon, I., Renaud, P., and Menciassi, A. (2021). Shape reconstruction processes for interventional application devices: State of the art, progress, and future directions. Front. Robot. AI *8*, 758411. https://doi.org/10.3389/frobt.2021.758411.
16. Xu, L., Ge, J., Patel, J.H., and Fok, M.P. (2017). Dual-layer orthogonal fiber bragg grating mesh based soft sensor for 3-dimensional shape sensing. Opt. Express *25*, 24727–24734. https://doi.org/10.1364/OE.25.024727.
17. Zhou, K., Zhu, L., Sun, G., and He, Y. (2023). FBG-based 3d shape sensor based on spun multi-core fibre for continuum surgical robots. Appl. Phys. B *129*, 140. https://doi.org/10.1007/s00340-023-08082-z.
18. Roshanfar, M., Zhang, A., He, C., Hooshiar, A., Podolsky, D.J., Looi, T., and Diller, E. (2026). Learning-based modeling of a magnetically steerable soft suction device for endoscopic endonasal interventions. Mechatronics *116*, 103468. https://doi.org/10.1016/j.mechatronics.2026.103468.
19. Zhang, F., Hao, Y., Tian, A., Yang, Z., Zhang, B., Fukuda, T., and Shi, C. (2025). Wearable fiber bragg grating sensors for physiological signal and body motion monitoring: A review. IEEE Trans. Instrum. Meas. *74*, 1–24. https://doi.org/10.1109/tim.2025.3558819.
20. Franz, A.M., Haidegger, T., Birkfellner, W., Cleary, K., Peters, T.M., and Maier-Hein, L. (2014). Electromagnetic tracking in medicine–a review of

technology, validation, and applications. IEEE Trans. Med. Imag. *33*, 1702–1725. https://doi.org/10.1109/tmi.2014.2321777.

21. Stoll, J., Ren, H., and Dupont, P.E. (2012). Passive markers for tracking surgical instruments in real-time 3-d ultrasound imaging. IEEE Trans. Med. Imag. *31*, 563–575. https://doi.org/10.1109/TMI.2011.2173586.
22. Lobaton, E.J., Fu, J., Torres, L.G., and Alterovitz, R. (2013). Continuous shape estimation of continuum robots using x-ray images. In 2013 IEEE Int (Conf. Robot. Autom. (ICRA)), pp. 725–732.
23. Vandini, A., Bergeles, C., Glocker, B., Giataganas, P., and Yang, G.-Z. (2017). Unified tracking and shape estimation for concentric tube robots. IEEE Trans. Robot. *33*, 901–915. https://doi.org/10.1109/tro.2017.2690977.
24. Cheng, S., Narang, Y.S., Yang, C., Suo, Z., and Howe, R.D. (2019). Stick-on large-strain sensors for soft robots. Adv. Mater. Interfac. *6*, 1900985. https://doi.org/10.1002/admi.201900985.
25. So, J., Kim, U., Kim, Y.B., Seok, D.-Y., Yang, S.Y., Kim, K., Park, J.H., Hwang, S.T., Gong, Y.J., and Choi, H.R. (2021). Shape estimation of soft manipulator using stretchable sensor. Cyborg Bionic Syst. *2021*, 9843894. https://doi.org/10.34133/2021/9843894.
26. Liu, L., Huang, X., Zhang, X., Zhang, B., Xu, H., Trivedi, V.M., Liu, K., Shaikh, Z., and Zhao, H. (2025). Model-based 3d shape reconstruction of soft robots via distributed strain sensing. Soft Robot. *12*, 721–731. https://doi.org/10.1089/soro.2024.0158.
27. Khan, B., Abdullah, S., and Khan, S. (2023). Current progress in conductive hydrogels and their applications in wearable bioelectronics and therapeutics. Micromachines *14*, 1005. https://doi.org/10.3390/mi14051005.
28. Tang, L., Wu, S., Qu, J., Gong, L., and Tang, J. (2020). A review of conductive hydrogel used in flexible strain sensor. Materials *13*, 3947. https://doi.org/10.3390/ma13183947.
29. Wu, Z., Zhang, L., Wang, M., Zang, D., Long, H., Weng, L., Guo, N., Gao, J., Liu, Y., and Xu, B.B. (2025). A wearable ionic hydrogel strain sensor with double cross-linked network for human–machine interface. Adv. Compos. Hybrid Mater. *8*, 17. https://doi.org/10.1007/s42114-024-01083-2.
30. Zhang, J., Liang, Y., Deng, Z., Xu, H., Zhang, H., Guo, B., and Zhang, J. (2023). Adhesive ion-conducting hydrogel strain sensor with high sensitivity, long-term stability, and extreme temperature tolerance. ACS Appl. Mater. Interfaces *15*, 29902–29913. https://doi.org/10.1021/acsami.3c03624.
31. Zhao, L., Ke, T., Ling, Q., Liu, J., Li, Z., and Gu, H. (2021). Multifunctional ionic conductive double-network hydrogel as a long-term flexible strain sensor. ACS Appl. Polym. Mater. *3*, 5494–5508. https://doi.org/10.1021/acsapm.1c00805.
32. Wang, S., Sun, Z., Zhao, Y., and Zuo, L. (2021). A highly stretchable hydrogel sensor for soft robot multi-modal perception. Sensor Actuator A Phys. *331*, 113006. https://doi.org/10.1016/j.sna.2021.113006.
33. Shen, Z., Zhang, Z., Zhang, N., Li, J., Zhou, P., Hu, F., Rong, Y., Lu, B., and Gu, G. (2022). High-stretchability, ultralow-hysteresis conducting polymer hydrogel strain sensors for soft machines. Adv. Mater. *34*, 2203650. https://doi.org/10.1002/adma.202203650.
34. Song, H., Sun, Y., Zhu, J., Xu, J., Zhang, C., and Liu, T. (2021). Hydrogen-bonded network enables polyelectrolyte complex hydrogels with high stretchability, excellent fatigue resistance and self-healability for human motion detection. Compos. B Eng. *217*, 108901. https://doi.org/10.1016/j.compositesb.2021.108901.
35. Sun, J.-Y., Keplinger, C., Whitesides, G.M., and Suo, Z. (2014). Ionic skin. Adv. Mater. *26*, 7608–7614. https://doi.org/10.1002/adma.201403441.
36. Keplinger, C., Sun, J.Y., Foo, C.C., Rothemund, P., Whitesides, G.M., and Suo, Z. (2013). Strechable, transparent, ionic conductors. Science *341*, 984–987. https://doi.org/10.1126/science.1240228.
37. Yang, C., and Suo, Z. (2018). Hydrogel ionotronics. Nat. Rev. Mater. *3*, 125–142. https://doi.org/10.1038/s41578-018-0018-7.
38. Lei, H., Dong, L., Li, Y., Zhang, J., Chen, H., Wu, J., Zhang, Y., Fan, Q., Xue, B., Qin, M., et al. (2020). Stretchable hydrogels with low hysteresis and anti-fatigue fracture based on polyprotein cross-linkers. Nat. Commun. *11*, 4032. https://doi.org/10.1038/s41467-020-17877-z.
39. Hamilton, M., Sivasambu, H., Behdinan, K., and Andrysek, J. (2021). Evaluating the dynamic performance of interfacial pressure sensors at a simulated body-device interface. Can. Prosthet. Orthot. J. *4*, 36059. https://doi.org/10.33137/cpoj.v4i1.36059.
40. Zhang, H., Lowe, A., Kalra, A., and Yu, Y. (2021). A flexible strain sensor based on embedded ionic liquid. Sensors (Basel) *21*, 5760. https://doi.org/10.3390/s21175760.
41. Xin, Y., Liang, J., Ren, L., Gao, W., Qiu, W., Li, Z., Qu, B., Peng, A., Ye, Z., Fu, J., et al. (2023). Tough, healable, and sensitive strain sensor based on multiphysically cross-linked hydrogel for ionic skin. Biomacromolecules *24*, 1287–1298. https://doi.org/10.1021/acs.biomac.2c01335.
42. Qing, X., Liu, Z., Katsaounis, A., Bouropoulos, N., Taurino, I., and Fardim, P. (2024). Poly(vinyl alcohol)/pullulan/nacl conductive hydrogels with high strength and sensitivity for wearable strain sensors. ACS Appl. Polym. Mater. *6*, 8105–8115. https://doi.org/10.1021/acsapm.4c00935.
43. Sun, Y., Thakur, V.K., and Luo, R. (2024). High mechanical strength, strong adhesion, self-healing and conductive ionic hydrogels for motion detection. Polymer *299*, 126946. https://doi.org/10.1016/j.polymer.2024.126946.
44. Gao, X., Guo, C., Xu, S., and Song, H. (2024). Stretchable ionic conductive gels for wearable human-activity detection. Chem. Eng. J. *489*, 151231. https://doi.org/10.1016/j.cej.2024.151231.
45. Raza, S., Yang, C., Qian, X., and Liu, J. (2025). Oscillations in incident electric field enhances interfacial water evaporation. Mater. Horiz. *12*, 6774–6783. https://doi.org/10.1039/d5mh00353a.
46. Helseth, L.E. (2024). Humidity and heat transport during electrical heating of an ionic hydrogel. Int. J. Heat Mass Transf. *229*, 125713. https://doi.org/10.1016/j.ijheatmasstransfer.2024.125713.
47. Shi, Y., Liu, J., Li, J., Xiong, D., and Dini, D. (2022). Improved mechanical and tribological properties of PAAm/PVA hydrogel-Ti6Al4V alloy configuration for cartilage repair. J. Polym. Res. *29*, 515. https://doi.org/10.1007/s10965-022-03355-1.
48. Jain, D., Goyal, A., and Zavala, S. (2016). Predicting colonoscopy time: A quality improvement initiative. Clin. Endosc. *49*, 555–559. https://doi.org/10.5946/ce.2015.110.
49. Shi, J., Abad, S.-A., Dai, J.S., and Wurdemann, H. (2026). Compliance model-based contact force control for soft continuum robots. Soft Robot. *13*, 310–323. https://doi.org/10.1177/21695172261431194.
50. Fang, G., Chow, M.C.K., Ho, J.D.L., He, Z., Wang, K., Ng, T.C., Tsoi, J.K.H., Chan, P.L., Chang, H.C., Chan, D.T.M., et al. (2021). Soft robotic manipulator for intraoperative mri-guided transoral laser microsurgery. Sci. Robot. *6*, eabg5575. https://doi.org/10.1126/scirobotics.abg5575.
51. Tian, L., Zhao, J., Yang, Z., Chalau, V., and Temelkuran, B. (2025). Thermally drawn steerable soft robotic fiber for multi-purpose minimally invasive surgery. IEEE Rob. Autom. Lett. *10*, 12389–12396. https://doi.org/10.1109/lra.2025.3619706.
52. Abdelaziz, M.E.M.K., Zhao, J., Gil Rosa, B., Lee, H.-T., Simon, D., Vyas, K., Li, B., Koguna, H., Li, Y., Demircali, A.A., et al. (2024). Fiberbots: Robotic fibers for high-precision minimally invasive surgery. Sci. Adv. *10*, eadj1984. https://doi.org/10.1126/sciadv.adj1984.
53. Moore, J.P., and Rogge, M.D. (2012). Shape sensing using multi-core fiber optic cable and parametric curve solutions. Opt. Express *20*, 2967–2973. https://doi.org/10.1364/OE.20.002967.
54. Yuen, M.C.S., Lear, T.R., Tonoyan, H., Telleria, M., and Kramer-Bottiglio, R. (2018). Toward closed-loop control of pneumatic grippers during pack-and-deploy operations. IEEE Rob. Autom. Lett. *3*, 1402–1409. https://doi.org/10.1109/lra.2018.2800079.

55. Xu, R., Yurkewich, A., and Patel, R.V. (2016). Curvature, torsion, and force sensing in continuum robots using helically wrapped fbg sensors. IEEE Rob. Autom. Lett. *1*, 1052–1059. https://doi.org/10.1109/lra.2016.2530867.

56. Renda, F., Boyer, F., Dias, J., and Seneviratne, L. (2018). Discrete cosserat approach for multisection soft manipulator dynamics. IEEE Trans. Robot. *34*, 1518–1533. https://doi.org/10.1109/tro.2018.2868815.

57. Rucker, D.C., and Webster III, R.J. (2011). Statics and dynamics of continuum robots with general tendon routing and external loading. IEEE Trans. Robot. *27*, 1033–1044. https://doi.org/10.1109/tro.2011.2160469.

58. Ge, G., Zhang, Y., Shao, J., Wang, W., Si, W., Huang, W., and Dong, X. (2018). Stretchable, transparent, and self-patterned hydrogel-based pressure sensor for human motions detection. Adv. Funct. Mater. *28*, 1802576. https://doi.org/10.1002/adfm.201802576.

Cell Reports Physical Science, Volume *7*

Supplemental information

Ionic hydrogel sensors for low-latency high-accuracy 3D reconstruction of soft robotic endoscope

Shuhang Chen, Jialei Shi, Libaihe Tian, Ferdinando Rodriguez y Baena, Jang Ah Kim, and Daniele Dini

S1 Supplemental figures and tables

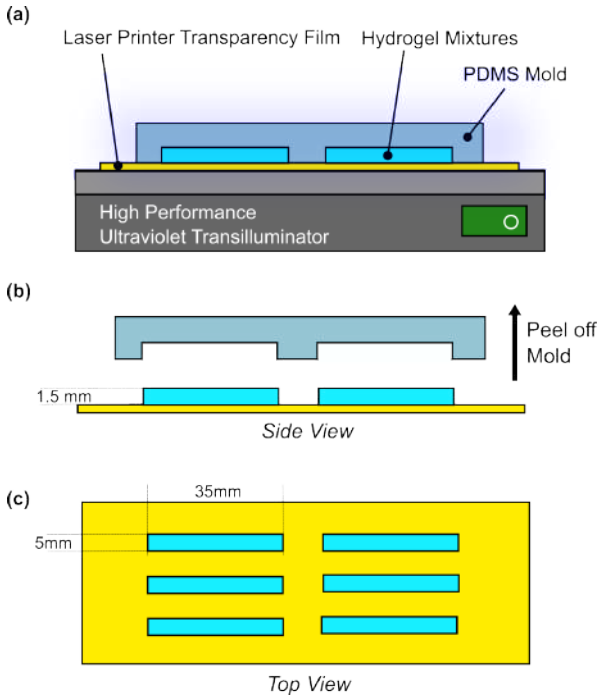

Figure S1: Fabrication of ionic hydrogel sensors (IHSs) via UV polymerization. (a) Cross-sectional illustration of the UV curing setup: hydrogel mixtures are cast into recessed cavities of a PDMS mold, covered with a laser printer transparency film to ensure sealing, and exposed to UV light from a High Performance UV Transilluminator beneath. (b) Side view schematic showing the IHS thickness of 1.5 mm following mold removal. (c) Top view schematic of the IHS product outcome layout, showing six strip-shaped IHS samples (35 mm × 5 mm each) per fabrication batch.

Label	AAm (wt%)	MBA (wt%)	PI (wt%)	PVA solution (wt%)	DI (wt%)	NaCl (wt%)	c_{NaCl} ($n_{\mathrm{NaCl}}/n_{\mathrm{AAm}}$) (mol/mol)
A	33	0.05	0.05	62.5	4.4	0	0
B	33	0.05	0.05	62.5	4.3	0.1	0.0037
C	33	0.05	0.05	62.5	4.1	0.3	0.0111
D	33	0.05	0.05	62.5	3.9	0.5	0.0184
E	33	0.05	0.05	62.5	3.4	1	0.0369
F	33	0.05	0.05	62.5	2.9	1.5	0.0553
G	33	0.05	0.05	62.5	2.4	2	0.0737
H	33	0.05	0.05	62.5	0.9	3.5	0.1290

Table S1: Composition of hydrogel formulations with different NaCl contents. $n_{\mathrm{NaCl}}/n_{\mathrm{AAm}}$ is the molar ratio of NaCl to acrylamide

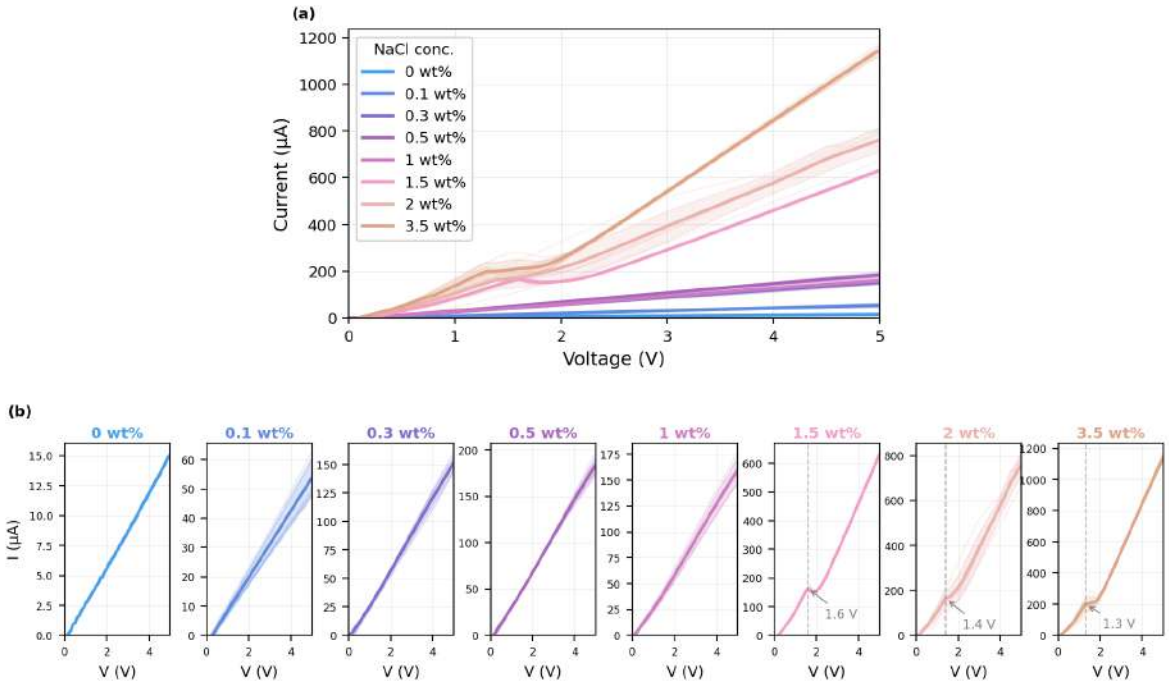

Figure S2: Linear sweep voltammetry (LSV) of IHS across varying salt concentrations. (a) Overlay of I-V curves for all eight samples (0–3.5 wt% NaCl), recorded from 0 to 5 V using the AUTOLAB potentiostat. Bold lines represent the mean current of the repeated measurements; shaded regions indicate ± one standard deviation. (b) Individual I-V curves for each sample. Dashed vertical lines in the 1.5, 2, and 3.5 wt% panels mark current transition (1.6, 1.4, and 1.3 V, respectively).

(a) $I(\varepsilon)$, 0–800%, Shared y-axis

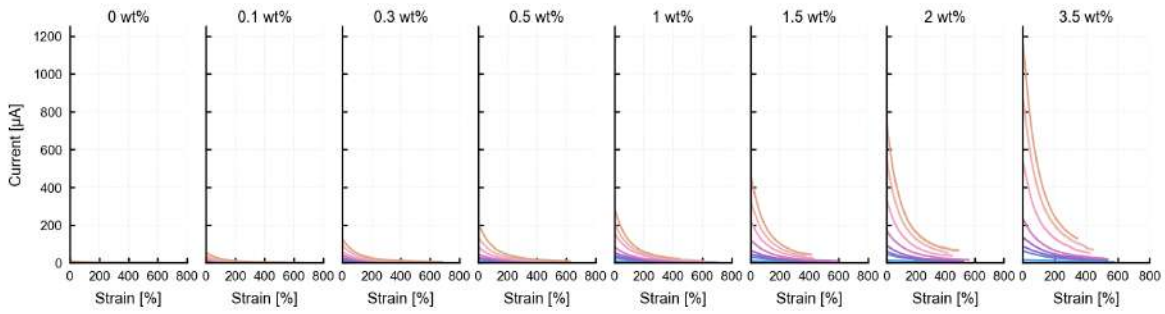

(b) $I(\varepsilon)$, 0–600%, Zoomed y-axis

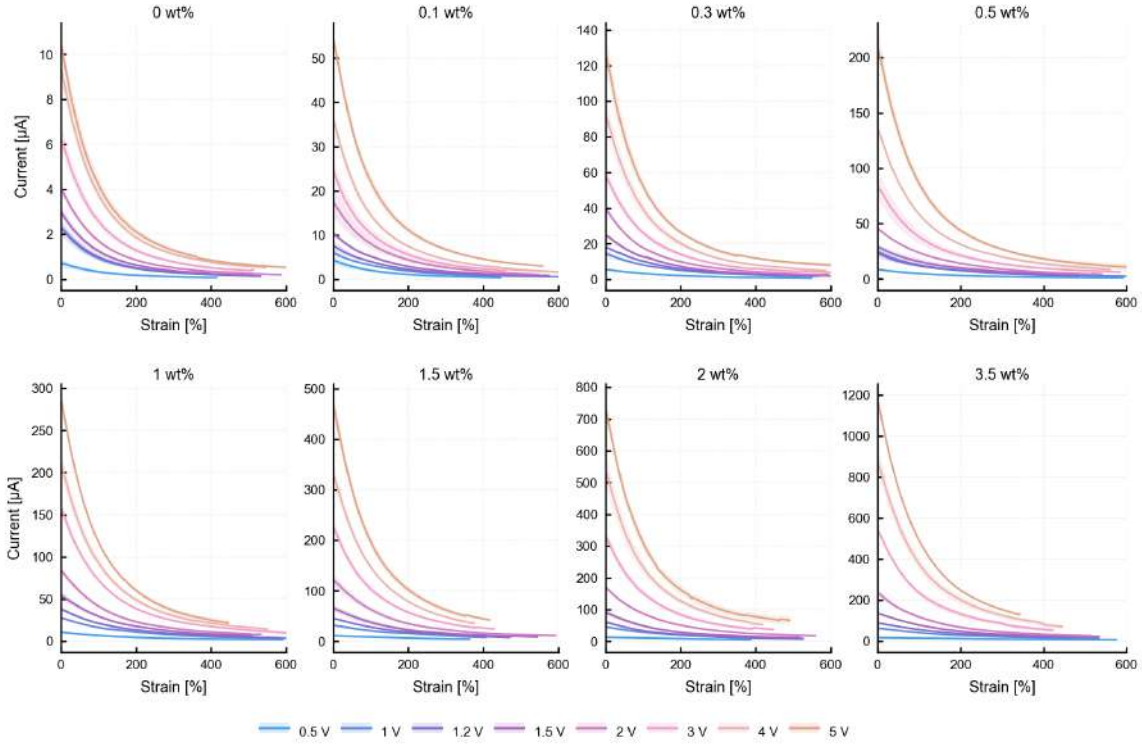

Figure S3: Strain-dependent current response $I(\varepsilon)$ across the full parameter space. (a) Overlay of all 64 current–strain curves (8 NaCl concentrations × 8 applied voltages) plotted on a unified axis, illustrating the wide dynamic range of the sensor output (0—1200 μA) with varying salt concentration; high-salt, high-voltage combinations yield the highest current change; the no-salt (0 wt%) and low-salt groups span the lowest current range. (b) Individual current response $I(\varepsilon)$ panels for each NaCl concentration (0—3.5 wt%). For each panel, the eight applied voltages (0.5—5 V) are shown in separate color-coded traces. Increasing salt concentration systematically elevates the absolute current.

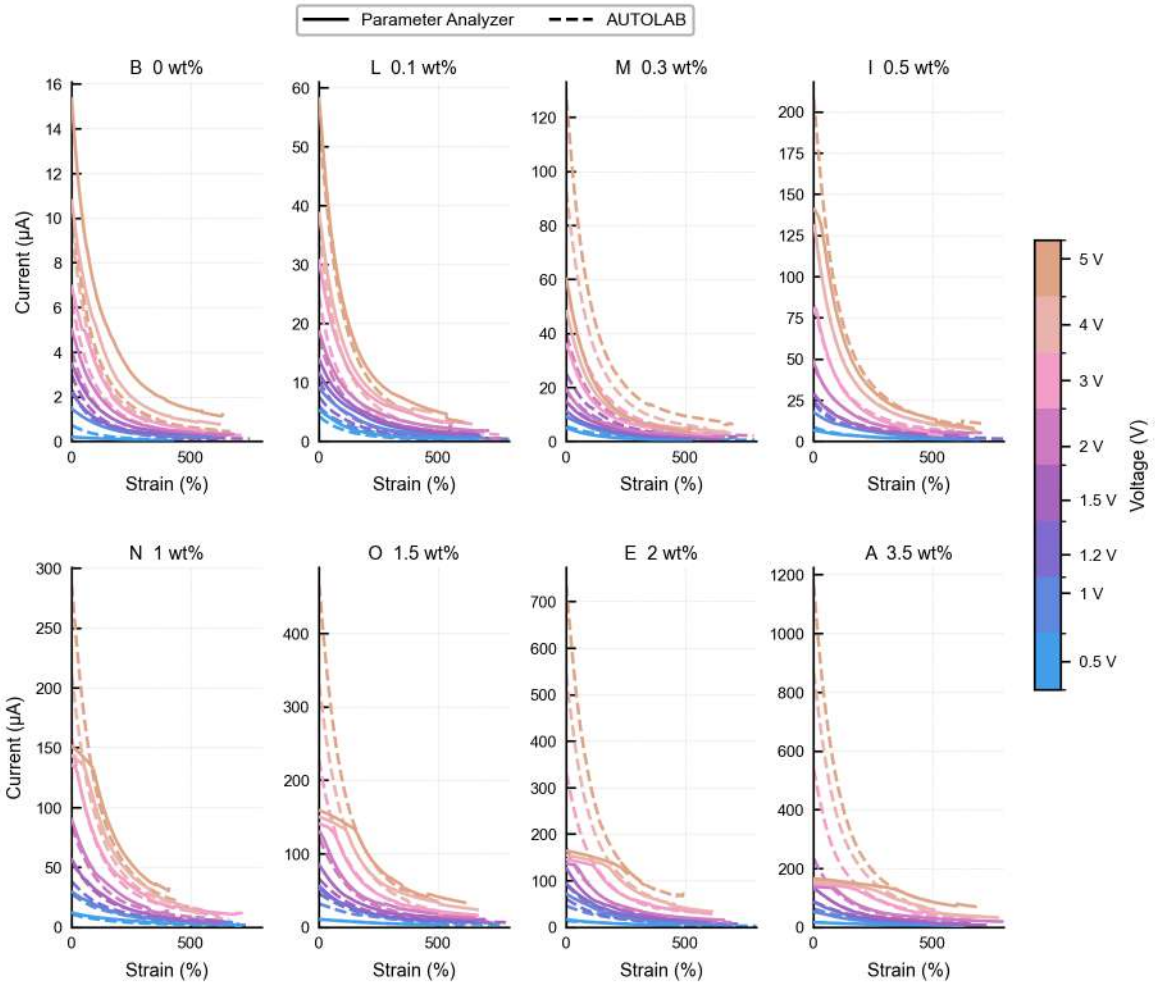

Figure S4: Cross-instrument validation of strain-dependent current responses $I(\varepsilon)$ across the full parameter space. Measurements from the Keithley 4200-SCS Parameter Analyzer (solid lines) are compared with those from the AUTOLAB potentiostat (dashed lines); each panel shows the mean current response across (n=4) repeated measurements.

(a) $R(\varepsilon)$, 0–800%, Shared y-axis

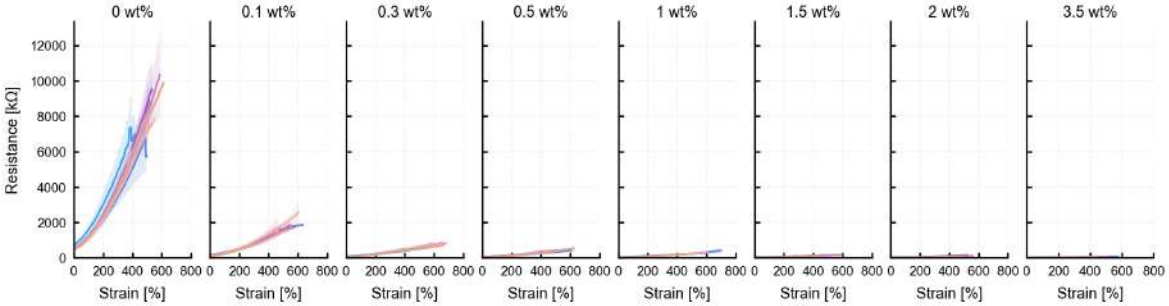

(b) $R(\varepsilon)$, 0–600%, Zoomed y-axis

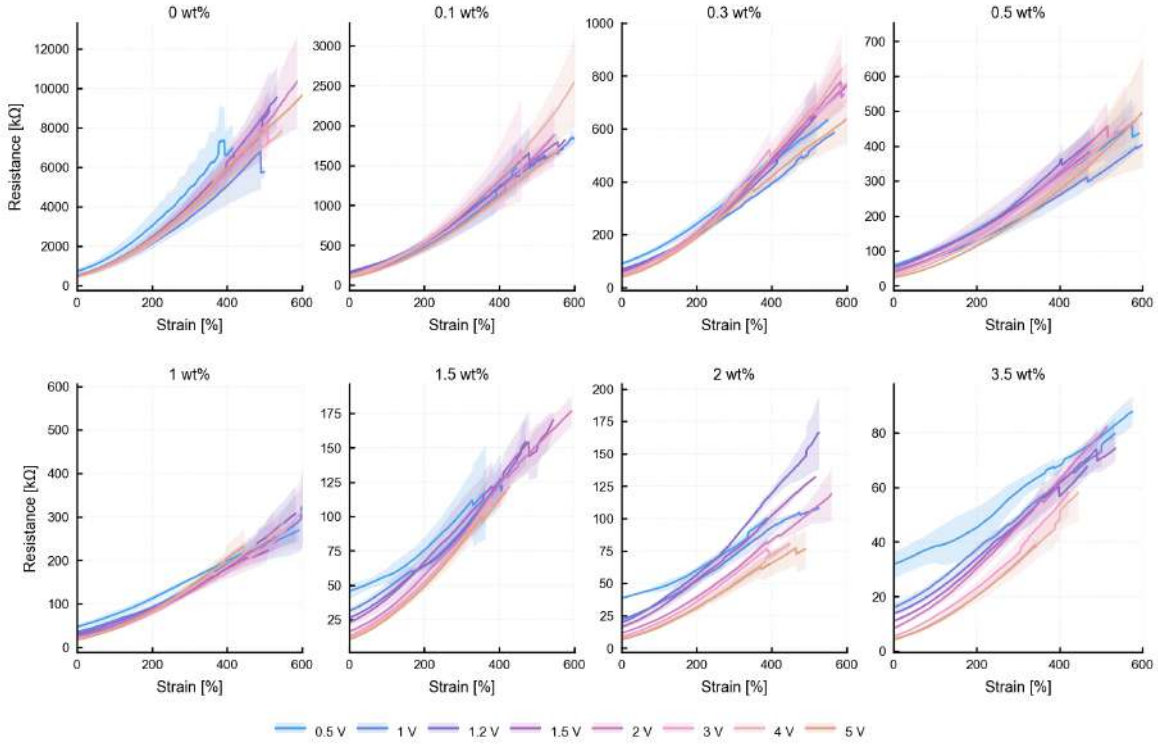

Figure S5: Strain-dependent resistance $R(\varepsilon)$ across the full parameter space. (a) Overlay of all resistance–strain $R(\varepsilon)$ curves on a unified axis (0–15,000 kohm), showing that salt-free and low-salt groups exhibit orders-of-magnitude higher baseline resistance than higher-salt formulations. (b) Individual resistance–strain panels for each NaCl concentration (0—3.5 wt%), with all eight applied voltages (0.5—5 V) color-coded. Solid lines represent the mean, and shaded regions indicate the SD across the four strain rates treated as repeats. Resistance increases monotonically with strain across all conditions, with higher applied voltages yielding a lower initial resistance (R_{ss}) but comparable absolute ΔR at equivalent strain.

(a) Effect of Voltage on R_0

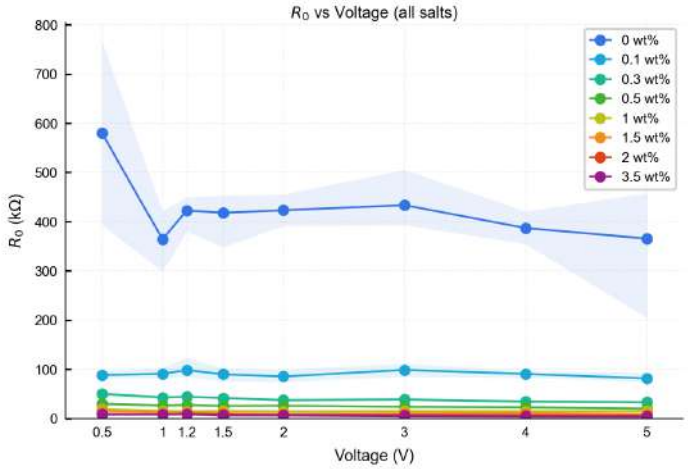

(b) Effect of Salt Concentration on R_0

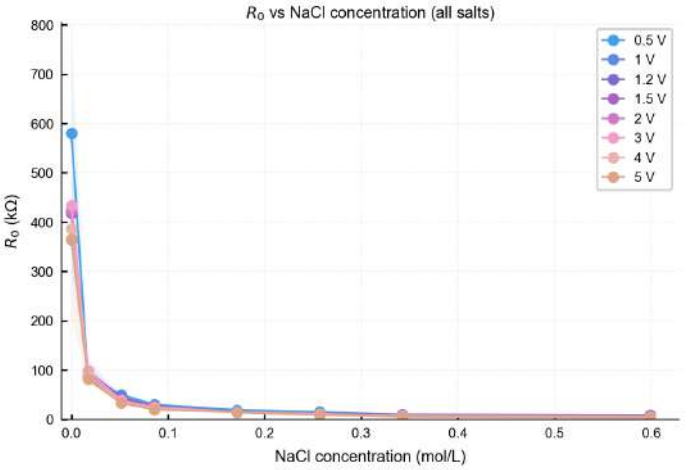

Figure S6: Summary of initial resistance (R_0) as a function of applied voltage and NaCl concentration. (a) R_0 versus applied voltage at each of the NaCl concentrations (0—3.5 wt%). (b) R_0 versus salt concentration at each of the applied voltages (0.5–5 V).

(a) R_{ss} vs NaCl Concentration (All Groups)

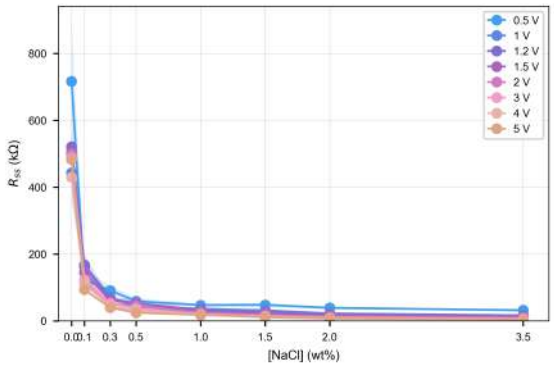

(b) R_{ss} vs NaCl Concentration (Excluding 0 wt%)

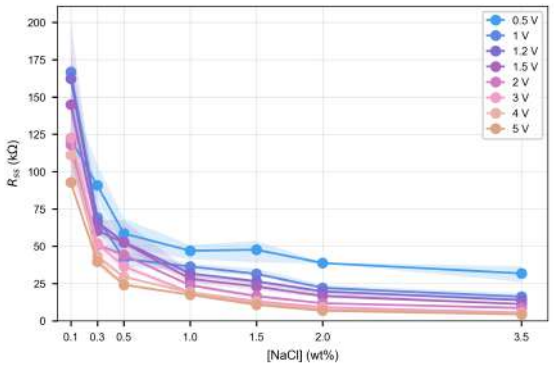

(c) R_{ss} vs Voltage (All Groups)

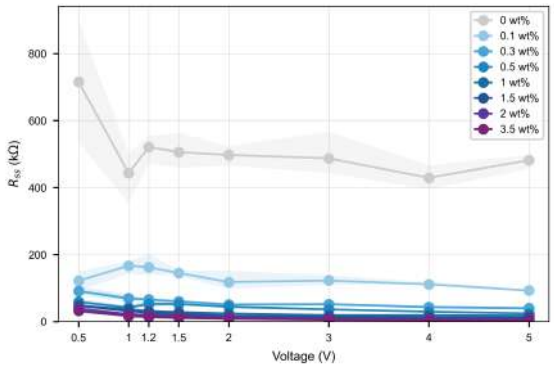

(d) R_{ss} vs Voltage (Excluding 0 wt%)

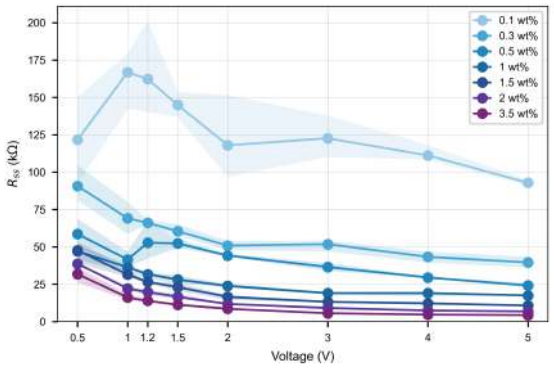

Figure S7: Summary of steady-state resistance (R_{ss}) as a function of applied voltage and NaCl concentration. (a,b) R_{ss} vs NaCl concentration at applied voltages of 0.5–5 V, with (b) excluding the 0 wt% group. (c,d) R_{ss} vs applied voltage, grouped by NaCl concentration, with (d) excluding the 0 wt% group. Solid lines: mean across samples (n=4); shaded bands: standard deviation.

(a) GF(ε), 0–800%, shared y-axis

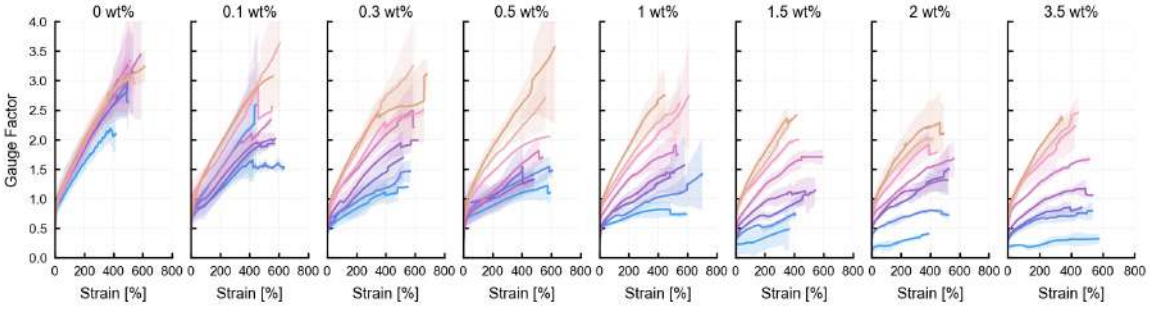

(b) GF(ε), 0–600%, zoomed y-axis

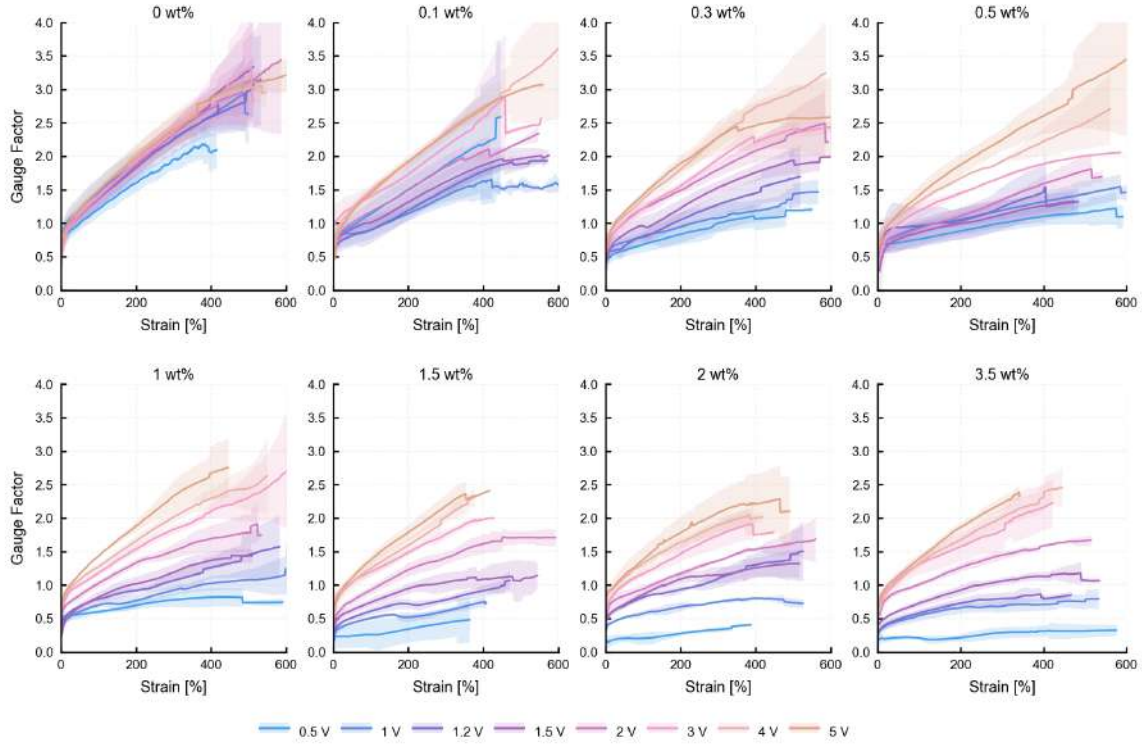

Figure S8: Gauge factor response GF(ε) across the full parameter space. (a) Overlay of all 64 GF(ε) curves on a unified axis (0—4.0), illustrating that GF increases nonlinearly with strain for all conditions and that the no-salt (0 wt%) and low-salt groups achieve the highest GF values. (b) Individual GF panels for each NaCl concentration (0—3.5 wt%). For each panel, the eight applied voltages (0.5—5 V) are color-coded. Solid lines represent the mean and shaded regions indicate the SD across the four strain rates. The GF response becomes increasingly voltage-dependent at higher salt concentrations, whereas the no-salt group shows almost voltage-insensitive GF owing to the absence of free ionic charge carriers inside gels.

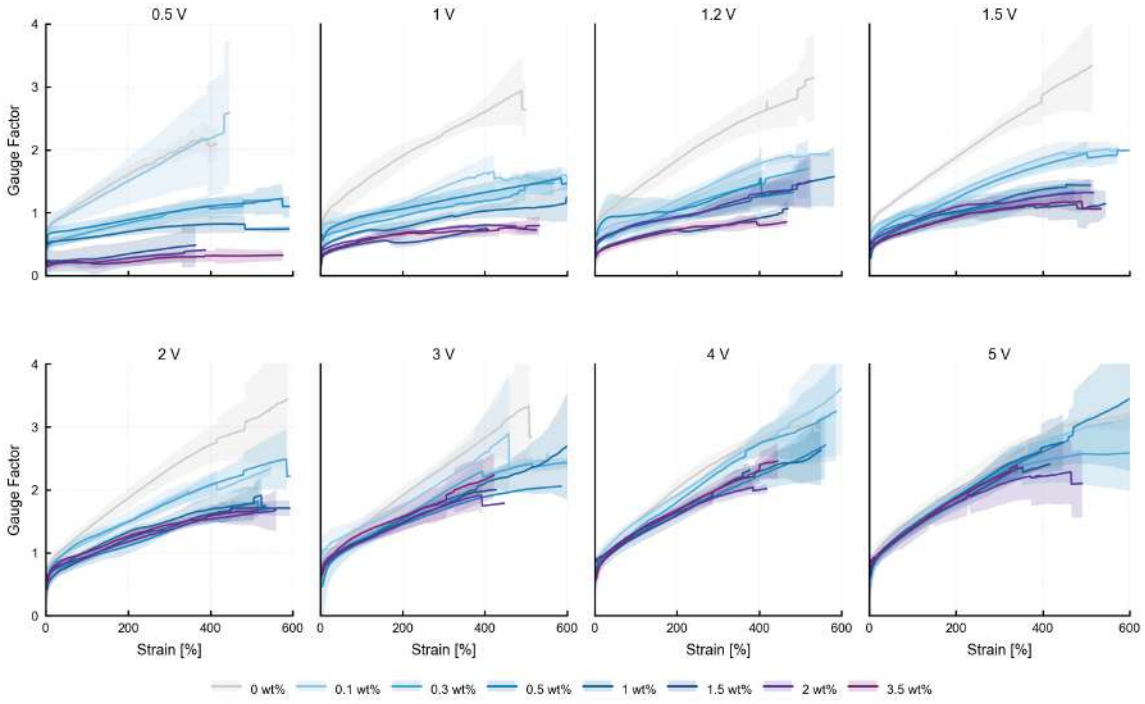

Figure S9: Gauge factor response GF(ε) reorganized by applied voltage. Each of the eight panels corresponds to a single applied voltage (0.5—5 V), with all eight NaCl concentrations (0—3.5 wt%) shown as color-coded traces. Solid lines represent the mean, and shaded regions indicate the SD across the four strain rates. Under low voltages (0.5—1.5 V), the no-salt (0 wt%) group (grey) consistently exhibits the highest GF, whereas at higher voltages ($\geq$ 2 V), low-salt formulations (0.1—0.3 wt%) approach or match the no-salt group. Higher-salt formulations ($\geq$ 1 wt%) exhibit progressively lower GF at all voltages, reflecting the trade-off between ionic conductivity and piezoresistive sensitivity introduced by NaCl.

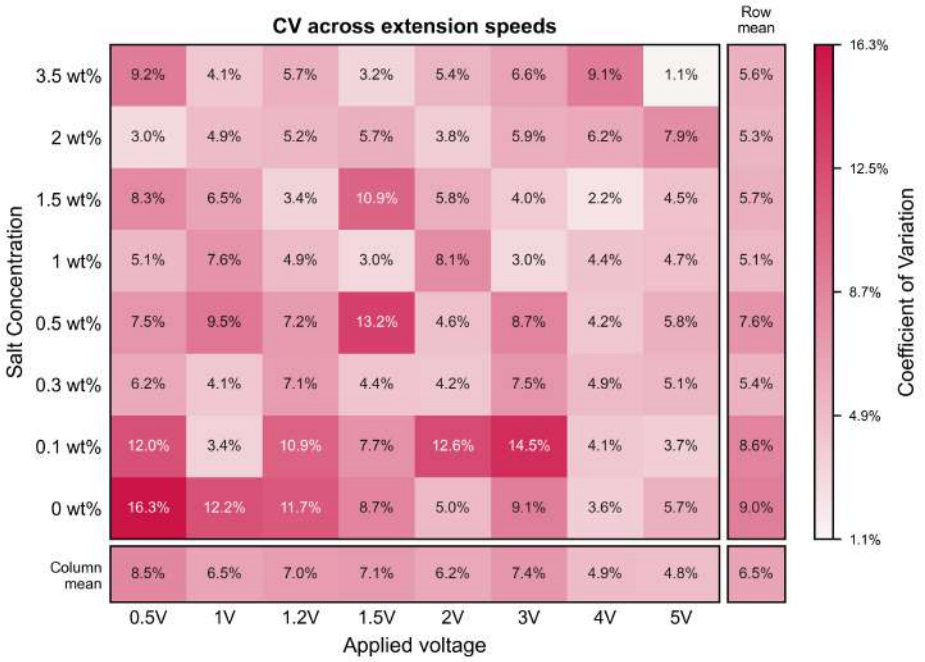

Figure S10: Full-parameter heatmap of mean coefficient of variation (CV) of resistance across strain rates. Each cell reports the mean CV (%) computed across all four strain rates at the corresponding combination of NaCl concentration (rows, 0–3.5 wt%) and applied voltage (columns, 0.5–5 V), for a total of 64 conditions (n = 64). Row and column means are shown at the right and bottom margins, respectively. Cells with CV $\geq$ 10%, which indicate notable strain-rate sensitivity, are highlighted in deeper pink. The 0 wt% group at low voltages exhibits the highest CV values (up to 16.3%), while most salt-containing formulations at voltages $\geq$ 1.2 V remain below 8%, confirming that strain-rate dependence is effectively negligible across the majority of the tested parameter space.

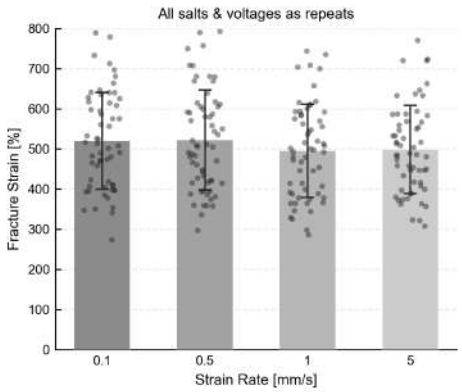

Figure S11: Fracture strain as a function of strain rate, pooled across all NaCl concentrations and applied voltages. Each bar shows the mean fracture strain (%) at one of four strain rates (0.1, 0.5, 1, and 5 mm s^{-1}), with all 64 parameter combinations (8 salt $\times$ 8 voltage) treated as repeats ($n = 64$ per group). Mean $\pm$ SD values are: 520 $\pm$ 121% at 0.1 mm s^{-1}, 522 $\pm$ 124% at 0.5 mm s^{-1}, 496 $\pm$ 116% at 1 mm s^{-1}, and 499 $\pm$ 110% at 5 mm s^{-1}. Error bars represent $\pm$ SD; individual data points are overlaid as scatter dots. Data points exceeding 800% strain are excluded as clamp slip artefacts, as this value corresponds to the maximum travel range of the linear stage and the strain conversion $\varepsilon = vt/L_0$ is no longer valid once the sample slips from the grips.

(a)

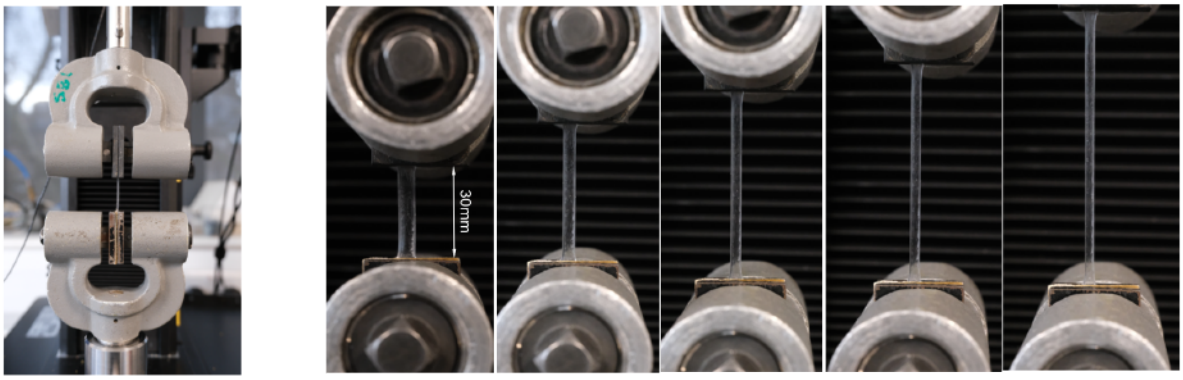

(b)

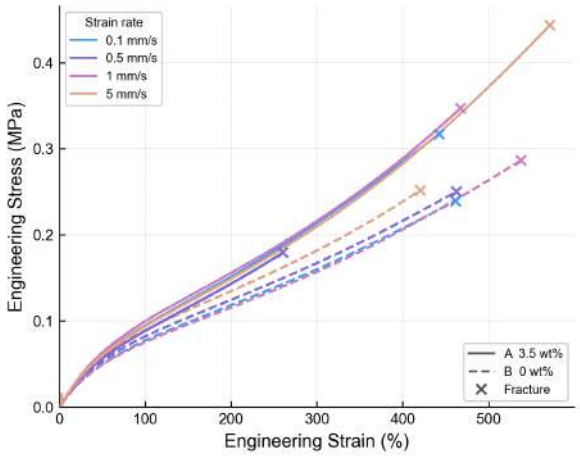

Figure S12: Mechanical characterization of IHS samples. (a) Sequential photographs of an IHS sample mounted in the film grips during uniaxial tensile testing, showing progressive elongation from the initial clamped state to near-fracture. (b) Engineering stress–strain curves at four strain rates (0.1, 0.5, 1, and 5 mms^{-1}) for representative high-salt (A 3.5 wt% NaCl) and salt-free (B 0 wt% NaCl) formulations with fracture points indicated for each data.

(a) Load–displacement Response (Increasing amplitude)

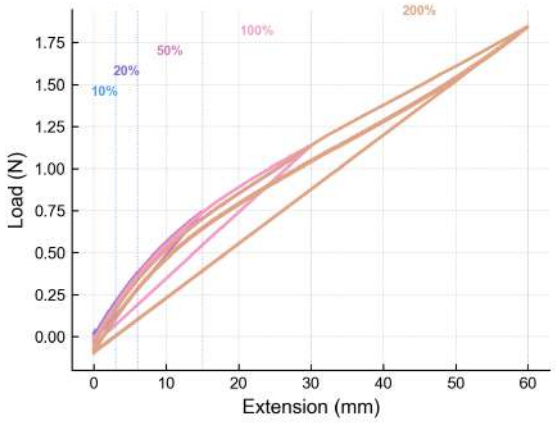

(b) Load-time Response (Increasing Amplitude)

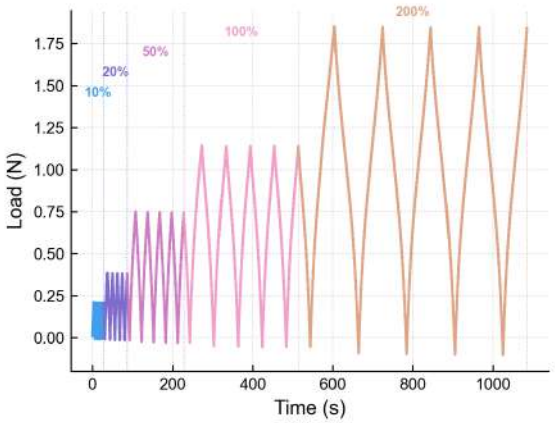

(c) Load-time Response (80% strain)

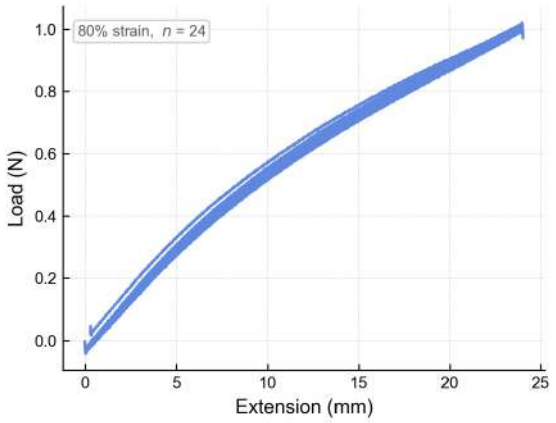

(d) Load–displacement Response (80% strain)

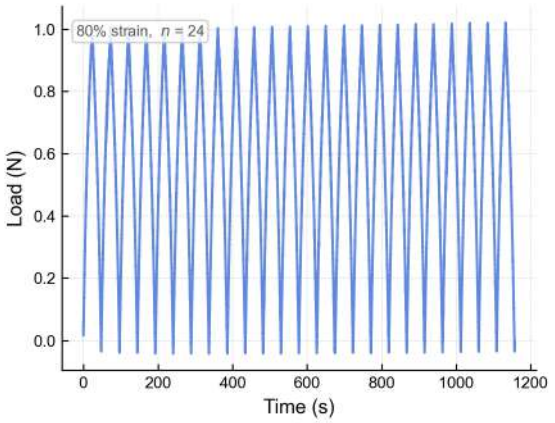

Figure S13: Cyclic mechanical loading of IHS samples. (a,b) Variable-amplitude cycling at strain levels of 10%, 20%, 50%, 100%, and 200%: (a) load–extension hysteresis loops showing reproducible behavior at each amplitude; (b) the corresponding load–time trace ($\sim$ 1100s), confirming a stable cyclic response across all amplitudes. (c,d) Constant-amplitude cycling at 80% strain for n = 24 cycles: (c) load–time trace and (d) load–extension response, demonstrating IHS mechanical repeatability without observable fatigue failure.

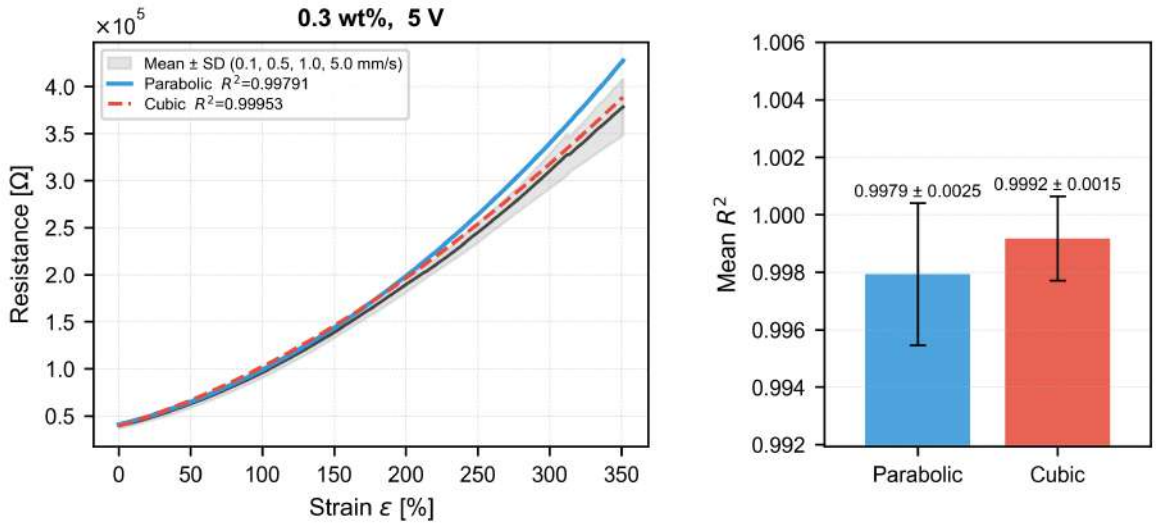

Figure S14: Comparison of resistance-strain fitting models for the IHSs. (a) A representative resistance-strain response of the hydrogel strain sensor (0.3 wt% NaCl, 5 V) fitted with both parabolic and cubic equations. (b) The goodness of fit (R^2) for the two fitting models across repeated measurements.

(a) R^2 vs Strain rates

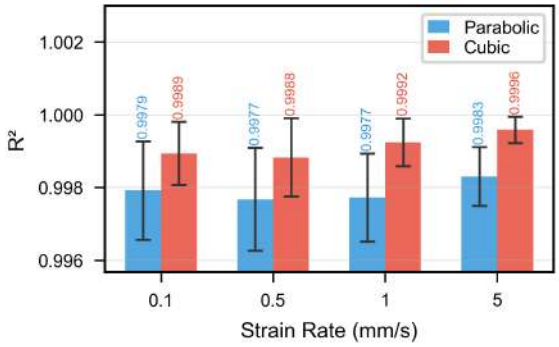

(b) R^2 vs Salt Concentrations

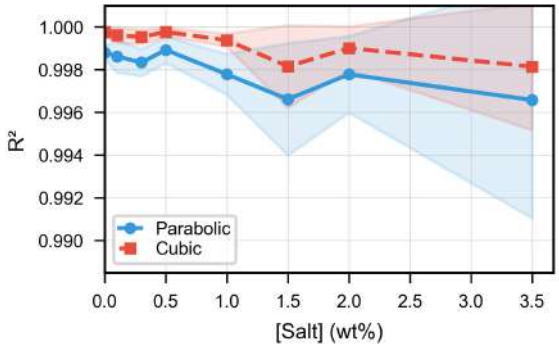

(c) R^2 vs Voltages

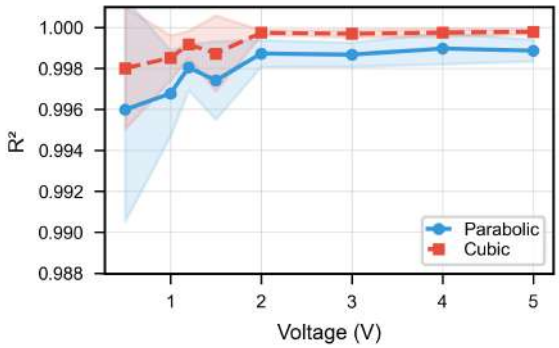

Figure S15: Goodness of fit (R^2) of the parabolic and cubic resistance–strain models fitting as a function of experimental conditions. (a) R^2 versus strain rate (0.1—5 mm s^-1) for both models (bar charts, mean ± SD). Both models achieve $R^2 > 0.997$ at all strain rates, confirming that model fit quality is insensitive to deformation rate. (b) R^2 versus NaCl concentration (0—3.5 wt%) with different voltages treated as repeats. Both Models exhibit slightly reduced R^2 at intermediate to high salt concentrations (1.5—3.5 wt%). (c) R^2 versus applied voltage (0.5—5 V) with different salt concentrations under the same applied voltage treated as repeats. For both models, elevated voltages generally exhibit better fitting.

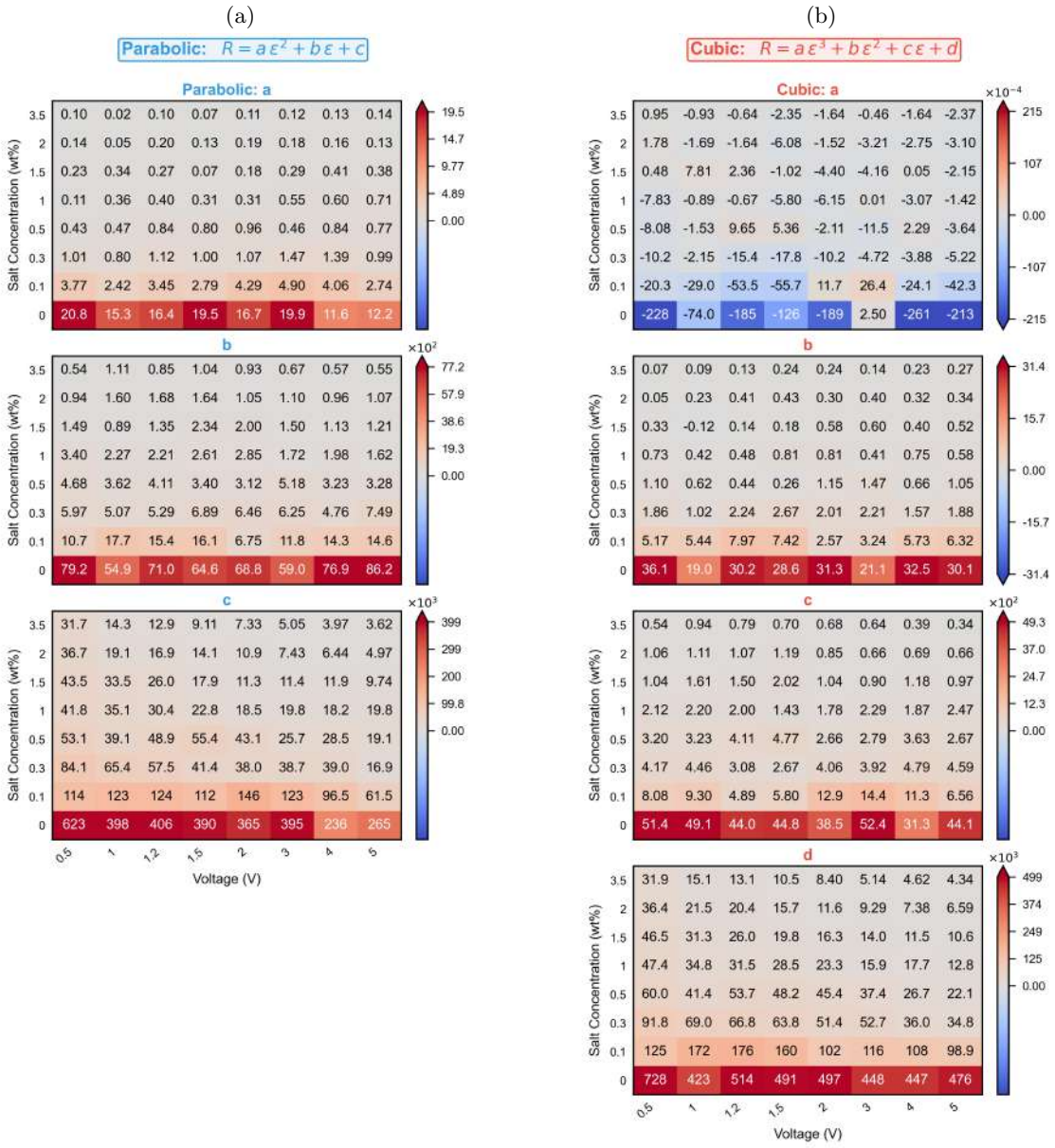

Figure S16: Systematic analysis of resistance-strain model fitting coefficients across the full parameter space. (a) Heatmaps of the three fitted coefficients (a, b, c) of the parabolic model across NaCl concentration (rows) and applied voltage (columns). Coefficient a (quadratic term, governing nonlinearity) increases with applied voltage; coefficient b (linear term) decreases above 1.2 V; and coefficient c (intercept, corresponding to R_{ss}) decreases systematically with both increasing voltage and salt concentration. (b) Heatmaps of the four fitted coefficients (a, b, c, d) of the cubic model. The leading cubic coefficient a is consistently near zero ($\times 10^{-4}$ scale), confirming its negligible contribution to the fit and supporting the selection of the parabolic model for practical deployment.

(a)

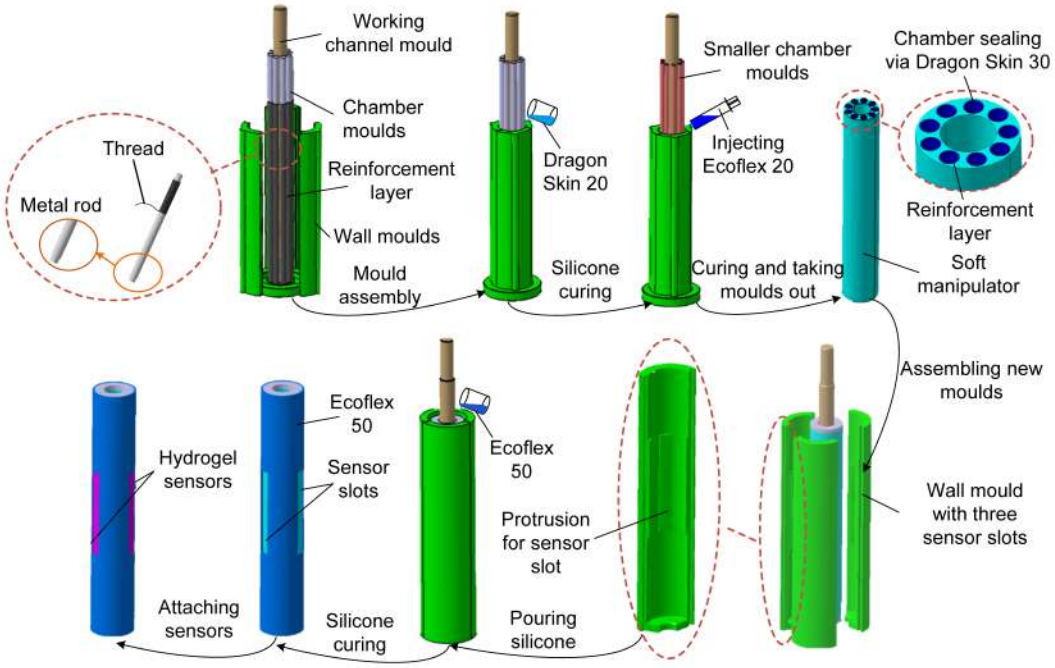

(b)

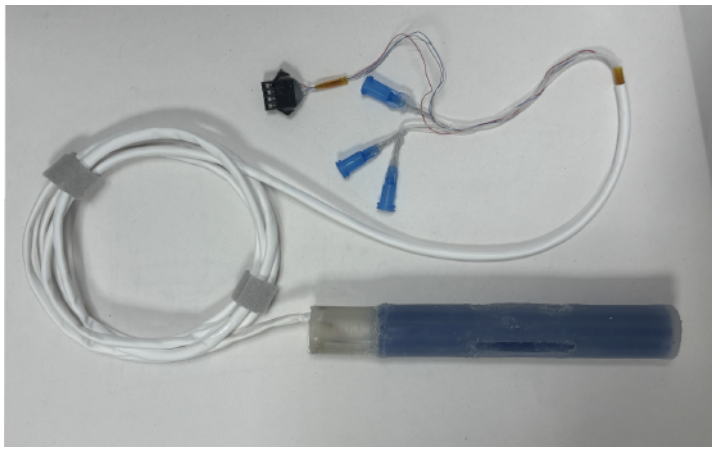

Figure S17: Soft pneumatic actuator fabrication and dimensional characterization. (a) Step-by-step schematic of the actuator fabrication protocol. A central working channel mold and chamber molds are assembled with a reinforcement layer and wall molds, then cast with Dragon Skin 20 silicone. After curing and demolding, Ecoflex 20 is injected to form the inner pneumatic chambers, sealed with Dragon Skin 30. In the second fabrication stage, new wall molds incorporating three circumferential sensor slots are assembled; Ecoflex 50 is poured to embed the sensor grooves, and IHSs are then attached and secured with adhesive. (b) Photograph of the fully assembled actuator with three IHSs attached, showing the electrical wiring and connectors.

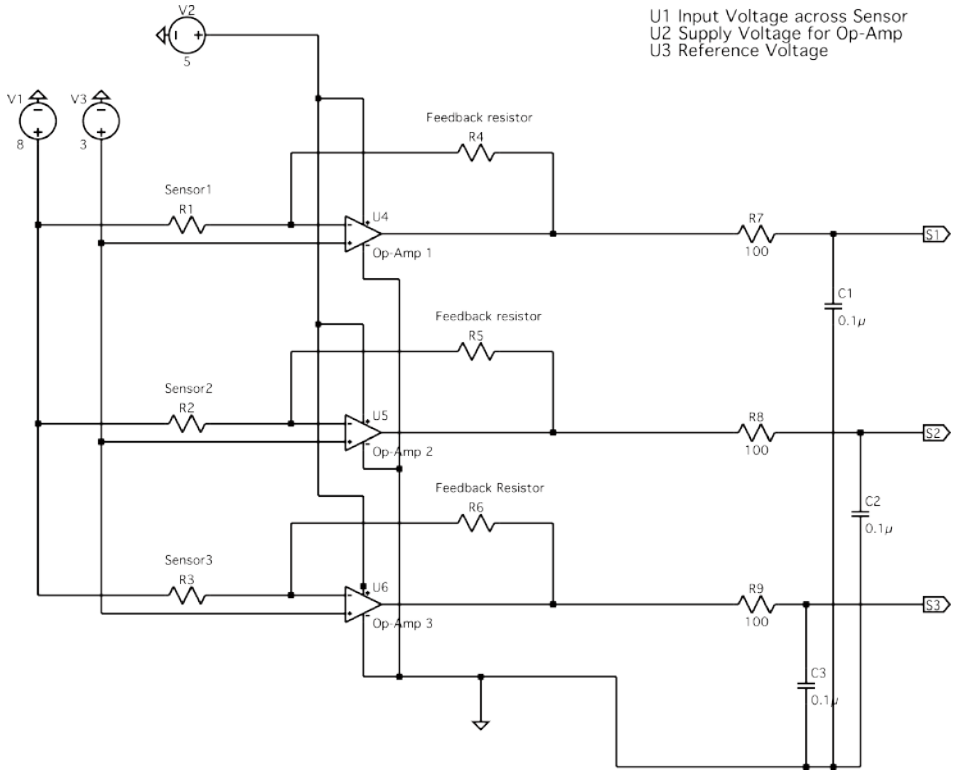

Figure S18: Schematic of the custom three-channel resistive readout circuit for IHS signal acquisition. Three IHSs (modeled as variable resistors R1–R3) are each connected in a transimpedance amplifier configuration using operational amplifiers (Op-Amp 1–3, U4–U6) with individual fixed feedback resistors (R4–R6). Three voltage sources are used: V1 (8 V, input bias voltage applied across the sensors), V2 (5 V, op-amp supply voltage), and V3 (3 V, reference voltage defining the measurement baseline). The output of each amplifier passes through a series resistor (R7–R9, 100) and a first-order RC low-pass filter (C1–C3, 0.1 μF) to suppress high-frequency noise before the voltage signals (S1–S3) are digitized. The voltage difference between the Vin and Vref produce a 5 V differential across each IHS. Each channel operates independently, enabling simultaneous acquisition of strain signals from all three sensors.

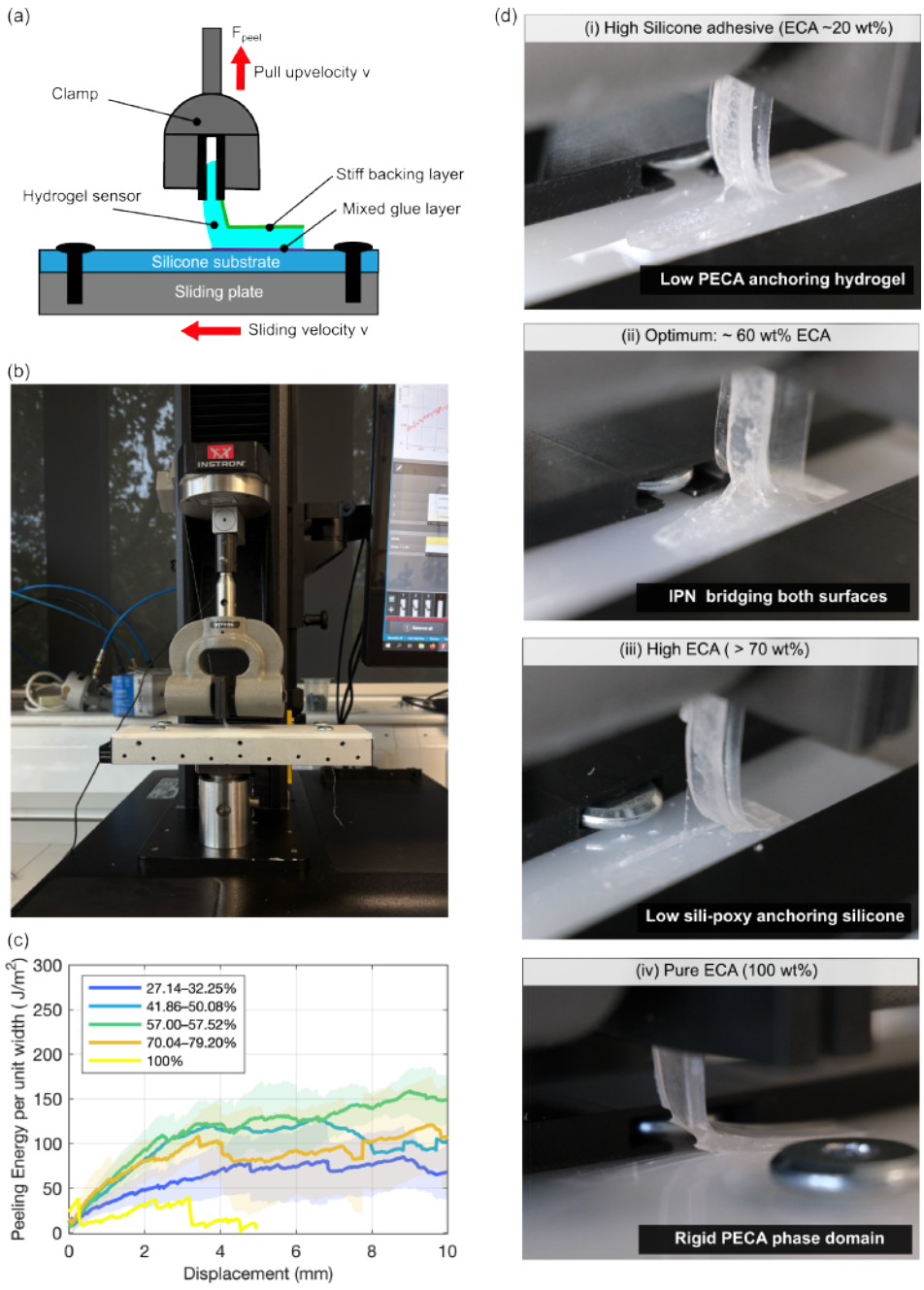

Figure S19: Peel test configuration and composition-dependent interfacial failure behavior. (a) Schematic of the peel test used to evaluate the adhesion of hydrogel-based sensor assemblies on silicone substrates. (b) Photograph of the corresponding experimental setup on an Instron testing machine. (c) Peeling energy per unit width as a function of displacement for different ECA composition ranges; shaded areas represent the variation within each group. (d) Representative peeling morphologies for different ECA contents, showing distinct failure modes: (i) low PECA anchoring to the hydrogel at high silicone adhesive content (20 wt% ECA), (ii) effective IPN bridging between both surfaces at the optimum composition (60 wt% ECA), (iii) reduced sili-poxy anchoring to the silicone substrate at high ECA content (>70 wt%), and (iv) rigid PECA phase domains in pure ECA (100 wt%).

(a) Humidity Test Setup

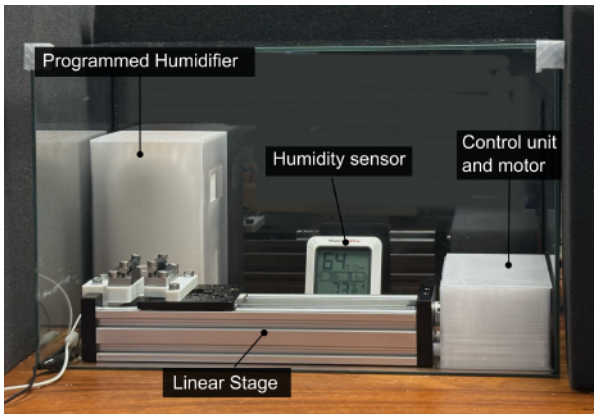

(b) Sensor-level Cyclic Test

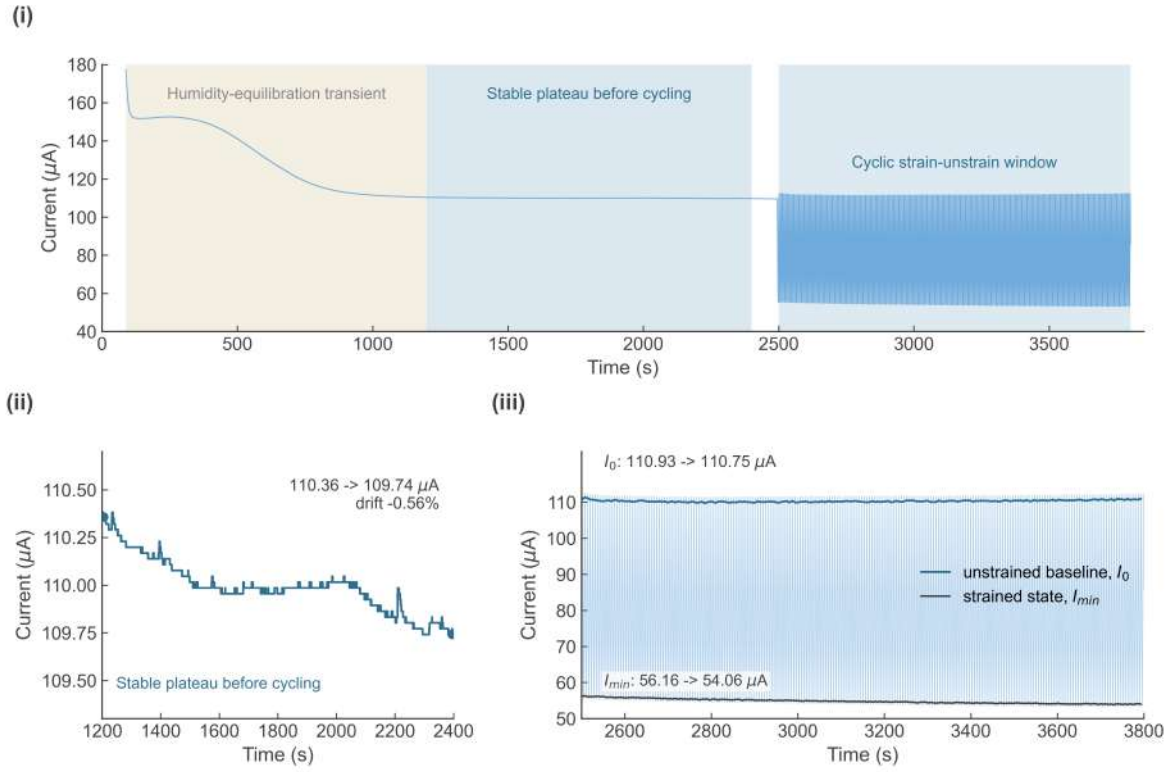

Figure S20: Humidity-controlled characterization of IHS electrical stability. (a) Photograph of the sealed test enclosure containing a programmed humidifier, a humidity sensor, a motor-driven linear stage for mechanical actuation, and a control unit. The enclosure maintains a target relative humidity of 70% RH throughout testing. (b) Sensor-level cyclic test of the IHS (0.3 wt% NaCl, 5 V) inside the humidity-controlled chamber. (i) Full current–time trace showing the initial humidity-equilibration transient, the stable plateau before cyclic loading, and the subsequent cyclic strain–unstrain window. (ii) Enlarged view of the stable plateau after humidity equilibration. The current decreased from 110.36 to 109.74 μA, corresponding to a baseline drift of -0.56%. (iii) Current response during cyclic strain–unstrain loading. The unstrained baseline current decreased from 110.93 to 110.75 μA, corresponding to a drift of -0.16%.

(a) Complete Integrated Experimental Platform

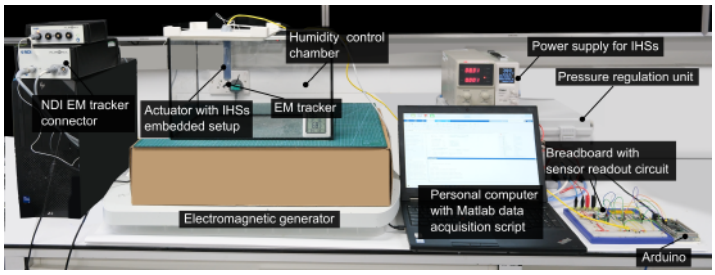

(b) Device-level Cyclic Test

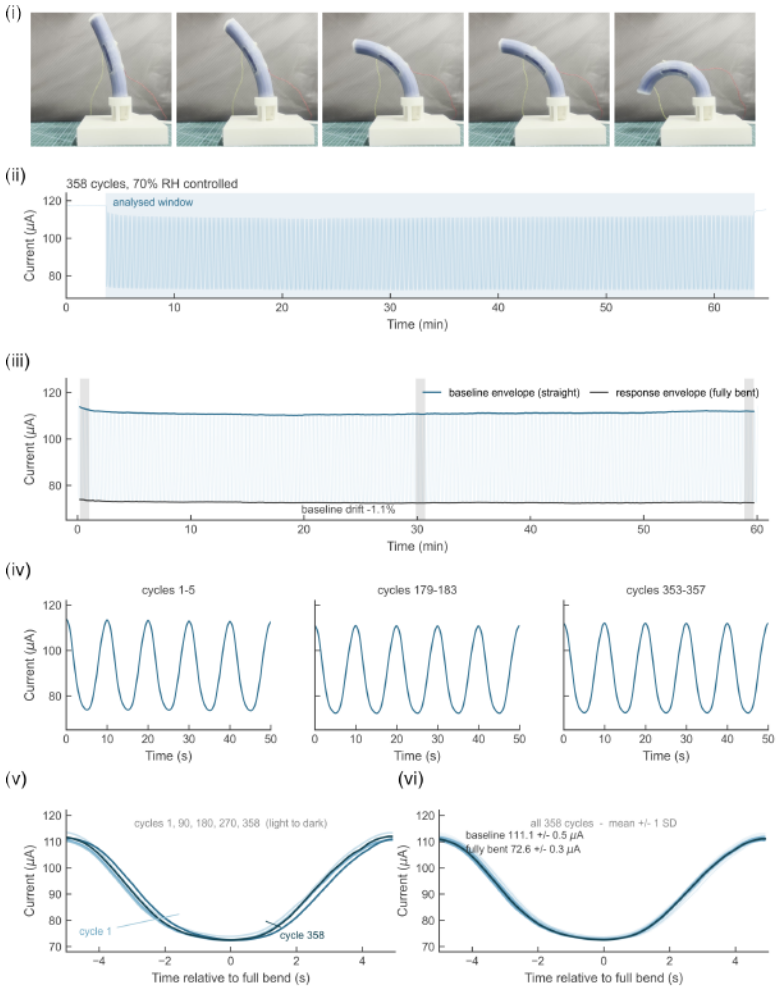

Figure S21: Experimental platform and cyclic stability of ionic hydrogel sensors integrated into a soft robotic endoscope tip. (a) Photograph of the complete integrated experimental platform for embedded IHS characterization. (b) Device-level cyclic test. (i) Sequential photographs of the IHS-integrated soft steering tip during large pneumatic bending. (ii) Current trace of the integrated IHS mounted on the soft endoscopic steering tip during the 70% RH controlled cyclic test. (iii) Enlarged view of the 358-cycle strain–unstrain test with the extracted unstrained baseline envelope and fully bent response envelope. The baseline current changed from 113.15 to 111.92 μA, corresponding to a drift of -1.09%, while the fully bent-state current changed from 73.70 to 72.51 μA, a drift of -1.61%. (iv) Representative current waveforms from early, middle, and late stages of the test, showing cycles 1–5, 179–183, and 353–357, respectively. (v) Phase-aligned current responses from selected cycles across the test. (vi) Overlay of all 358 phase-aligned cycles with the mean $\pm$ 1 SD response, showing stable waveform consistency throughout repeated strain–unstrain cycling.

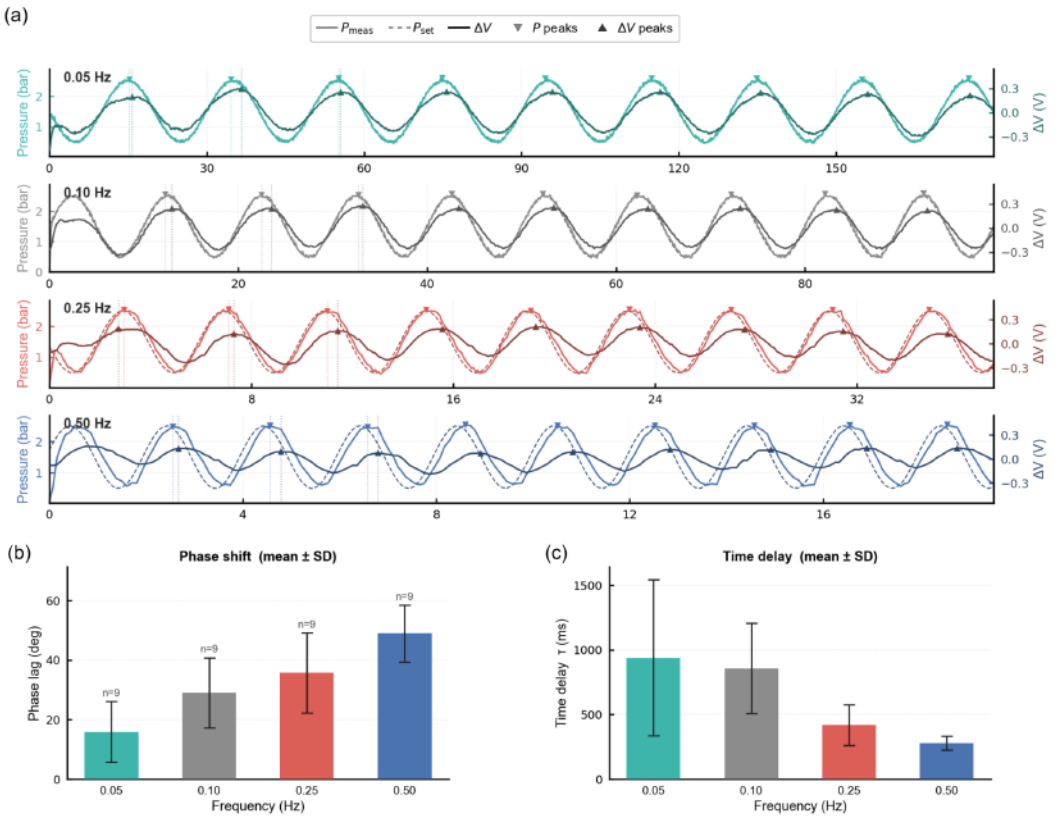

Figure S22: Frequency-dependent response of the soft actuator under sinusoidal pressure input. (a) Representative time-series recordings at four input frequencies (0.05, 0.10, 0.25, and 0.50 Hz). Each panel shows the set pressure (P_{set}, dashed line), measured pressure (P_{meas}, solid line), and the corresponding sensor reading (ΔV, dashed line) on dual y-axes. Detected peaks of P_{meas} and ΔV are marked by downward and upward triangles, respectively. The phase delay between matched peak pairs is indicated by vertical dashed lines. Boundary peaks within $0.4T_0$ of the signal edges were excluded from analysis. (b) Phase shift (mean ± SD) between the pressure and voltage signals increases monotonically with input frequency, from $15.9 \pm 10.2°$ at 0.05 Hz to $48.9 \pm 9.5°$ at 0.50 Hz ($n = 9$ cycles per frequency). (c) Absolute time delay τ (mean ± SD), derived from the phase shift as $\tau = \phi/(360° \times f)$, decreases with frequency, from 940 ± 603 ms at 0.05 Hz to 278 ± 54 ms at 0.50 Hz, indicating that the absolute mechanical lag becomes smaller at higher actuation rates.

Nominal freq (Hz)	**Actual freq (Hz)**	***n* (cycles)**	**Phase shift (deg)**	**Time delay (ms)**	**ΔV amplitude (V)**	**3D motion (mm)**
0.05	0.047	9	15.9 ± 10.2	940 ± 603	0.255 ± 0.006	47.4
0.10	0.094	9	29.0 ± 11.8	857 ± 349	0.251 ± 0.009	45.8
0.25	0.236	9	35.7 ± 13.4	420 ± 158	0.178 ± 0.009	41.0
0.50	0.488	9	48.9 ± 9.5	278 ± 54	0.122 ± 0.007	19.7

Table S2: Static summary of frequency-dependent sensor and actuator responses. Phase shift and ΔV amplitude are reported as mean ± SD ($n = 9$ cycles per frequency). Time delay τ is derived from the phase shift as $\tau = \varphi \,/\, (360° \times f)$.

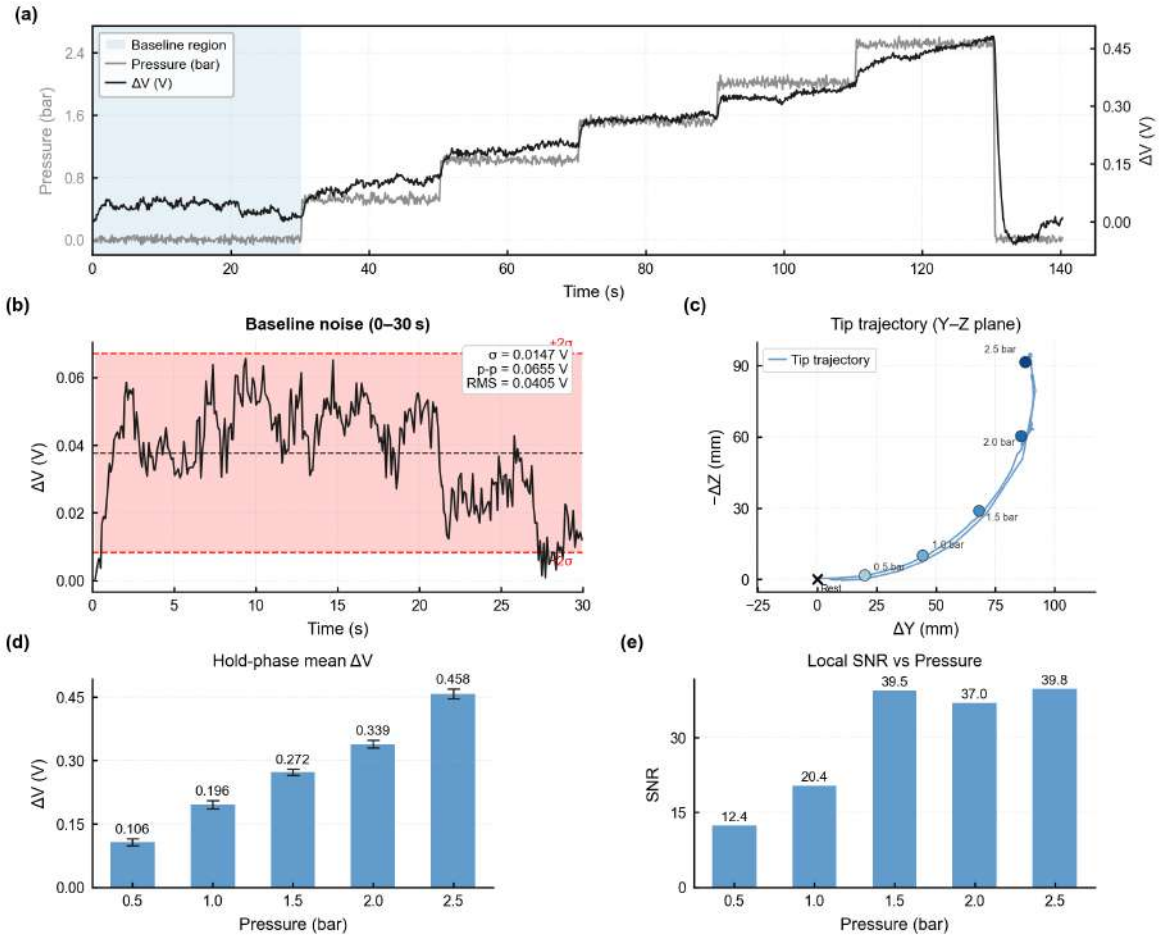

Figure S23: Stepwise pressurization characterization of the embedded IHS. (a) Applied pressure (gray, left axis) and IHS output (black, right axis) as a function of time during stepwise pressurization (0.5–2.5 bar, 20 s per step). The blue-shaded region (0–30 s) indicates the zero-pressure baseline window. (b) Zoom in view of the zero-pressure baseline window, illustrating the intrinsic noise floor of the sensing circuit. The dashed black line denotes the mean (0.040 V), and the dashed red lines mark the $\pm\ 2\sigma$ boundary. (c) Tip trajectory of the soft actuator in the Y-Z bending plane, recorded by an electromagnetic (EM) tracker. Circles mark the hold-phase centroids at each pressure level. At low pressures ($\leq$1.0 bar), the displacement is predominantly lateral (ΔY), whereas at higher pressures the actuator develops a pronounced bending arc. (d) Hold-phase ΔV at each pressure level (mean $\pm$ SD). The values increase monotonically from 0.106 ± 0.009 V at 0.5 bar to 0.458 ± 0.012 V at 2.5 bar. The hold-phase standard deviations remain below 0.012 V (2.5-8.0% of the corresponding mean ΔV), comparable to the baseline noise floor, confirming that no additional drift is introduced with increasing load. (e) Local signal-to-noise ratio (SNR=Mean(ΔV)/SD(ΔV), computed within each hold window) as a function of pressure.

Pressure (bar)	0.5	1.0	1.5	2.0	2.5
ΔV (V)	0.106 ± 0.009	0.196 ± 0.010	0.272 ± 0.007	0.339 ± 0.009	0.458 ± 0.012

Table S3: Static summary of hold-phase ΔV at each pressure level during the hold stage. Values are mean $\pm$ SD.

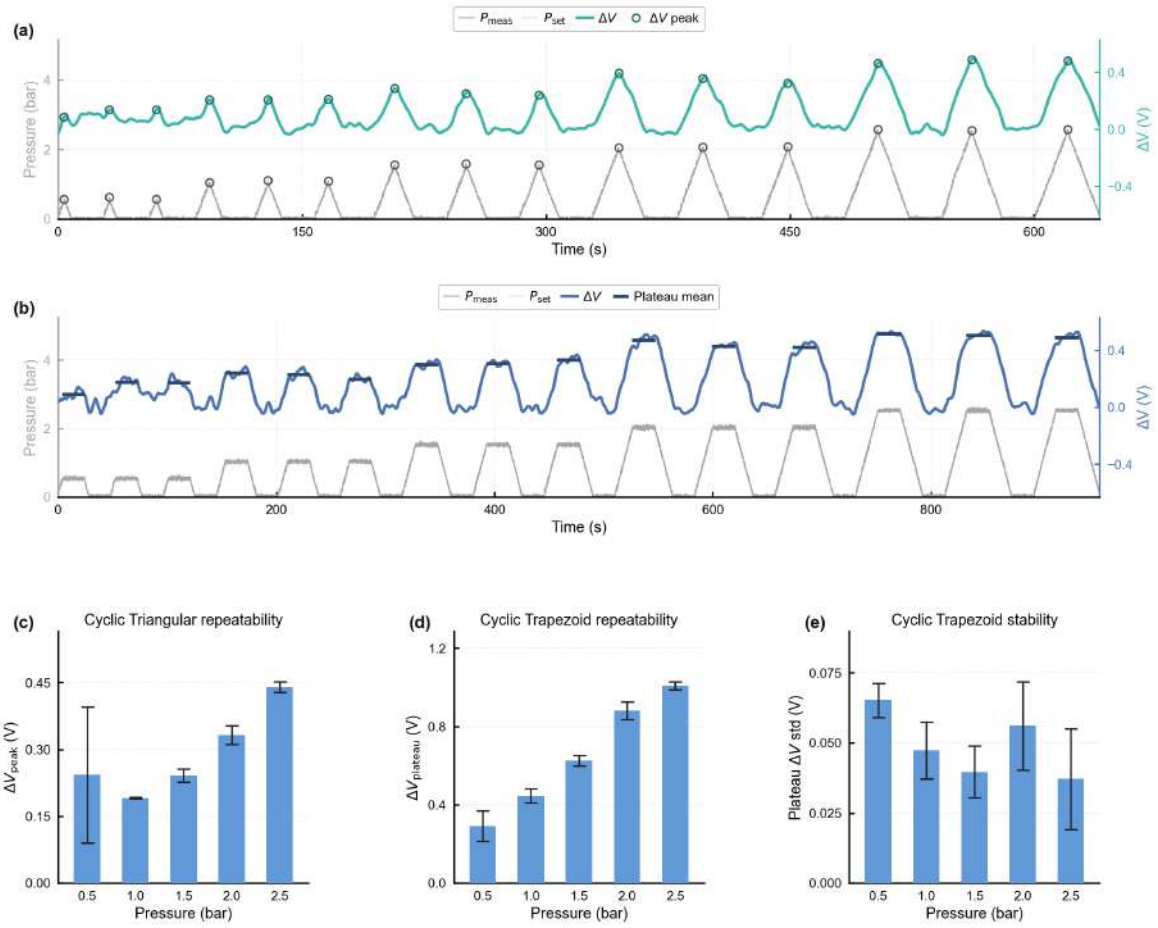

Figure S24: Characterization of the sensor response under cyclic triangular and trapezoidal pressure waveforms. (a) Representative time series of a triangular pressure cycle, showing the measured pressure (P_{meas}, left axis) and the baseline-corrected voltage response (ΔV, right axis). Downward triangles indicate pressure peaks, and upward triangles denote the corresponding ΔV peaks. Arrows indicate the phase delay between pressure onset and the peak ΔV response. (b) Representative time series of a trapezoidal pressure cycle. Horizontal segments indicate the mean ΔV during each pressure hold phase. (c) Cycle-to-cycle reproducibility of peak ΔV for the triangular waveform (n = 3 repetitions per pressure level; bars: mean; error bars: ± SD; CV: coefficient of variation). (d) Cycle-to-cycle reproducibility of plateau ΔV for the trapezoidal waveform (n = 3; bars: mean ± SD). (e) Hold-phase stability, expressed as the within-cycle standard deviation of ΔV during each pressure plateau (bars: mean per-cycle SD ± SD across cycles).

	Triangular		Trapezoidal		Hold phase
P (bar)	ΔV_{peak} (V)	CV (%)	$\Delta V_{\text{plateau}}$ (V)	CV (%)	ΔV (V)
0.5	0.243 ± 0.153	62.8	0.291 ± 0.078	26.7	0.065 ± 0.006
1.0	0.191 ± 0.002	1.2	0.446 ± 0.037	8.3	0.047 ± 0.010
1.5	0.241 ± 0.014	5.9	0.626 ± 0.026	4.2	0.040 ± 0.009
2.0	0.332 ± 0.021	6.3	0.881 ± 0.045	5.1	0.056 ± 0.016
2.5	0.440 ± 0.012	2.6	1.008 ± 0.020	2.0	0.037 ± 0.018

Table S4: Summary of sensor response metrics under triangular and trapezoidal pressure waveforms. Data shown as mean ± SD ($n = 3$).

Parameter	Symbol	Value
Soft actuator geometry		
Sensor radius (mm)	r	8.5
Undeformed actuator length (mm)	L_0	115
Sensor angular positions		
Sensor 1 angle (deg)	θ_1	90 (ideal) / 90.4 (measured)
Sensor 2 angle (deg)	θ_2	210 (ideal) / 209.0 (measured)
Sensor 3 angle (deg)	θ_3	330 (ideal) / 326.8 (measured)
Sensor calibration result for Figure 7d $R_i(\varepsilon)$ in Ω, ε in %		
Sensor 1	R_1	$4.70\,\varepsilon^2 + 426.8\,\varepsilon + 69{,}041$ $(R^2 = 0.990)$
Sensor 2	R_2	$0.45\,\varepsilon^2 + 405.1\,\varepsilon + 65{,}889$ $(R^2 = 0.972)$
Sensor 3	R_3	$6.17\,\varepsilon^2 + 262.7\,\varepsilon + 55{,}303$ $(R^2 = 0.991)$
Signal processing and registration		
Delay compensation (s)	τ	0.94

Table S5: Parameters used for the final 3D shape reconstruction.

Condition	Mean (mm)	STD (mm)	RMSE (mm)	Relative error (%)
Without delay compensation	12.56	6.87	14.31	10.08 ± 5.51
With delay compensation (0.94 s)	7.37	4.76	8.77	5.92 ± 3.82

Table S6: 3D tip reconstruction error with and without time-delay compensation. Relative error is normalized by the actuator arc length.

Panel	Case / metric	Actuation pressure (bar)	Terminal moment (N·m)	S1 / κ_x	S2 / κ_y	S3 / $\lvert\kappa\rvert$ or orientation
A. Simulated axial strain response						
No bending	No torsion	[0, 0, 0]	[0, 0, 0]	0.0000	0.0000	0.0000
	With torsion	[0, 0, 0]	[0, 0, 0.0085]	0.0007937	0.0007937	0.0007937
	$\Delta\varepsilon$	–	–	+0.0007937	+0.0007937	+0.0007937
	$\Delta\varepsilon/\varepsilon_{\max,\text{baseline}}$	–	–	N.D.	N.D.	N.D.
Large bending	No torsion	[2.5, 0, 0]	[0, 0, 0]	0.2990	0.2039	0.0253
	With torsion	[2.5, 0, 0]	[-0.00651, -0.00546, 0.00028]	0.3096	0.1877	0.0319
	$\Delta\varepsilon$	–	–	+0.0106	-0.0162	+0.0066
	$\Delta\varepsilon/\varepsilon_{\max,\text{baseline}}$	–	–	+3.5%	-5.4%	+2.2%
B. Curvature reconstruction from the large-bending strain values						
Condition		κ_x (m^{-1})	κ_y (m^{-1})	$\lvert\kappa\rvert$ (m^{-1})	**Orientation (°)**	**Change**
Large bending	No torsion	14.46	12.14	18.88	40.00	–
	With torsion	15.67	10.59	18.91	34.04	$\Delta\lvert\kappa\rvert = +0.16\%$, $\Delta\phi = -5.96°$

Table S7: Numerical torsion-sensitivity analysis and curvature reconstruction results.

(a) No pneumatic actuation, no torsion.

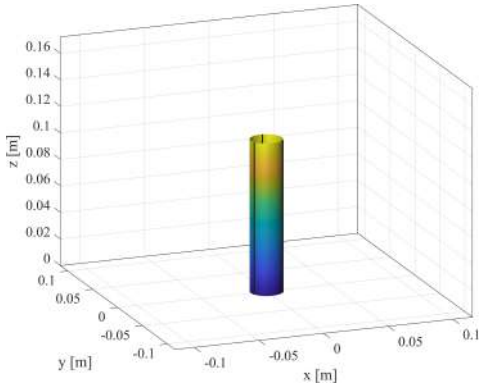

(b) No pneumatic actuation, with terminal torsion.

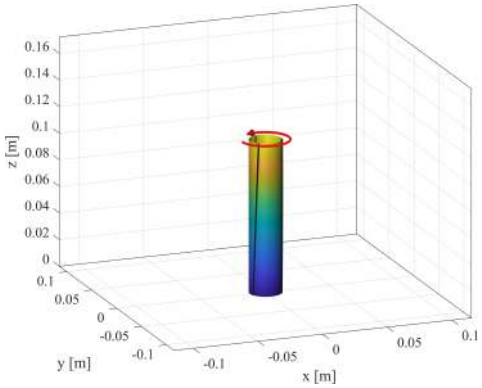

(c) Large pneumatic bending, no torsion.

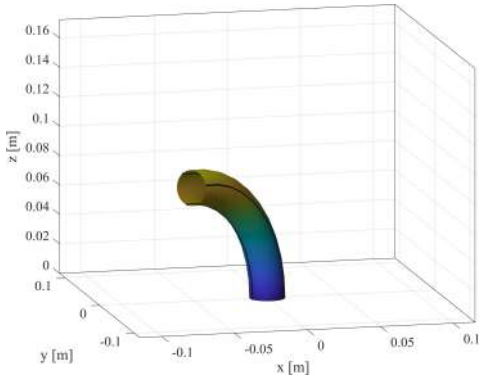

(d) Large pneumatic bending, with terminal torsion.

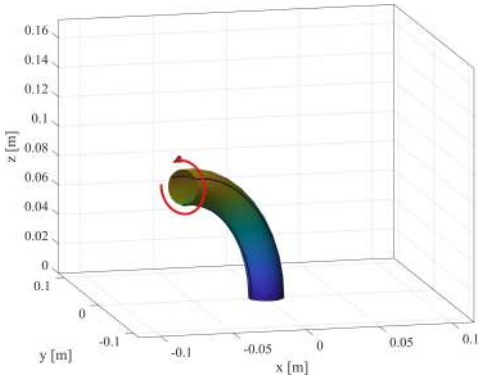

Figure S25: Numerical torsion-sensitivity analysis using the static forward model from [1]. The upper row compares the no-bending case without and with an applied terminal torsional moment. The lower row compares the representative large-bending condition without and with the applied terminal torsional moment, allowing the torsion-induced perturbation in actuator shape and sensor-path strain to be evaluated.

S2 Supplemental notes

Note S1: Cross-instrument validation of piezoresistive response measurements

To cross-validate the electrical characterization data, a subset of IHS samples was characterized using the Keithley 4200-SCS parameter analyzer (PA) alongside the AUTOLAB potentiostat. Both instruments performed identical measurement protocols under the same applied voltages and strain conditions. The comparison revealed a consistent transition in the PA-measured current at a threshold of approximately 1.33×10^{-4}A (133 μA). Below this threshold, the current responses recorded by the two instruments were in close agreement across all tested NaCl concentrations and applied voltages. Above this threshold, however, the PA-measured current appeared suppressed relative to the AUTOLAB reference, with the two traces diverging progressively. Critically, this transition current was independent of sample composition and applied voltage, confirming that it originates from the PA instrument itself rather than from any intrinsic property of the IHS samples. This behavior might stand for the current compliance limit of the PA — the maximum current the instrument can reliably source and measure before internal protection circuitry clamps the output.

These results show two important implications. First, they validate the reliability of the AUTOLAB-derived characterization data. In the sub-threshold regime, the results are highly reproducible across both measurement platforms, confirming that the electromechanical response data reported in the main text are instrument-independent. Second, they highlight a practical consideration in the design of readout instrumentation for ionic hydrogel sensors. Given that hydrogels typically exhibit resistance in the range of 10^4–10^6 Ω, the resulting operating current at bias voltages of 0.5–5 V spans approximately 1–500 μA. Any measurement instrument or custom sensing circuit intended for use with such sensors must therefore be capable of reliably resolving signals across this dynamic range, particularly at the low end (sub-μA), to avoid compliance-induced clipping at high-conductance conditions and signal-to-noise limitations at low-conductance conditions.

Note S2: Model fitting of resistance and strain curves

To enable continuous and quantitative mapping between the electrical output and strain deformation of the IHS, two mathematical models, parabolic and cubic functions, were adopted to fit the nonlinear resistance–strain relationship, $R(\varepsilon)$, where ε denotes the engineering strain (%). For each experimental condition (NaCl concentration, applied voltage, and strain rate), the resistance–strain relationship $R(\varepsilon)$ was fitted independently using MATLAB's nonlinear least-squares routine (`fit`, Curve Fitting Toolbox).

$$R(\varepsilon) = \begin{cases} a_1\varepsilon^2 + b_1\varepsilon + c_1 & \text{(Parabolic)} \\ a_2\varepsilon^3 + b_2\varepsilon^2 + c_2\varepsilon + d_2 & \text{(Cubic)} \end{cases} \tag{S1}$$

The quadratic term in the parabolic model has a geometric origin: for a homogeneous elastic conductor of length L_0 and cross-sectional area A_0, uniaxial strain ε gives $R \propto L/A \propto (1+\varepsilon)^2 \approx 1 + 2\varepsilon + \varepsilon^2$, contributing an intrinsic ε^2 curvature independent of ionic content [2, 3]. To assess whether the parabolic model fully captures the resistance-strain relationship, a cubic model was also fitted to the same dataset. Goodness of fit R^2 was quantified by the coefficient of determination:

$$R^2 = 1 - \frac{\sum_i (R_i - \hat{R}_i)^2}{\sum_i (R_i - \bar{R})^2} \tag{S2}$$

where R_i are the measured resistance, $\hat{R}_i$ the model predictions resistance, and $\bar{R}$ the mean measured resistance.

Taking the optimized IHS (0.3 wt% NaCl, 5 V) as a representative example (Figure S14a, Supplemental Information), the mean resistance–strain curve is plotted together with the two fitted models, with the shaded band spanning one standard deviation about the mean across the four tested strain rates. The goodness of fit, quantified by R^2 (Equation S2), was 0.998 for the parabolic model and

0.9995 for the cubic model, with the corresponding fitted resistance–strain relationships given as:

$$R(\varepsilon) = \begin{cases} 0.627\varepsilon^2 + 201.8\varepsilon + 16393 & \text{(Parabolic)} \\ -3.29 \times 10^{-4}\varepsilon^3 + 0.769\varepsilon^2 + 185.6\varepsilon + 16781 & \text{(Cubic)} \end{cases} \tag{S3}$$

The full parameter space comprised 8 NaCl concentrations × 8 applied voltages × 4 strain rates, yielding 256 fitted curves per model. The goodness of fit (R^2) of both models as a function of experimental condition is summarized in Figure S15 to assess the effect of strain rate, salt concentration, and applied voltage. No systematic dependence on strain rate was observed (Figure S15a). R^2 shows a modest decreasing trend with increasing salt concentration (Figure S15b), and greater scatter is present at applied voltages below 2 V; at $V \geq 2$ V the fits are consistently tight across all conditions (Figure S15c).

The systematic analysis of model fitting across the full parameter space is presented in Figure S16. Both the parabolic and cubic models achieved $R^2 > 0.98$ across all conditions, with the cubic model yielding marginally higher R^2 in general (Figure S16). The variation of the leading coefficient a of parabolic fitting further reveals a concentration-dependent transition in conduction behavior (Figure S16a). For low salt concentrations ($c \leq 0.3wt\%$), a remains relatively large and shows no clear dependence on applied voltage, with a slight decreasing trend particularly evident in the salt-free case, indicating a strongly nonlinear response. In contrast, at higher salt concentrations ($c \geq 0.5wt\%$), a decreases significantly (e.g., $\sim$ 0.6 at 1 wt%, $\sim$ 0.3 at 1.5 wt%, and approaching zero at 3.5 wt%), reflecting a transition from a nonlinear toward a quasi-linear piezoresistive response $R(\varepsilon)$. Since purely geometric deformation of a homogeneous conductor already introduces an intrinsic quadratic term via $R \propto (1+\varepsilon)^2$, the much larger a values observed at low salt indicate an additional strain-dependent reduction in effective conductivity beyond geometry alone. In this regime, ionic transport is possibly more strongly coupled to deformation-induced rearrangement of the polymer network, so stretching not only changes the sample dimensions but also increasingly disrupts ion-conduction pathways. With increasing salt concentration, the larger population of mobile ions makes conduction progressively less sensitive to such microstructural changes, and the fitted a approaches zero. In the limit $a \to 0$, the parabolic model approaches a linear relationship $R(\varepsilon) \approx b\varepsilon + c$, consistent with Ohmic behavior in which resistance scales directly with strain.

To assess whether the parabolic model fully captures the resistance-strain relationship, a cubic model was also fitted to the same dataset and the fitted coefficients a, b, c, and d are summarized in Figure S16b. The leading cubic coefficient a remains consistently near zero ($\sim 10^{-4}$) across all conditions, confirming that the third-order contribution is almost negligible. Based on the results above, the parabolic model was adopted for all subsequent analyses, as it provides equivalent predictive accuracy with fewer free parameters and admits a physical interpretation of its coefficients.

Note S3: Integrated electronics

The ionic hydrogel sensors were interfaced with a custom-designed, multi-channel resistive readout circuit based on operational amplifier transimpedance amplification. Each sensing element was biased at a constant input voltage and converted into a voltage output through a fixed feedback resistor, ensuring consistent gain across channels. A reference voltage was applied to define the operating point of the measurement. Output signals were passed through first-order RC low-pass filters prior to acquisition, providing noise suppression while introducing a finite electronic response time. In the subsequent data-processing stage, smoothing was applied to the voltage signals to suppress high-frequency acquisition noise while preserving the dynamic response and phase characteristics used for reconstruction.

Each IHS was modeled as a variable resistance R and interfaced with an op-amp-based resistive readout circuit with a fixed feedback resistor R_f and a reference voltage V_{ref}. Assuming linear operation, the output voltage is given by

$$V_{\text{out}} = V_{\text{ref}} - \frac{R_f}{R}\left(V_{\text{in}} - V_{\text{ref}}\right), \tag{S4}$$

To extract strain from the circuit output, a two-step signal conversion pipeline was implemented. First, the measured output voltage V_{out} was converted to resistance using the circuit transfer function:

$$R = \frac{R_f\,(V_{\text{in}} - V_{\text{ref}})}{V_{\text{ref}} - V_{\text{out}}} \tag{S5}$$

The sensor-specific calibration coefficients a_i, b_i, and c_i were determined by fitting the $R_i(\varepsilon)$ dataset acquired during the calibration procedure to a quadratic model by least-squares regression:

$$R_i(\varepsilon) = a_i\varepsilon^2 + b_i\varepsilon + c_i \tag{S6}$$

During the shape reconstruction process, the measured resistance R_i was mapped to strain by inverting this fitted model:

$$a_i\varepsilon^2 + b_i\varepsilon + (c_i - R_i) = 0 \tag{S7}$$

The physically meaningful positive root gives the reconstructed strain:

$$\varepsilon = \frac{-b_i + \sqrt{b_i^2 - 4a_i(c_i - R_i)}}{2a_i} \tag{S8}$$

Note S4: Analysis of different frequency signals

Time-synchronized pressure and voltage signals were analyzed to quantify the dynamic coupling between pneumatic excitation and electrical response across multiple driving frequencies. For each run, a steady-state window ($T = 20$ s) was selected and re-referenced such that $t = 0$ corresponds to the start of the window. For each run, the fundamental frequency f_0 of the pressure excitation was estimated from the pressure setpoint signal $P_{\text{set}}(t)$ within the analysis window. Specifically, the dominant spectral peak in the one-sided power spectrum obtained via the discrete Fourier transform was identified, yielding f_0 and $\omega_0 = 2\pi f_0$. The raw voltage signal $V(t)$ was first smoothed using a Savitzky–Golay (SG) filter. Both $P(t)$ and the processed voltage signal were then projected onto a sinusoidal basis at the fundamental angular frequency ω_0, allowing direct extraction of amplitude and phase at the excitation frequency.

$$x(t) \approx \alpha \sin(\omega_0 t) + \beta \cos(\omega_0 t) + \gamma, \tag{S9}$$

The phase was computed as $\phi = \text{atan2}(\alpha, \beta)$ (rad). The phase difference $\Delta\phi = \phi_{\Delta V} - \phi_P$ was converted to a time delay,

$$\tau_{\text{phase}} = \frac{\Delta\phi}{\omega_0}. \tag{S10}$$

The time delay in each cycle was estimated from the difference between the pressure peak and the corresponding voltage peak:

$$\Delta t_i = t_{V,\max,i} - t_{P,\max,i}. \tag{S11}$$

The phase shift was then calculated as $\phi_i = 2\pi f_0 \Delta t_i$, and the voltage amplitude as $\Delta V_i = (V_{\max,i} - V_{\min,i})/2$. The values in Table S2 are reported as mean ± SD over the steady-state cycles.

Note S5: Localized calibration

For individual sensor localized calibration, each pneumatic chamber was subjected to a synchronous monotonic pressure ramp from 0 to 2.5 bar and back to 0 bar. The synchronized pressurization produced a uniform axial extension of the soft actuator, subjecting the embedded IHS to uniaxial tensile deformation. Individual sensor signal was recorded and cropped ($t \in [10, 90]$ s) to exclude the equilibrium stage. The displacement magnitude $\Delta s(t)$ was derived from EM tracker measurements as:

$$\Delta s(t) = \sqrt{(x(t) - x_0)^2 + (y(t) - y_0)^2 + (z(t) - z_0)^2}, \tag{S12}$$

where, (x_0, y_0, z_0) denotes the starting position of the tip (t=0), and $(x(t), y(t), z(t))$ represent tip position at time t. Displacement was converted to engineering strain using the initial actuator length L_0,

$$\varepsilon(t) = \frac{\Delta s(t)}{L_0} \times 100\%. \tag{S13}$$

Each sensing channel was independently calibrated using data acquired during the pressure ramp. The measured voltage $V(t)$ was first converted to resistance $R(t)$ via the circuit transfer function, and temporally synchronized with the EM-derived strain $\varepsilon(t)$ via timestamp alignment. The $R(\varepsilon)$ data for each sensing channel were fitted to a quadratic equation by least-squares regression, yielding sensor-specific calibration curves for strain extraction during operation.

Note S6: 3D shape reconstruction under constant curvature assumption

Three strain sensors were mounted circumferentially around the actuator at a radial distance r from the neutral axis, with angular locations θ_i $(i = 1, 2, 3)$ defined in the cross-sectional plane. At each time instant t, the measured voltages $V(t)$ were converted into axial strains $\varepsilon_i(t)$ using the individual quadratic calibration model obtained previously.

Under pneumatic actuation, the actuator undergoes both bending and axial elongation. The measured strain at each sensor can therefore be decomposed into a common-mode component, representing the axial strain of the actuator, and a differential component, representing bending-induced strain:

$$\varepsilon_0(t) = \frac{1}{3}\sum_{i=1}^{3}\varepsilon_i(t), \qquad \varepsilon_i(t) = \varepsilon_i(t) - \varepsilon_0(t) \tag{S14}$$

Here, $\varepsilon_0(t)$ approximates the common axial elongation component of the actuator. Although the calibrated strain values in Table S5 are reported in percent for readability, they were converted to dimensionless fractional strain before being used in the backbone-length update and curvature reconstruction in Equations S15–S17. The instantaneous backbone length is therefore given by

$$L(t) = L_0\,(1 + \varepsilon_0(t)) \tag{S15}$$

where L_0 is the undeformed actuator length.

Following the Euler-Bernoulli beam assumption [4, 5], the axial strain at a radial distance r from the neutral axis is linearly proportional to the local curvature. Denoting the reconstructed axial strain of the i-th sensor at time t as $\tilde{\varepsilon}_i(t)$, the strain readings from the three sensors can be directly mapped to the curvature vector components (κ_x, κ_y) via

$$\varepsilon_i(t) \approx r\big(\kappa_x(t)\cos\theta_i + \kappa_y(t)\sin\theta_i\big) \tag{S16}$$

where θ_i denotes the circumferential position of the i-th sensor. For the symmetric three-sensor configuration employed, the curvature κ magnitude and bending direction can be represented by:

$$\kappa_x(t) = \frac{2}{3r}\sum_{i=1}^{3}\tilde{\varepsilon}_i(t)\cos\theta_i, \qquad \kappa_y(t) = \frac{2}{3r}\sum_{i=1}^{3}\tilde{\varepsilon}_i(t)\sin\theta_i \tag{S17}$$

The curvature magnitude $\kappa(t)$ and the bending-plane orientation $\theta_k(t)$ were subsequently recovered from the reconstructed curvature vector (κ_x, κ_y).

$$\kappa(t) = \sqrt{\kappa_x(t)^2 + \kappa_y(t)^2}, \qquad \theta_k(t) = \operatorname{atan2}\big(\kappa_y(t), \kappa_x(t)\big) \tag{S18}$$

The actuator backbone is then modeled as a circular arc with constant curvature $\kappa(t)$ and instantaneous length $L(t)$. The bending angle is $\phi(t) = \kappa(t)L(t)$. In the local bending plane, the tip position relative to the base is

$$x_b(t) = \frac{1 - \cos\big(\kappa(t)L(t)\big)}{\kappa(t)}, \qquad z_b(t) = \frac{\sin\big(\kappa(t)L(t)\big)}{\kappa(t)} \tag{S19}$$

For the special case of negligible bending, the constant-curvature formulation reduces to a straight backbone, where the lateral displacement is zero, and the axial coordinate equals the effective length, i.e., $(x_b, z_b) = (0, L(t))$.

Rotating the local bending plane by $\theta_k(t)$ yields the three-dimensional tip position $p(t)$:

$$p(t) = \begin{bmatrix} x(t) \\ y(t) \\ z(t) \end{bmatrix} = \begin{bmatrix} x_b(t)\cos\theta_k(t) \\ x_b(t)\sin\theta_k(t) \\ z_b(t) \end{bmatrix} \tag{S20}$$

Repeating the above procedure over time produces the reconstructed three-dimensional tip trajectory.

A systematic time offset of $\tau = 0.94$ s was used as an approximation of the system delay between the strain-derived reconstruction and the EM tracking reference for the fixed low-frequency trajectory tested here. This value was selected from the 0.05 Hz dynamic characterization, which was the closest experimentally measured condition to the approximately 0.033 Hz reconstruction trajectory. To quantify the effect of this delay on the reconstruction accuracy, two error metrics are reported: the *compensated* error, computed between the reconstructed tip position $p_{\mathrm{rec}}(t)$ and the EM reference $p_{\mathrm{EM}}(t+\tau)$; and the *non-compensated* error, computed between $p_{\mathrm{rec}}(t)$ and $p_{\mathrm{EM}}(t)$ without applying any time-delay correction.

Note S7. Numerical torsion-sensitivity analysis

A numerical torsion-sensitivity analysis was conducted using the static forward model reported in previous work [1]. The model is based on a static Cosserat-rod formulation, in which pneumatic chamber pressures are represented as distributed force and moment terms along the actuator body, while external loads are prescribed through terminal force/moment boundary conditions.

In the simulation, the pneumatic actuation input was defined as `act_pressure = [P1, P2, P3]`, and the external terminal moment was defined as `torsion_moment = [Mx, My, Mz]`. The model computed the actuator shape and the axial strains along three virtual sensor paths placed 120° apart around the actuator circumference.

A representative terminal moment magnitude of 0.0085 N · m was estimated from a 1 N contact force acting with an 8.5 mm moment arm. Two simulation cases were considered: torsion without pneumatic actuation, and torsion under a representative large-bending condition. For the no-bending case, the moment was applied about the undeformed actuator axis. For the bending case, the same moment magnitude was applied along the deformed local tip axis and expressed in the global coordinate frame. The torsion-induced strain perturbation was calculated by subtracting the corresponding no-torsion strain from the with-torsion strain. The results are summarized in Figure S25 and Table S7.

References

[1] Jialei Shi, Hanyu Jin, Wenlong Gaozhang, Ge Shi, Sara-Adela Abad, and Helge A. Wurdemann. A static modeling and evaluation framework for soft continuum robots with reinforced chambers. *IEEE Transactions on Robotics*, 41:6419–6439, 2025.

[2] W. Zhao, Z. Lin, Z. Sun, Z. Zhu, W. Lin, Y. Xu, Z. Peng, Z. Sun, and Z. Wang. Road narrow-inspired strain concentration to wide-range-tunable gauge factor of ionic hydrogel strain sensor. *Adv. Sci.*, 10:2303338, 2023.

[3] S. Cheng, Y. S. Narang, C. Yang, Z. Suo, and R. D. Howe. Stick-on large-strain sensors for soft robots. *Adv. Mater. Interfaces*, 6:1900985, 2019.

[4] J. P. Moore and M. D. Rogge. Shape sensing using multi-core fiber optic cable and parametric curve solutions. *Opt. Express*, 20:2967–2973, 2012.

[5] J. So, U. Kim, Y. B. Kim, D.-Y. Seok, S. Y. Yang, K. Kim, J. H. Park, S. T. Hwang, Y. J. Gong, and H. R. Choi. Shape estimation of soft manipulator using stretchable sensor. *Cyborg Bionic Syst.*, 2021:9843894, 2021.